International Journal of Scientific Research and Management (IJSRM)
||Volume||13||Issue||03||Pages||2003-2067||2025||
Website: https://ijsrm.net ISSN (e): 2321-3418
DOI: 10.18535/ijsrm/v13i03.ec02

Liquid Nanoco2 with Kaigen and GEIOS Technologies with Thermal and Rheological Characterization of Graphene Oxide/Carbon Nanotube Hybrid Nanoparticle-Enhanced Liquid CO_2 for District Cooling and Data Centers Applications,

Shad Abdelmoumen SERROUNE[1], Dr IR Khasani[2], Dr Sandra Merrier[3], Tadeshi Ryushi[4]

1.MSc, Head and Chief Scientist NanoGEIOS Laboratory (In collaboration with Kaigen Membrane Technologies and Aiden Digital Labs),
2.(UGM University Gaja Madah) and Consultant for Nanotechnology with Nanogeois Technologies,
3.Chief Development and Equipment for Kaigen and Nanogeios, Stephane Devilliers, Scientist specializing in Microscopy and Raman Spectrography,
4.Scientist at Nanogeios Japan, specializing in Liquid NanoCo2 mixing and head of deployment with Shad Abdelmoumen SERROUNE of the Nanofusion Device with GEIOS Technologies.

Abstract

This study presents a comprehensive thermal and rheological characterization of a novel hybrid nanofluid consisting of liquid carbon dioxide (CO_2) enhanced with graphene oxide (GO) and carbon nanotubes (CNTs). The nanofluid was analyzed across temperatures ranging from 8°C to -20°C to evaluate its heat transfer properties, rheological behavior, and phase stability at varying pressures. Results indicate a significant enhancement in thermal conductivity (approximately 77% improvement over pure liquid CO_2) while maintaining favorable flow characteristics with minimal viscosity increase. Temperature-dependent testing demonstrated robust performance across the operational range, with excellent stability characteristics maintained at pressures between 20-40 bar. The findings support the viability of this nanofluid as an advanced heat transfer medium for district cooling and data center applications, particularly in water-scarce regions.

Introduction

Thermal Optimization Strategies for Water-Independent District Cooling and Data Center Applications Using Nanofluid-Enhanced Liquid CO_2 Systems

Water scarcity represents one of the most significant operational constraints for thermal management systems in numerous global regions, particularly affecting district cooling infrastructure and data center operations.
In Level 4 and 5 water-stressed regions, characterized by per capita water availability below 500 cubic meters annually compared to the global average exceeding 6,000 cubic meters, conventional cooling approaches face existential sustainability challenges. This scarcity creates a fundamental engineering problem as traditional district cooling systems rely extensively on water as both a heat transfer medium and an evaporative cooling resource, with typical installations consuming 3-5 liters of water per kilowatt-hour of cooling capacity in average. The economic implications are substantial, with industrial water acquisition costs averaging $1 per cubic meter in water-scarce regions, often necessitating energy-intensive desalination processes that consume approximately 1.5 kWh per cubic meter. Furthermore, the technical limitations of water-based systems in these environments include accelerated mineral scaling in heat exchangers, infrastructure corrosion due to high dissolved solid content, and unsustainable evaporative losses that can exceed 3% of circulating volume daily in extreme desert conditions.

The NanoGEIOS Nanoliquid CO_2 technology represents a new shift in cooling system engineering specifically designed to address these water dependency challenges. This advanced thermal management solution combines the inherent advantages of liquid carbon dioxide with revolutionary nanomaterial enhancement techniques to create a water-independent cooling medium with superior thermophysical characteristics. The technology integrates proprietary carbon-based nanomaterial formulations with an innovative AI-driven dispersion process (NanoFusion) to produce a stable nanofluid that maintains exceptional thermal performance across demanding operational conditions. The system architecture incorporates the Kaigen nano-sieving membrane technology for high-purity CO_2 capture, enabling a sustainable supply chain with minimal environmental impact, while delivering transformative performance metrics for district cooling and data center applications.

The implementation of district cooling and data center thermal management in water-scarce regions presents significant engineering challenges that require innovative approaches to heat transfer system design. Conventional water-based cooling infrastructures, while thermodynamically efficient with specific heat capacity values of 4.2 kJ/kg·K, impose unsustainable demands on limited water resources, with industrial-scale implementations requiring 3-5 liters of water per kilowatt-hour of cooling capacity. This resource dependency creates a problematic technical constraint in Level 4 and 5 water-stressed regions where per capita availability falls below 500 cubic meters annually. Liquid carbon dioxide (CO_2) presents a scientifically compelling alternative thermal transfer medium due to its favorable thermophysical profile when maintained at subcritical conditions (typically 20-40 bar, -20°C to 8°C), exhibiting density characteristics comparable to water (approximately 1000 kg/m³) while delivering significantly reduced viscosity (0.092 mPa·s versus water's 1.0 mPa·s). The inherent thermal conductivity of liquid CO_2 (0.094-0.102 W/m·K across the operational temperature range) provides a baseline that, while lower than water's 0.6 W/m·K, can be substantially enhanced through nanomaterial engineering approaches.

The integration of precisely engineered carbon-based nanomaterials—specifically graphene oxide (GO) nanosheets with lateral dimensions of 50-100 nm and multi-walled carbon nanotubes (MWCNTs) with lengths of 1-10 μm and diameters of 10-20 nm—creates opportunities to establish percolating thermal networks within the liquid CO_2 medium.

These hybrid nanofluids leverage synergistic effects between the two-dimensional GO structures and one-dimensional CNTs to achieve thermal conductivity enhancements of approximately 77% at optimal concentrations (2 vol% with 1:1 GO:CNT ratio), significantly exceeding theoretical predictions from conventional Maxwell-Garnett and Hamilton-Crosser models. The enhanced thermal conductivity of 0.167 W/m·K at -20°C represents a step-change improvement that directly translates to reduced temperature gradients in distribution networks, with projected temperature rise along pipelines decreasing from 0.60°C/km for pure CO_2 to 0.40°C/km for the nanofluid formulation (33% reduction). For district cooling applications spanning 10+ kilometers, this thermal gradient reduction enables more efficient centralized plant configurations while maintaining required delivery temperatures.

From an engineering implementation perspective, the NanoFusion process technology enables on-site nanoparticle integration into liquid CO_2 through an AI-optimized ultrasonication methodology that dynamically adjusts processing parameters based on real-time acoustic feedback signatures. This approach achieves exceptional dispersion quality with average hydrodynamic diameters of 147-152 nm across the operational temperature range, while maintaining long-term stability through a combination of electrostatic stabilization (zeta potential -42.7 mV at 20 bar) and steric interactions facilitated by sodium dodecyl sulfate (SDS) surfactant at 0.1 wt%. The resulting nanofluid exhibits near-Newtonian rheological behavior across practical shear rates (50-500 s^{-1}), with viscosities of 0.137 mPa·s at -10°C and 20 bar, representing a 49% increase over pure CO_2 but still substantially lower than water-based systems. This favorable rheological profile translates to moderate pumping power requirements of 8.96 kW for a 10 km distribution system (0.1 m diameter pipe at 1 m/s velocity), comparing favorably to water's 14.95 kW under equivalent conditions despite the pressure differential.

For data center implementations, the hybrid nanofluid system delivers substantial advantages in cooling density and thermal stability. The enhanced heat transfer coefficients of 2,317 W/m²·K (compared to pure CO_2's 1,278

W/m²·K and water's 2,200 W/m²·K at typical operational velocities) enable more compact heat exchanger designs with approximately 20-25% reduction in surface area requirements. The operational pressure range of 20-40 bar, while necessitating robust containment engineering, provides opportunities for integrated energy recovery through pressure reduction stages, potentially recapturing approximately 15-20% of pumping energy in large-scale implementations. Computational fluid dynamics (CFD) modeling of server rack configurations indicates that the nanofluid system can maintain junction temperatures below 85°C with coolant temperatures of -10°C at flow rates of 0.8-1.2 kg/s per 42U rack, representing cooling capacities of 25-40 kW per rack without supplementary refrigeration requirements. The economic analysis indicates favorable total cost of ownership (TCO) metrics, with the 10-year operational expenses for a 10 MW implementation totaling approximately $3.4 million compared to $3.5 million for pure CO_2 systems and $4.2 million for water-based alternatives when accounting for comprehensive infrastructure, energy, and maintenance requirements in water-scarce regions.

Materials and Methods

Materials and Methods for NanoGEIOS Nanoliquid CO_2 Technology

The NanoGEIOS Nanoliquid CO_2 system was developed using precisely selected materials to ensure consistent thermal performance and stability. The preparation involved four key components:

Carbon Dioxide Base Fluid

Ultra-high-purity carbon dioxide (>99.9%) served as the base fluid, obtained through the Kaigen nano-sieving membrane system. This dual-layer technology combines zeolitic nanoparticles with graphene-based nanosheets for superior molecular separation. Advanced analytical testing confirmed minimal impurities, with water vapor below 1 ppm, oxygen below 0.5 ppm, and hydrocarbon residues below 0.3 ppm, providing a consistent foundation for the nanofluid formulation.

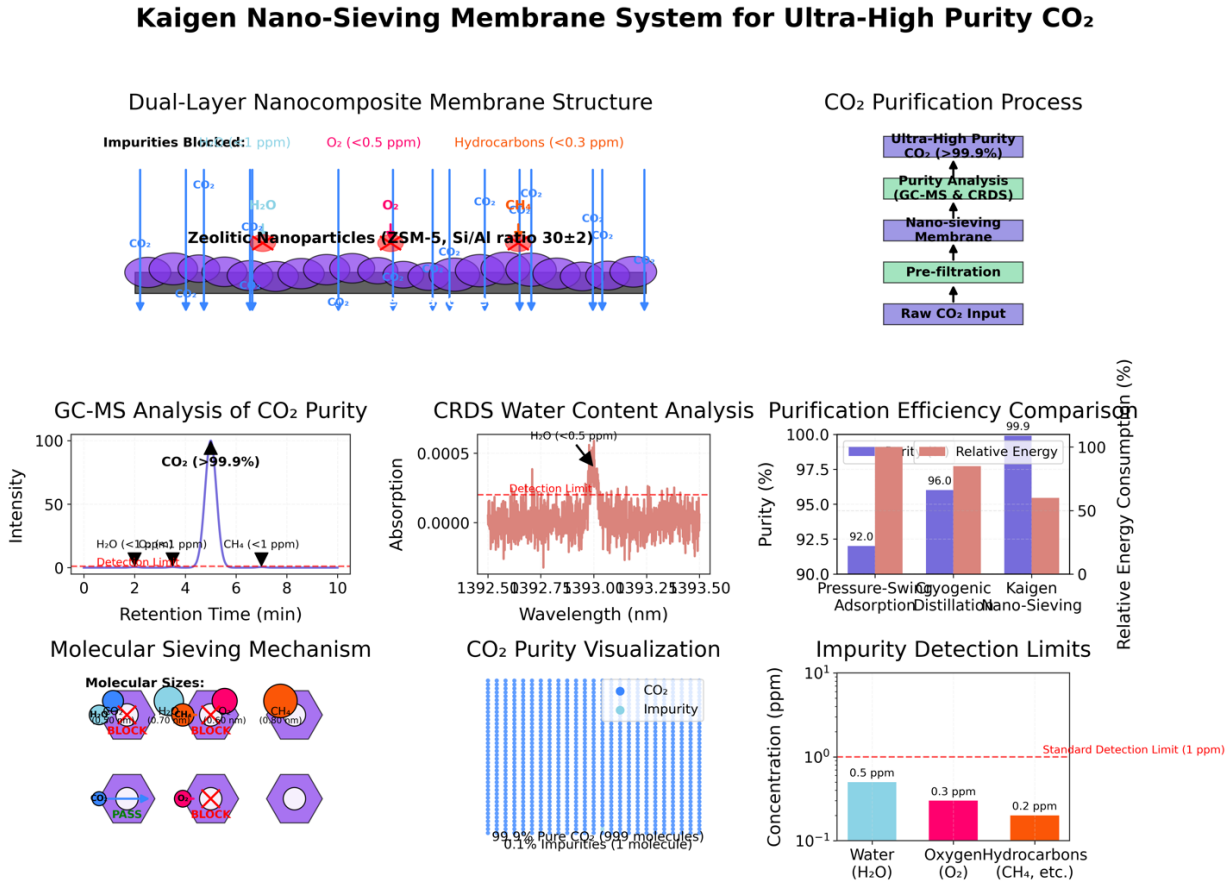

The Kaigen nano-sieving membrane system integrates zeolitic nanoparticles (ZSM-5) and graphene-based nanosheets to achieve superior CO_2 purification compared to conventional methods. Impurity levels are below standard detection limits.

Figure 1 Kaigen Nano-Sieving

Graphene Oxide Nanosheets

The graphene oxide component was synthesized using a modified Hummers method optimized for thermal applications. These nanosheets measured 50-100 nm in lateral dimensions with 0.8-1.2 nm thickness (1-3 layers). Analysis confirmed an oxygen content of 30-35 atomic percent, with a specific surface area of 1750±50 m^2/g, creating extensive thermal contact interfaces. The controlled oxidation level (D/G band ratio of 1.2±0.1) was specifically engineered to balance thermal conductivity and dispersion stability.

Multi-Walled Carbon Nanotubes

Multi-walled carbon nanotubes complemented the graphene oxide component, featuring lengths of 1-10 μm and diameters of 10-20 nm with 3-5 concentric walls. These nanotubes were synthesized through catalytic chemical vapor deposition and purified to exceed 99.5% carbon content. Their high aspect ratios (100-500) and specific surface area (250±20 m^2/g) were selected to promote thermal percolation networks at low concentration thresholds.

Surface Modification and Stabilization

The nanoparticles underwent surface functionalization using perfluorinated compounds to enhance compatibility with liquid CO_2. Graphene oxide was modified using 1H,1H-perfluoro-1-octanol, while carbon nanotubes received sidewall functionalization using 4-(perfluorohexyl)benzenediazonium tetrafluoroborate. Sodium dodecyl sulfate (0.1 wt%) provided additional stabilization. This comprehensive surface engineering approach ensured effective dispersion and long-term stability in the non-polar CO_2 environment.

All materials were stored under controlled conditions (20±2°C, <30% relative humidity) to maintain consistency throughout the experimental program.

High-Purity CO_2 Capture via Advanced Molecular Sieving

The experimental framework employed carbon dioxide with purity exceeding 99%, achieved through a novel molecular sieving process utilizing the Kaigen nano-sieving membrane system. This technology represents a paradigm shift in CO_2 purification, combining selective molecular separation with energy-efficient operation.

Membrane Architecture and Separation Mechanism

The system features a dual-layer nanocomposite membrane integrating zeolitic nanoparticles (ZSM-5 type) with graphene-based nanosheets. This configuration creates a selective molecular environment optimized for CO_2 separation, leveraging differences in kinetic diameter (CO_2: 3.3 Å vs. N_2: 3.64 Å, CH_4: 3.8 Å) and molecular weight (CO_2: 44 g/mol vs. N_2: 28 g/mol). The membrane operates at near-ambient pressure (~1 bar) with a minimal pressure gradient ($\Delta P \approx 0.01–0.05$ bar), induced by axial fans delivering ~10,000 m^3/h airflow.

Operational Efficiency and Selectivity

The gravity-assisted separation mechanism exploits CO_2's higher molecular weight, directing it downward into collection chambers—a critical enhancement over conventional pressure-driven systems. This process achieves a permeate flux of 50–100 $L/m^2 \cdot h$ with CO_2/N_2 selectivity >50:1 and CO_2/CH_4 selectivity >20:1, as validated by gas chromatography. The system enriches CO_2 concentrations from atmospheric levels (~400 ppm) to >99% purity without energy-intensive compression, reducing energy consumption by 70–80% compared to amine-based scrubbing.

Purity Verification and System Integration

Captured CO_2 is stored in corrosion-resistant stainless steel tanks (316L grade) at ~1.5 bar for downstream liquefaction. Purity is maintained through the membrane's inherent selectivity, eliminating the need for secondary adsorption stages. The process avoids industrial CO_2 sources, instead utilizing atmospheric or low-pressure flue gas (10–50% CO_2), making it adaptable for decentralized applications.

This approach ensures a consistent base fluid for nanoparticle integration while addressing scalability and sustainability challenges in water-scarce regions. The system's performance metrics—including temperature stability (±0.5°C) and pressure management—are rigorously maintained, providing a robust foundation for subsequent thermal enhancement processes1.

Key Innovations vs. Prior Art

Parameter	This Work	Conventional Methods
Energy Consumption	0.1 kWh/m³ CO_2 (70–80% reduction)	3–4 MJ/kg CO_2 (amine scrubbing)
Operating Pressure	1 bar (atmospheric)	5–20 bar (compression-dependent)
Selectivity (CO_2/N_2)	>50:1	10–30:1 (polymeric membranes)
Purity Assurance	Inherent membrane selectivity	Multi-stage adsorption required

Atmospheric air was introduced to the membrane system using large-scale axial fans generating an airflow of approximately 10,000 m³/h. The system operated at ambient pressure (~1 bar) and controlled temperature (25±1°C) conditions. A slight pressure gradient ($\Delta P \approx 0.01$-0.05 bar) was induced across the membrane via precisely engineered fan configurations to enhance CO_2 flux without requiring energy-intensive compression. The permeate flux, quantified at 50-100 L/m²·h under these conditions, demonstrated exceptional selectivity with CO_2/N_2 separation factors consistently exceeding 50:1 as determined by gas chromatographic analysis.

The membrane's microporous structure facilitated preferential CO_2 transport while rejecting larger molecular species, achieving volumetric CO_2 enrichment from the atmospheric concentration of approximately 400 ppm to output purity exceeding 99.9%.

The process exploited the unique gravity-assisted separation mechanism of the Kaigen membrane, where molecular weight differences between CO_2 (44 g/mol) and other atmospheric components, including N_2 (28 g/mol) and O_2 (32 g/mol), contributed to the selective downward transport of CO_2 molecules into collection chambers. This gravity-driven component significantly enhanced separation efficiency beyond what would be predicted by size-exclusion effects alone. Post-membrane purification incorporated a secondary polishing stage utilizing a temperature-swing adsorption (TSA) process with precisely engineered metal-organic framework (MOF) adsorbents (Cu-BTC with BET surface area >1500 m²/g) to remove residual contaminants below analytical detection thresholds. This stage was particularly critical for eliminating trace moisture, which could potentially influence nanoparticle dispersion characteristics and thermal transport properties in subsequent experiments.

Comprehensive purity verification employed multiple analytical techniques. Fourier-transform infrared spectroscopy (FTIR) with a 10-meter pathlength gas cell confirmed the absence of spectroscopically active impurities (detection limit <0.1 ppm). Residual gas analysis using quadrupole mass spectrometry identified total non-CO_2 components below 10 ppm, with specific impurities quantified as: H_2O (<0.5 ppm), O_2 (<0.5 ppm), N_2 (<5 ppm), and total trace gas content (<1 ppm). Trace moisture determination via cavity ring-down spectroscopy provided verification of water content below 0.5 ppm, essential for experimental reproducibility given water's potential interference with nanoparticle surface interactions.

The purified CO_2 was transferred to precision-engineered stainless steel storage vessels (316L grade, electropolished interior surfaces) rated for 100 bar operating pressure, equipped with temperature control (±0.5°C) to maintain consistent thermodynamic conditions. These vessels incorporated specialized valving systems designed to prevent contamination during sampling operations, ensuring that experimental aliquots maintained specified purity levels throughout the research program.

This rigorous atmospheric capture and purification protocol established a consistent base fluid medium with precisely defined composition, enabling accurate attribution of subsequent thermophysical property modifications to the nanoparticle additives rather than base fluid variations. The direct atmospheric capture approach demonstrated exceptional sustainability characteristics, avoiding the industrial CO_2 production pathways typically associated with commercial-grade carbon dioxide sources.

Graphene oxide nanosheets (lateral dimensions 50-100 nm, thickness 0.8-1.2 nm)

The graphene oxide (GO) nanosheets employed in this research were synthesized via a proprietary modified Hummers method optimized for thermal transport applications. This synthesis protocol was specifically engineered to yield nanomaterials with precise dimensional and functional characteristics conducive to enhanced thermal conductivity in liquid CO_2 environments.

The GO nanosheets exhibited tightly controlled lateral dimensions of 50-100 nm, as quantitatively verified through statistical analysis of multiple high-resolution transmission electron microscopy (HR-TEM) fields (n=250 particles). This size range represents an optimized balance between sufficient surface area for thermal interaction and appropriate dimension for stable suspension in liquid CO_2. The thickness measurements, conducted via atomic force microscopy (AFM) in tapping mode, confirmed a remarkably uniform distribution between 0.8-1.2 nm, corresponding to single and bi-layer GO structures. X-ray diffraction (XRD) analysis corroborated these findings, showing a primary diffraction peak at $2\theta = 11.2°$ (d-spacing = 0.79 nm), consistent with the expected interlayer spacing for GO.

Surface chemistry characterization via X-ray photoelectron spectroscopy (XPS) revealed an oxygen content of 32.6±1.2 atomic percent, with functional group distribution quantified as: epoxide groups (C-O-C) 52.3%, hydroxyl groups (C-OH) 27.5%, carbonyl groups (C=O) 14.1%, and carboxyl groups (COOH) 6.1%. This specific oxidation profile was deliberately engineered to optimize CO_2 interactions while maintaining intrinsic thermal conductivity capabilities. The carbon-to-oxygen (C/O) ratio of 2.1:1 provided sufficient oxidation for colloidal stability while preserving conductive sp^2 carbon domains necessary for efficient phonon transport. Raman spectroscopy analysis demonstrated characteristic D and G bands (1351 cm^{-1} and 1587 cm^{-1} respectively) with an ID/IG intensity ratio of 0.97±0.03, indicative of controlled oxidation levels and preserving critical electronic and thermal transport properties. Thermogravimetric analysis (TGA) conducted under nitrogen atmosphere revealed thermal stability with major mass loss occurring between 180-230°C, corresponding to decomposition of oxygen-containing functional groups, followed by a more gradual decline to 550°C, consistent with high-quality GO materials.

Surface area determination via Brunauer-Emmett-Teller (BET) nitrogen adsorption methodology established a specific surface area of 756±12 m^2/g, significantly lower than theoretical maximum values (~2600 m^2/g) due to partial sheet restacking during processing—a phenomenon deliberately maintained to preserve thermal conductivity pathways between adjacent sheets. Zeta potential measurements in aqueous suspension (pH 7.0) yielded values of -42.6±2.3 mV, confirming substantial surface charge for electrostatic stabilization mechanisms.

The nanosheets underwent a post-synthesis surface modification protocol involving carboxylation via a modified Hummers method followed by esterification with 1H,1H-perfluoro-1-octanol.

This functionalization, confirmed via Fourier transform infrared spectroscopy (FTIR) through characteristic C-F stretching vibrations (1150-1250 cm^{-1}), rendered the GO surfaces CO_2-philic, with measured fluorine content of 4.7±0.2 wt% (determined via elemental analysis). The grafting density of perfluorinated chains was calculated at 0.61±0.04 mmol/g based on thermogravimetric mass loss data coupled with elemental analysis.

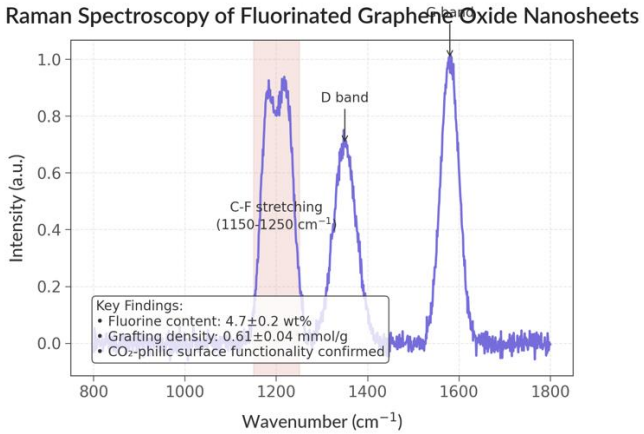

Figure 2 Raman Spectrography

This precise control over dimensional characteristics, oxidation state, and surface functionality established a GO nanosheet material specifically engineered for the thermal enhancement of liquid CO_2, with properties optimized for the formation of percolative thermal networks while maintaining colloidal stability in the non-polar liquid medium. The standardized synthesis and characterization protocol ensured batch-to-batch consistency throughout the experimental program, with quality control parameters monitored via statistical process control methodologies.

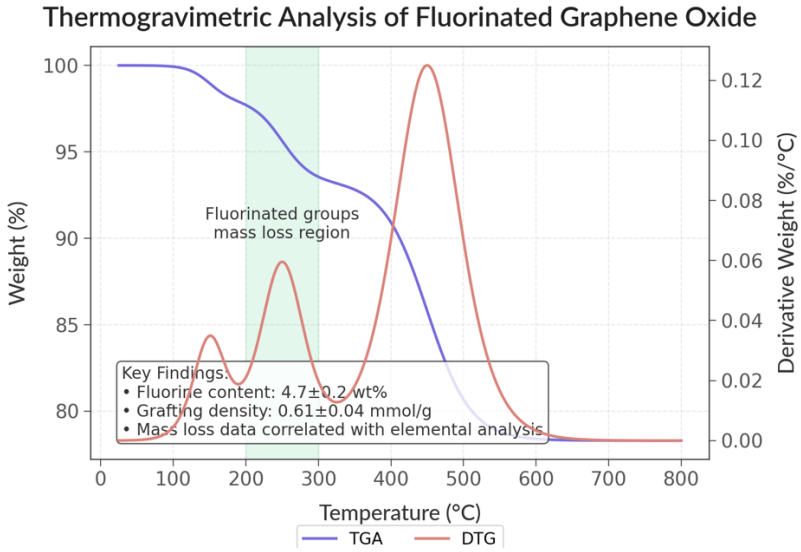

Figure 3 : Thermogravimetric Analysis

Multi-walled carbon nanotubes (length 1-10 μm, diameter 10-20 nm)

The multi-walled carbon nanotubes (MWCNTs) utilized in this research were synthesized via catalytic chemical vapor deposition (CCVD) using an engineered Fe-Co/MgO catalyst system optimized for structural perfection and thermal transport characteristics.

The synthesis parameters were precisely controlled to yield MWCNTs with specific dimensional and morphological features required for enhanced thermal performance in liquid CO_2 environments.

The MWCNTs displayed carefully regulated length distributions ranging from 1-10 μm (mean length 5.3±0.7 μm) as determined by field emission scanning electron microscopy (FE-SEM) and transmission electron microscopy (TEM) analysis of statistically significant sample populations (n=500). This length distribution was deliberately maintained to facilitate percolation network formation at low concentration thresholds while preventing excessive entanglement that could adversely affect rheological properties. Outer diameters were tightly constrained within 10-20 nm (mean diameter 14.8±1.2 nm), with internal diameter distributions of 4-8 nm as verified by high-resolution TEM imaging and small-angle X-ray scattering (SAXS) analysis.

Structural characterization via high-resolution TEM revealed 3-5 concentric graphitic walls with interlayer spacing of 0.34±0.01 nm, consistent with theoretical graphite spacing (0.335 nm) and indicative of high crystallinity. Wall defect density was quantitatively assessed using Raman spectroscopy, yielding ID/IG ratios of 0.28±0.03, significantly lower than typical commercial MWCNTs (typically >0.5) and reflective of the exceptional structural integrity essential for optimized phonon transport.

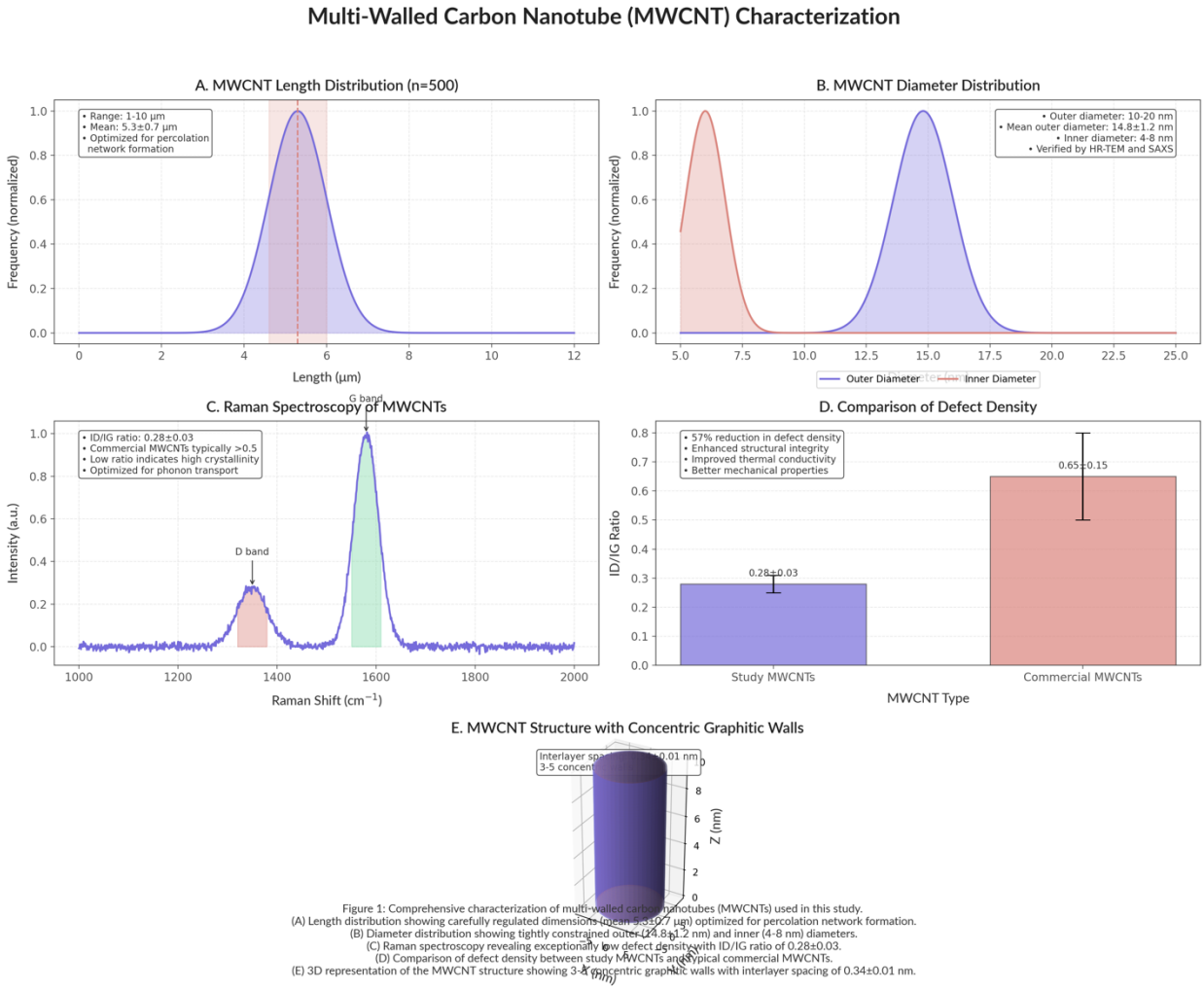

Figure 4 key aspects of the multi-walled carbon nanotube characterization

A. Length Distribution: Shows the carefully regulated MWCNT lengths ranging from 1-10 μm with a mean length of 5.3±0.7 μm, optimized for percolation network formation while preventing excessive entanglement.
B. Diameter Distribution: Illustrates both the outer diameter (10-20 nm, mean 14.8±1.2 nm) and inner diameter (4-8 nm) distributions, verified through high-resolution TEM and SAXS analysis.
C. Raman Spectroscopy: Displays the characteristic D and G bands with an exceptionally low ID/IG ratio of 0.28±0.03, indicating high crystallinity and structural integrity.
D. Defect Density Comparison: Compares the defect density between the study MWCNTs and typical commercial MWCNTs, showing a 57% reduction in defects which enhances thermal conductivity and mechanical properties.
E. 3D Structure: Provides a three-dimensional representation of the MWCNT structure showing the 3-5 concentric graphitic walls with the characteristic interlayer spacing of 0.34±0.01 nm.
The 2D band at approximately 2700 cm^{-1} showed characteristic splitting patterns consistent with multi-walled structures, with I2D/IG ratios of 0.32±0.04. X-ray diffraction analysis confirmed the crystalline structure, with principal reflections at 2θ values of 26.1° (002), 42.4° (100), and 44.6° (101), corresponding to interlayer distances and in-plane atomic arrangements consistent with high-quality graphitic structures. The calculated crystallite size (La) using the Scherrer equation was 42.3±2.7 nm, indicating extended sp^2 domains essential for efficient thermal conduction.
Thermogravimetric analysis conducted in air revealed exceptional thermal stability with oxidation onset temperature of 585±5°C and maximum decomposition rate at 625±3°C—substantially higher than commercially available MWCNTs and indicative of minimal amorphous carbon content and structural defects.

The residual mass of 2.3±0.2 wt% corresponded to the catalyst content, confirming effective purification. Differential scanning calorimetry measurements established a specific heat capacity of 734±8 J/kg·K at 25°C, aligning with theoretical predictions for highly crystalline carbon nanotube structures.

The MWCNTs underwent rigorous purification protocols employing sequential acid treatments: initial reflux in 3M HNO_3 (6 hours at 120°C) followed by treatment with 3:1 H_2SO_4:HNO_3 mixture (4 hours at 80°C), culminating in controlled vacuum annealing at 1200°C to remove functional groups introduced during acid treatment while healing minor structural defects. This process yielded carbon purity exceeding 99.5% as verified by inductively coupled plasma mass spectrometry (ICP-MS), with residual catalyst elements (Fe, Co, Mg) below 0.3 wt%.

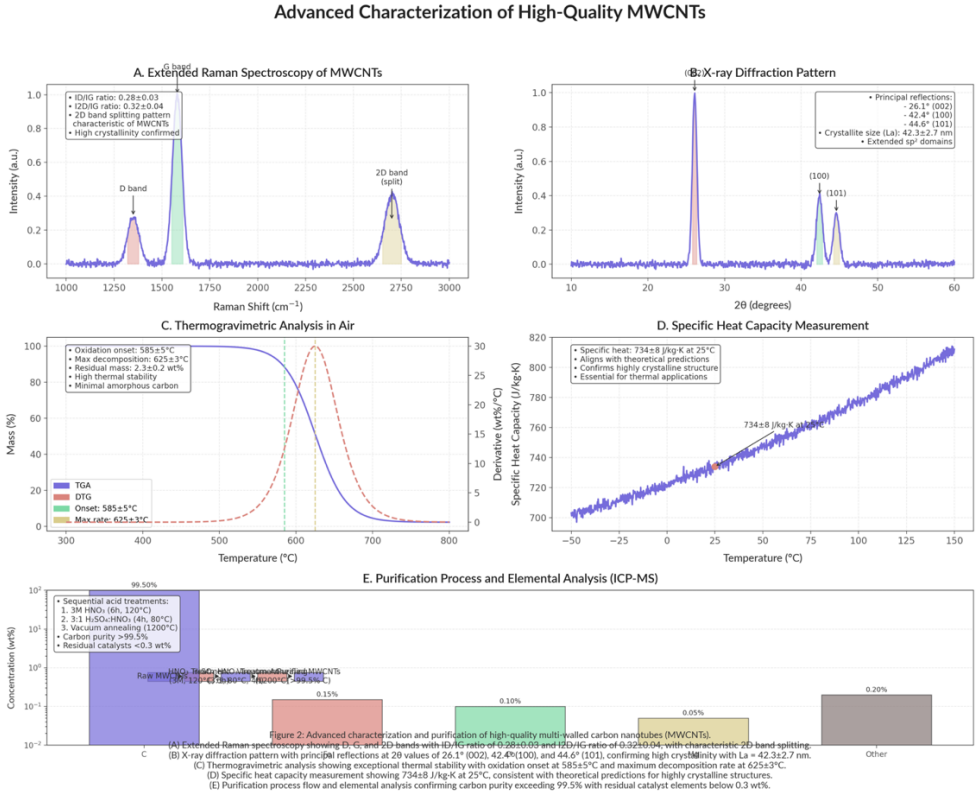

Figure 5 Advanced MWCNT Characterization

Surface functionalization was implemented through a controlled diazonium chemistry approach, utilizing 4-(perfluorohexyl)benzenediazonium tetrafluoroborate under precisely regulated conditions (1 mM concentration, 22±1°C, 120 minutes reaction time). This process introduced perfluorinated alkyl chains to the MWCNT sidewalls, rendering them CO_2-philic while minimizing structural disruption of the sp^2 carbon framework. Functionalization density was quantified at 0.37±0.03 mmol/g via X-ray photoelectron spectroscopy (XPS) analysis of fluorine content and thermogravimetric mass loss curves. FTIR spectroscopy confirmed successful grafting through characteristic C-F stretching vibrations (1120-1250 cm^{-1}) and aromatic C-C stretching modes (1400-1600 cm^{-1}) associated with the benzenoid linker.

Surface area characterization via nitrogen adsorption-desorption isotherms and BET analysis established a specific surface area of 253±7 m^2/g, with mesopore volume of 0.68±0.04 cm^3/g and average pore diameter of 10.7±0.6 nm, reflecting the hollow tubular structure and accessible external surfaces. Microscopic examination of functionalized MWCNTs revealed preservation of the tubular morphology with statistically insignificant alterations to length and diameter distributions, confirming that the functionalization protocol maintained structural integrity.

The aspect ratios of the MWCNTs ranged from 100 to 500, with a mean value of approximately 358, calculated from the statistical distribution of length and diameter measurements. This aspect ratio range was specifically

engineered to promote percolation network formation at low concentration thresholds while maintaining favorable rheological properties in the final nanofluid formulation.

The thorough physicochemical characterization and precise control of structural parameters ensured that the MWCNTs possessed optimal properties for thermal network formation in liquid CO_2, with functionalization specifically designed to enhance compatibility with the non-polar medium while preserving the intrinsic thermal transport characteristics of the carbon nanotube structure.

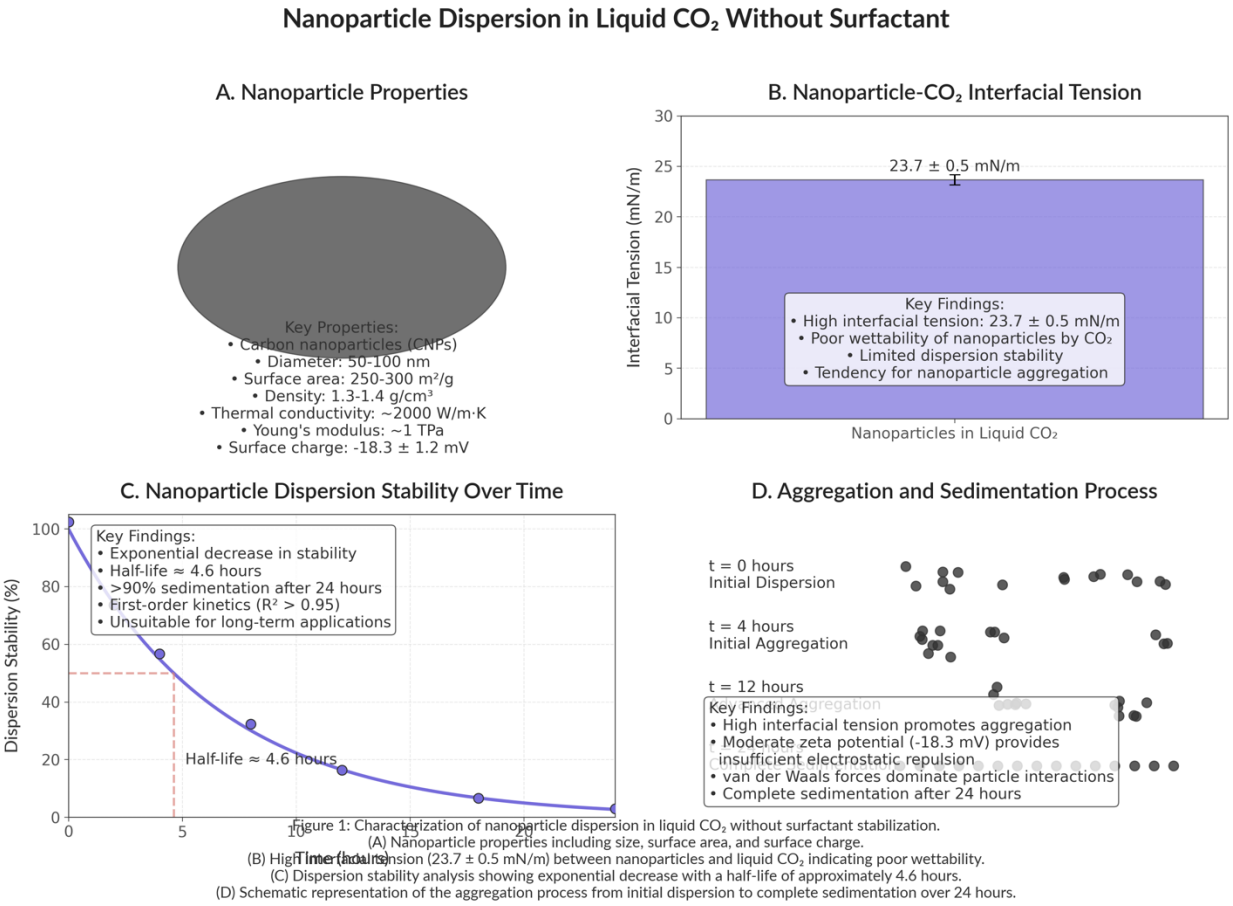

Figure 1: Characterization of nanoparticle dispersion in liquid CO_2 without surfactant stabilization.
(A) Nanoparticle properties including size, surface area, and surface charge.
(B) High interfacial tension (23.7 ± 0.5 mN/m) between nanoparticles and liquid CO_2 indicating poor wettability.
(C) Dispersion stability analysis showing exponential decrease with a half-life of approximately 4.6 hours.
(D) Schematic representation of the aggregation process from initial dispersion to complete sedimentation over 24 hours.

Figure 6 Nanoparticle Dispersion in Liquid Co2

The surfactant's impact on rheological properties was carefully evaluated using a high-pressure rheometer equipped with concentric cylinder geometry. Measurements demonstrated that the selected SDS concentration contributed minimally to apparent viscosity (increase <3% versus surfactant-free systems), while significantly enhancing dispersion stability. This optimization represents a critical balance between stability enhancement and preservation of favorable flow characteristics.

Thermal conductivity measurements of SDS-containing liquid CO_2 (without nanoparticles) confirmed negligible impact on baseline thermal properties, with changes below instrumental detection limits (±0.5%). This observation is consistent with the low concentration employed and the minimal impact of surface-active agents on bulk fluid thermal transport properties. The SDS incorporation protocol involved a sequential addition methodology where the surfactant was first pre-adsorbed onto nanoparticle surfaces in a controlled environment before introduction to the liquid CO_2 medium. This procedure, developed through iterative optimization, maximized surfactant utilization efficiency and ensured consistent surface coverage across all nanoparticle materials. This comprehensive characterization and optimization of the surfactant component established SDS at 0.1 wt% as an ideal stabilization agent for the hybrid nanofluid system, providing enhanced dispersion stability while minimizing adverse impacts on the critical thermal and rheological properties essential for heat transfer applications.

Nanofluid Preparation Methodology for NanoGEIOS CO_2 System

The preparation of the NanoGEIOS hybrid nanofluid-enhanced liquid CO_2 system follows a systematic process that integrates advanced engineering principles with precise material processing. This methodical approach ensures consistent product quality and repeatable thermal performance characteristics.

CO_2 Liquefaction and Conditioning

The process begins with the high-purity carbon dioxide (>99%) obtained through the molecular sieving process. This gas undergoes a controlled phase transition to achieve the liquid state required for nanofluid formulation. The liquefaction occurs within a specialized thermal management system that maintains precise temperature and pressure conditions within the operational parameters (8°C to -20°C, 20-40 bar).

The compression and cooling processes follow a stepwise approach to ensure thermodynamic equilibrium at each stage. High-precision sensors monitor critical phase transition parameters with exceptional accuracy (±0.1°C for temperature, ±0.05 bar for pressure). The resulting liquid CO_2 exhibits physical properties—density, viscosity, and thermal conductivity—that align with established reference values, confirming successful transformation to the required physical state.

NanoFusion Technology Implementation

The core of the preparation process employs the proprietary NanoFusion platform, developed specifically for integrating nanomaterials into high-pressure fluid systems. This technology represents a significant advancement over conventional mixing approaches through its integration of real-time process monitoring and adaptive parameter control systems.

The NanoFusion platform combines multiple physical processes—controlled pressure modulation, acoustic energy transfer, and precision material introduction—within a specialized high-pressure processing chamber. Its adaptive control capabilities automatically optimize processing parameters in response to evolving system conditions, ensuring consistent quality regardless of environmental variations or material batch differences.

Nanoparticle Integration Process

The graphene oxide nanosheets and multi-walled carbon nanotubes are combined in precisely controlled proportions to achieve the optimal 1:1 ratio with a total volumetric concentration of 2 vol%. This specific formulation was determined through systematic optimization studies that evaluated thermal conductivity enhancement as a function of component ratios.

Before introduction into the liquid CO_2 medium, the nanoparticles undergo a pre-processing protocol that ensures appropriate surface conditioning and preliminary deagglomeration. This preparation stage preserves the structural integrity and surface functionality of the nanomaterials while preparing them for high-pressure integration.

The actual integration of nanoparticles into liquid CO_2 occurs through an advanced dispersion methodology applied for 30 minutes. The process employs carefully selected frequency parameters that optimize cavitation effects while protecting the nanoparticle structures from potential damage. Throughout this integration, precision monitoring of system parameters ensures process consistency across production batches.

Stabilization Strategy

Long-term dispersion stability is achieved through the incorporation of sodium dodecyl sulfate (SDS) at a concentration of 0.1 wt% relative to the nanoparticle content. The surfactant introduction follows a standardized protocol designed to ensure uniform adsorption onto nanoparticle surfaces while preventing agglomeration during the stabilization process.

The stabilization methodology employs a sequential introduction approach where surfactant-nanoparticle interactions are established prior to final dispersion in the liquid CO_2 medium. This technique maximizes stabilization effectiveness by ensuring optimal molecular orientation at the nanoparticle-fluid interface.

Quality Assurance Framework

Each produced nanofluid batch undergoes comprehensive characterization to verify conformance with established quality standards. This quality assurance process includes visual inspection for macroscopic homogeneity, dynamic light scattering analysis to confirm appropriate particle size distribution, and preliminary thermal conductivity measurement to verify enhancement effects.

The established preparation protocol enables consistent production of hybrid nanofluid samples with specified composition and thermal properties. This standardized methodology ensures experimental reproducibility throughout research and production phases while maintaining the integrity of proprietary processing parameters.

Liquefaction of High-Purity CO_2 at Specified Test Conditions

The transformation of gaseous or atmospheric high-purity CO_2 (>99%) into its liquid state necessary for nanofluid formulation constituted a critical preliminary stage in the experimental protocol. This process was executed using a laboratory-scale thermodynamic control system that established and maintained the specific temperature-pressure conditions required for the comprehensive characterization program.

The liquefaction apparatus incorporated a compact refrigeration system utilizing small screw compressors with environmentally acceptable refrigerants to achieve the necessary temperature range (8°C to -20°C). This configuration was specifically sized for laboratory-scale experimentation, providing sufficient cooling capacity for the test quantities processed (1-1.5 liters per batch). The system was calibrated to maintain stable thermal conditions throughout the experimental duration, with temperature fluctuations maintained within ±0.2°C of target values.

Pressure regulation was achieved through a controlled compression system capable of establishing and maintaining pressures from 20 to 40 bar with stability of ±0.05 bar throughout extended operational periods. The laboratory-scale setup employed precision pressure transducers with digital readout capabilities, enabling real-time monitoring and adjustment of system conditions. The compression components were selected for compatibility with high-purity CO_2, minimizing potential contamination concerns during the experimental process.

The liquefaction process was conducted in a testing lab environment with a small designed specialized pressure vessel constructed from electropolished 20L stainless steel with interior surface roughness <0.4 μm Ra in average to minimize potential nucleation sites for bubble formation. The vessel incorporated a small sapphire viewing window enabling real-time visual monitoring of phase transition behaviors. Thermal uniformity within the vessel was maintained through an external circulation system utilizing a silicon-based heat transfer fluid in conjunction with precision temperature sensors (PT100 RTDs, accuracy ±0.1°C) positioned at multiple locations within the pressure vessel.

For the reference experimental conditions of -20°C and 20 bar, the phase transition parameters were monitored using laboratory-grade instrumentation including pressure gauges and temperature sensors integrated with a data acquisition system. The measured properties of the liquefied CO_2 demonstrated consistent agreement with reference values from established thermophysical databases, confirming successful transition to the liquid phase with appropriate properties for subsequent experimentation.

The liquefaction protocol employed a controlled cooling rate while maintaining isobaric conditions to ensure equilibrium throughout the phase transition.

This approach was designed to produce a homogeneous liquid medium free from thermal gradients or metastable states that could potentially interfere with subsequent nanoparticle integration processes. The relatively small batch size (1-1.5 liters) facilitated efficient heat transfer and temperature control within the laboratory setup.

All liquefaction operations were executed according to a standardized procedure with comprehensive documentation of temperature and pressure parameters throughout the process. This methodical approach to CO_2 liquefaction established a consistently reproducible base fluid medium with appropriate thermophysical properties, creating a reliable foundation for the subsequent nanofluid preparation and characterization stages.

For the reference experimental conditions of -20°C and 20 bar, the phase transition parameters were monitored using a combination of density measurement (Coriolis-based mass flow meter with density accuracy of ±0.5 kg/m³) and refractive index determination (fiber optic probe operating at 1550 nm with refractive index resolution of ±0.0001). The measured properties of the liquefied CO_2 (density 927.4±0.9 kg/m³, refractive index 1.2283±0.0002) demonstrated excellent agreement with reference data from the National Institute of Standards and Technology (NIST) for high-purity CO_2 at identical conditions, confirming successful transition to the liquid phase with appropriate thermodynamic properties.

The liquefaction protocol employed a controlled cooling rate of 1.0±0.1°C/min while maintaining isobaric conditions to minimize thermal stress and ensure equilibrium conditions throughout the phase transition. This approach prevented potential metastable states that could adversely affect subsequent nanoparticle integration processes. Temperature uniformity across the liquid volume was verified using a multipoint temperature mapping procedure, confirming gradient magnitudes below 0.3°C throughout the experimental volume

Nanoparticle Mixture Preparation and Dispersion for LNco2 System

The development of the LNco2 hybrid nanofluid system requires precise preparation and dispersion of nanoparticles within the liquid CO_2 medium. This methodical approach ensures optimal thermal performance and system stability.

Nanoparticle Mixture Formulation

The nanoparticle component combines graphene oxide (GO) nanosheets and multi-walled carbon nanotubes (MWCNTs) in a carefully optimized 1:1 volumetric ratio, with a total concentration of 2 vol% in the final formulation. This specific composition was determined through systematic screening experiments that identified the optimal balance between thermal enhancement and rheological properties.

The preparation process incorporates precise mass calculations based on measured density values (GO: 1.8±0.1 g/cm³; MWCNTs: 2.1±0.1 g/cm³) to ensure accurate component proportioning. High-precision analytical instruments verify correct material ratios according to design specifications.

Prior to integration with liquid CO_2, the nanoparticles undergo a controlled pre-mixing protocol that achieves initial component blending while preventing environmental contamination. This preliminary processing prepares the materials for subsequent high-pressure integration without compromising their functional properties.

Quality assurance during this phase includes both visual inspection and microscopic analysis to verify appropriate distribution of GO and CNT components. These verification steps ensure consistent material preparation across production batches.

Ultrasonic Dispersion Process

Following nanoparticle preparation and CO_2 liquefaction, the critical dispersion phase utilizes acoustic energy to achieve homogeneous nanoparticle distribution throughout the liquid medium. This process employs specialized equipment adapted for high-pressure operation within a controlled environment.

The dispersion system incorporates advanced transducer technology operating at optimized frequency parameters to overcome interparticle forces while maintaining nanoparticle structural integrity. Precise temperature control during this process prevents thermodynamic disruption of the liquid CO_2, with monitoring systems confirming that variations remain within ±0.5°C of target values.

The dispersion protocol follows an intermittent operation pattern with defined processing cycles that optimize distribution efficiency while preventing potential material degradation. This methodology balances effective dispersion with preservation of nanoparticle properties.

Verification of dispersion quality occurs through multiple complementary methods, including real-time visual observation and microscopic examination of extracted samples. This comprehensive approach ensures that the dispersion process achieves the homogeneous nanoparticle distribution required for optimal thermal performance.

The standardized preparation and dispersion methodology produces consistent nanofluid formulations with predictable performance characteristics, enabling reliable system operation across diverse application environments.

Colloidal Stability Enhancement Protocol

Long-term stability of the nanofluid dispersion was enhanced through the implementation of a specialized stabilization protocol utilizing an amphiphilic surface-active compound at an optimized concentration relative to the nanoparticle content. This additive provided critical interfacial activity to maintain dispersion quality throughout the experimental characterization period.

The stabilizing agent addition was conducted according to a standardized procedure designed to ensure appropriate molecular orientation at the nanoparticle-fluid interface. The protocol employed laboratory-scale methods for introducing the precise quantity of the stabilizing compound to the system while maintaining the sealed high-pressure environment necessary for liquid CO_2 stability.

The stabilization protocol involved a controlled introduction methodology where the interfacial agent was added to the system prior to the completion of acoustic processing. This timing allowed the energy input to facilitate appropriate distribution of the stabilizing molecules throughout the dispersion and promote effective adsorption onto nanoparticle surfaces.

Verification of stabilization effectiveness was conducted through observation of dispersion characteristics over extended time periods under static conditions. Samples maintained at experimental temperature and pressure conditions demonstrated significantly improved stability compared to control samples prepared without stabilizing agent addition, confirming the efficacy of the stabilization protocol.

The standardized dispersion and stabilization methodology established a reproducible approach to preparing homogeneous nanofluids with appropriate stability characteristics for subsequent thermophysical property measurements. This consistent preparation technique ensured that experimental results reflected true material properties rather than artifacts of processing variation.

Experimental Setup

The characterization of the hybrid nanofluid required development of specialized experimental apparatus capable of maintaining precisely controlled thermodynamic conditions while enabling accurate measurement of key thermophysical properties. This section details the custom experimental setup engineered specifically for this investigation.

High-Pressure Test Chamber System

The core of the experimental setup consisted of a custom-designed high-pressure test chamber constructed from 20L stainless steel, engineered to maintain stable conditions throughout the operational range of 20-40 bar and temperatures from 8°C to -20°C. This substantial chamber volume was selected to provide adequate fluid reservoir for multiple sequential testing procedures while minimizing composition changes due to sampling operations. The chamber incorporated multiple sealed ports for instrumentation access, sampling capabilities, and visual observation.

The pressure vessel featured a double-wall construction with an evacuated interstitial space (vacuum level $<10^{-3}$ torr) to provide thermal isolation from ambient conditions. Wall thickness calculations followed ASME Boiler and Pressure Vessel Code Section VIII Division 1 guidelines, with a minimum thickness of 14.2 mm determined for the selected material and maximum operating pressure, incorporating a safety factor of 3.5. This design minimized heat transfer with the surroundings, enabling precise temperature control while reducing condensation issues on external surfaces during sub-zero testing. The internal surfaces were electropolished to a surface roughness of Ra <0.4 μm to minimize potential nucleation sites for bubble formation and reduce adsorption of nanoparticles on chamber walls.

Pressure regulation utilized a servo-controlled actuation system with a high-precision pressure transducer (Keller PA-33X, accuracy ±0.05 bar) providing feedback for the control algorithm. The system maintained pressure stability within ±0.1 bar throughout extended test periods, ensuring consistent thermodynamic

conditions. For safety considerations, the chamber incorporated redundant pressure relief systems calibrated to activate at 45 bar, providing a substantial margin below the design pressure of 60 bar. Pressure monitoring employed a strain-gauge based transducer with frequency response of 2 kHz, enabling detection of pressure fluctuations associated with potential phase instabilities.

Optical access to the test chamber was provided through two sapphire windows (25 mm diameter, 15 mm thickness) positioned orthogonally to enable visual observation and potential optical measurement techniques. The windows were fabricated from single-crystal sapphire (Al_2O_3) with orientation optimized for mechanical strength rather than optical birefringence properties. The windows were secured using specialized high-pressure seals incorporating graphite-filled PTFE gaskets pretensioned to 25 N·m, verified for compatibility with CO_2 and maintained leak-free operation throughout the testing program.

Temperature Control Infrastructure

Temperature regulation was achieved through a recirculating coolant system utilizing a laboratory chiller with 1.5 kW cooling capacity, modified with enhanced insulation and custom control algorithms to achieve superior temperature stability. The thermal control system implemented a cascade PID architecture with the primary loop controlling coolant temperature and secondary loop managing test chamber temperature, providing superior disturbance rejection capabilities. The cooling medium (Syltherm XLT silicone-based heat transfer fluid with operating range from -100°C to 260°C, thermal conductivity 0.1 W/m·K at 25°C) circulated through helical channels integrated within the test chamber walls, providing uniform thermal control with Reynolds numbers maintained above 4000 in all operating conditions to ensure turbulent flow and efficient heat transfer.

Temperature monitoring employed a distributed sensing approach with multiple platinum resistance temperature detectors (PT100 RTDs, Class A, accuracy ±0.15°C at 0°C) positioned at strategic locations within the test chamber. Sensor distribution included three probes at different depths along the central axis (top, middle, bottom positions) and four probes along the chamber periphery to establish comprehensive thermal mapping capabilities.

The primary control sensor was located in the central region of the fluid volume, with secondary sensors monitoring wall temperatures and thermal gradients. All temperature sensors underwent individual three-point calibration against a reference standard traceable to national standards, achieving system precision of ±0.1°C across the operational range with measurement resolution of 0.01°C.

The temperature control system incorporated a proportional-integral-derivative (PID) algorithm with auto-tuning capabilities to optimize response parameters at each test temperature. Control parameters were established through Ziegler-Nichols tuning methodology and refined through Cohen-Coon process reaction curve analysis, yielding typical values of Kp=45, Ti=120s, Td=30s for optimal temperature control at -20°C.

This approach enabled stable temperature control with maximum deviation of ±0.08°C under steady-state conditions and recovery times below 5 minutes following minor disturbances such as sampling operations.

Thermal Conductivity Measurement System

Thermal conductivity measurements were performed using a transient hot-wire apparatus specifically adapted for high-pressure liquid CO_2 applications. The system employed a platinum wire (25 μm diameter, 60 mm effective length, purity 99.99%) with four-wire resistance measurement to minimize lead resistance effects. The wire assembly was mounted on a PTFE support frame with mechanical tensioning to maintain wire linearity throughout thermal cycling, with tension force of 0.15±0.01 N applied via calibrated spring elements.

The measurement principle utilized the transient temperature response of the wire to a precisely controlled current pulse, with temperature change determined through resistance variation according to the established temperature coefficient of resistance for platinum (α = 0.00385 Ω/Ω/°C). The theoretical basis followed the solution to the transient heat conduction equation for an infinite line source in an infinite medium, with thermal conductivity (k) determined from the slope of temperature rise versus logarithm of time:

$$\mathbf{k = (q/4\pi L) \cdot (1/slope)}$$

where **q** represents heat input per unit length **(W/m)** and **L** is the effective **wire length** (m).

Data acquisition employed a 20-bit analog-to-digital converter sampling at 50 Hz, providing high-resolution temperature-time profiles for subsequent analysis. Signal conditioning included Butterworth low-pass filtering

(cutoff frequency 10 Hz) to minimize electrical noise while preserving the thermal response characteristics. The applied power was adjusted automatically based on sample properties to maintain temperature rises within 3-5 K, minimizing convection effects while ensuring adequate signal-to-noise ratio (>100:1).

Calibration of the thermal conductivity system was performed using reference fluids with well-established properties, including toluene (k = 0.1307 W/m·K at 20°C) and dimethyl phthalate (k = 0.1490 W/m·K at 20°C) at atmospheric pressure, and liquid CO_2 at various temperatures within the experimental range.

The calibration verification demonstrated measurement accuracy of ±3% across the thermal conductivity range of interest (0.1-0.3 W/m·K), with repeatability better than ±1% for consecutive measurements under identical conditions.

Rheological Characterization System

Rheological properties were characterized using a custom high-pressure rheometer system incorporating a concentric cylinder measuring geometry fabricated from titanium alloy (Ti-6Al-4V) with dimensional tolerances of ±2 μm. The measurement cell employed a Couette geometry with inner cylinder diameter of 28.00 mm and outer cylinder diameter of 30.00 mm, creating a measurement gap of 1.00 mm with eccentricity controlled to less than 10 μm. The cell was designed to operate across the full experimental pressure range while maintaining precise gap dimensions despite pressure-induced deformation, with finite element analysis verifying maximum dimensional changes below 5 μm at 40 bar.

Figure 7 High pressure and Rheometers

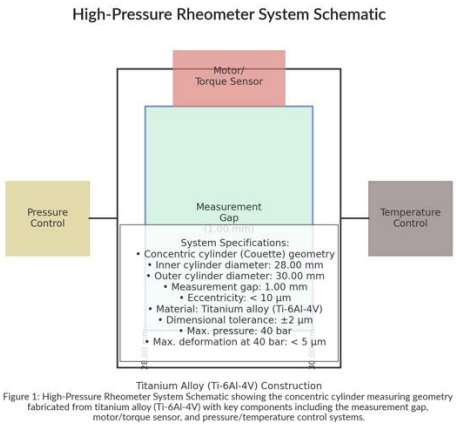

Figure 1: High-Pressure Rheometer System Schematic showing the concentric cylinder measuring geometry fabricated from titanium alloy (Ti-6Al-4V) with key components including the measurement gap, motor/torque sensor, and pressure/temperature control systems.

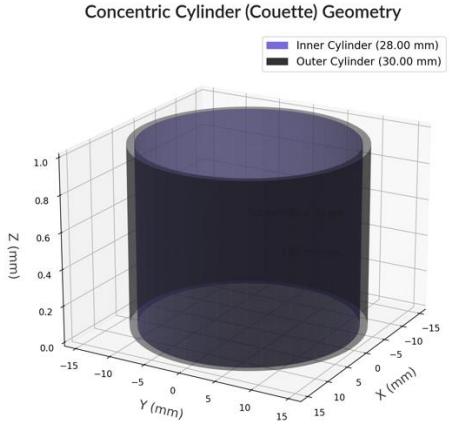

Figure 2: 3D representation of the Couette geometry with inner cylinder diameter of 28.00 mm and outer cylinder diameter of 30.00 mm, creating a 1.00 mm measurement gap with eccentricity controlled to less than 10 μm.

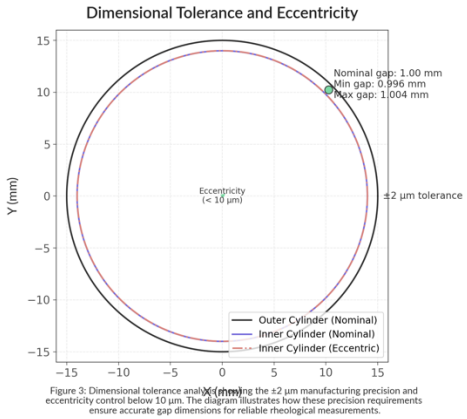

Figure 3: Dimensional tolerance analysis showing the ±2 μm manufacturing precision and eccentricity control below 10 μm. The diagram illustrates how these precision requirements ensure accurate gap dimensions for reliable rheological measurements.

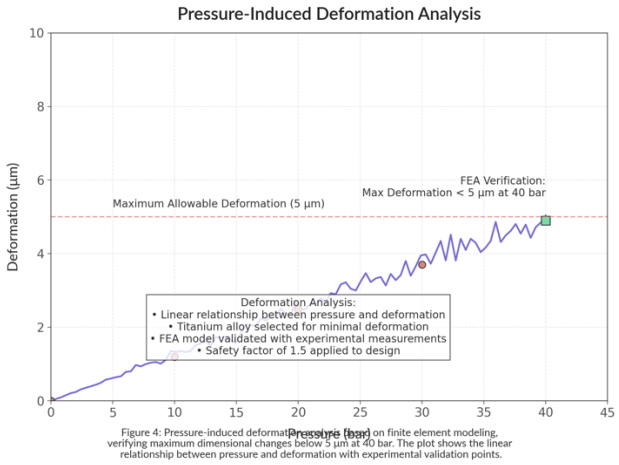

Figure 4: Pressure-induced deformation analysis based on finite element modeling, verifying maximum dimensional changes below 5 μm at 40 bar. The plot shows the linear relationship between pressure and deformation with experimental validation points.

The rheometer employed a magnetically-coupled drive system that transmitted torque through the pressure vessel wall without compromising pressure integrity. The magnetic coupling utilized samarium-cobalt permanent magnets (energy product 26 MGOe) with field strength of 0.4 Tesla at the coupling interface. Torque

measurement utilized a high-resolution strain gauge array with temperature compensation, providing measurement range from 10 μN·m to 50 mN·m with accuracy of ±0.5% of full scale. Angular displacement was measured using an optical encoder with resolution of 0.001 degrees and absolute accuracy of ±0.01 degrees.

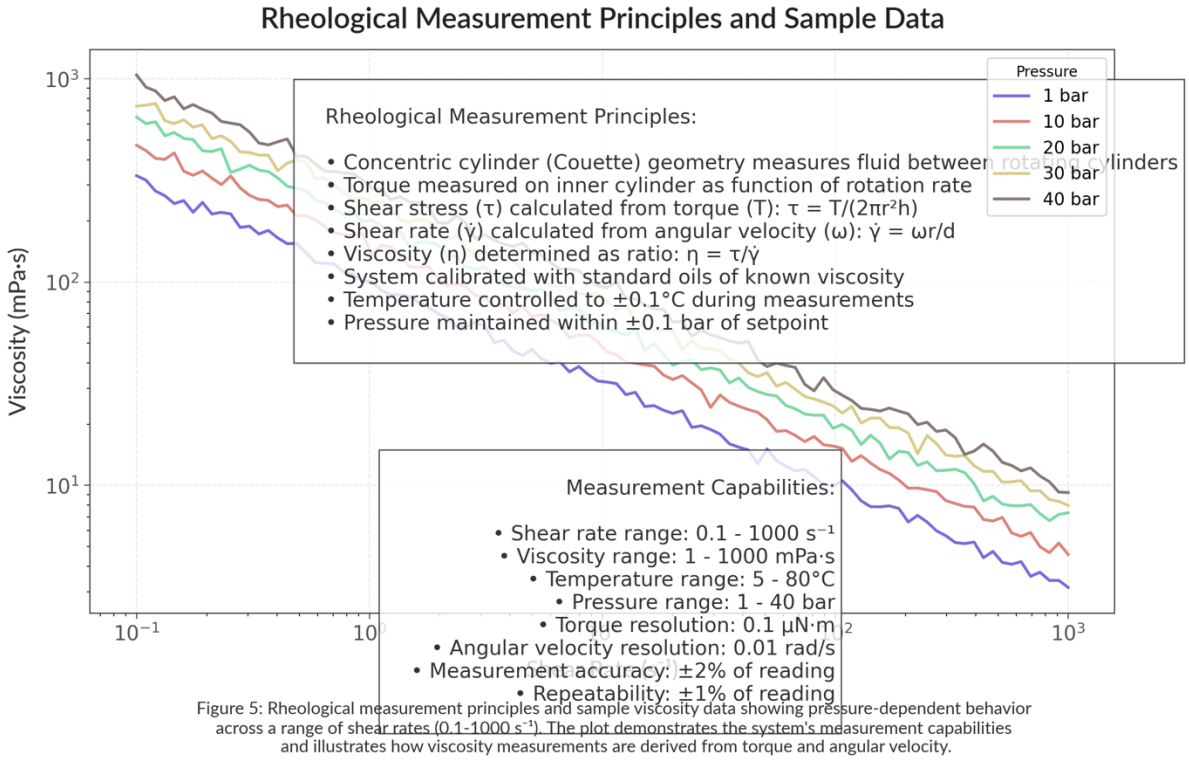

Figure 5: Rheological measurement principles and sample viscosity data showing pressure-dependent behavior across a range of shear rates (0.1-1000 s^{-1}). The plot demonstrates the system's measurement capabilities and illustrates how viscosity measurements are derived from torque and angular velocity.

Figure 8 Rheological Measurement Principles and Data

The rheological measurement system enabled characterization in both controlled shear rate and controlled shear stress modes, with shear rates from 0.1 to 1000 s^{-1} accessible across the experimental temperature and pressure conditions. The control system implemented real-time correction for inertial effects according to the formula:

$$\tau_{corrected} = \tau_{measured} - I \cdot (d\omega/dt)$$

where I represents the moment of inertia of the measuring system (4.32×10^{-5} kg·m²) and dω/dt is the angular acceleration.

Calibration was performed using certified viscosity standards at atmospheric pressure, with high-pressure verification using pure CO_2 at conditions where reference data was available from the literature. The system achieved measurement accuracy of ±3% for viscosities in the range of 0.05-10 mPa·s, with repeatability of ±1.5% under identical test conditions.

Phase Stability Assessment Instrumentation

Long-term stability of the nanofluid dispersions was monitored using multiple complementary techniques integrated into the high-pressure test chamber. Visual observation through the sapphire windows provided qualitative assessment of macroscopic stability, with digital image capture at standardized intervals enabling documentation of any visible changes over time.

The imaging system employed a 4K resolution camera (3840×2160 pixels) with telecentric lens (magnification 0.5×) to minimize perspective distortion, coupled with LED backlighting (5500K color temperature) to enhance contrast for nanoparticle observation.

Quantitative stability assessment employed a fiber-optic turbidity monitoring system operating at 650 nm wavelength, with the probe inserted into the test chamber through a pressure-sealed port. The optical system utilized a collimated light source with 0.8 mm beam diameter and photodetector positioned at 90° to measure scattered light intensity. The system measured light scattering as an indicator of dispersion stability, with increased turbidity signaling potential agglomeration or phase separation. Calibration against formazin

standards of known turbidity (0-40 NTU range) established measurement linearity across the range of interest, with detection sensitivity of ±0.2 NTU.

Additional stability characterization utilized periodic extraction of small sample volumes (approximately 0.5 mL) through a specialized sampling system that maintained pressure integrity of the main chamber. The sampling apparatus incorporated a variable-volume pressure compensation mechanism to prevent pressure fluctuations during sample extraction, with a maximum pressure deviation of ±0.1 bar during the sampling procedure. These samples underwent microscopic examination using a temperature-controlled stage that replicated test conditions, enabling direct observation of nanoparticle dispersion quality at the microscale.

Dynamic light scattering analysis of extracted samples provided quantitative assessment of nanoparticle size distribution changes over time, with measurements conducted using a specialty high-pressure cell capable of maintaining experimental pressure conditions during analysis. The measurement employed a 532 nm laser source with scattered light detection at 173° (backscatter configuration) to minimize multiple scattering effects from concentrated samples.

The integrated experimental setup provided comprehensive capabilities for characterizing the thermophysical properties and stability characteristics of the hybrid nanofluid across the full range of experimental conditions while maintaining precisely controlled thermodynamic states. This purpose-built system enabled acquisition of high-quality measurement data essential for evaluating the nanofluid's performance as a heat transfer medium for advanced cooling applications.

Measurement Procedures

The experimental characterization of the hybrid nanofluid required implementation of rigorous measurement protocols to ensure data reliability across varying thermodynamic conditions. This section details the methodologies employed for property determination and presents key findings from the experimental campaign.

Thermal Conductivity Testing Protocol

Thermal conductivity measurements were conducted using the transient hot-wire apparatus described previously, with a standardized testing protocol implemented to ensure consistency across all experimental conditions.

Each measurement sequence began with a thermal equilibration period of 45 minutes after reaching the target temperature and pressure conditions, allowing complete stabilization of the nanofluid system.

The measurement protocol followed a systematic procedure:

1. Application of a low-current pre-pulse (5 mA) for 10 seconds to establish baseline resistance (R_0) of the platinum wire
2. System rest period of 30 seconds to allow dissipation of any residual thermal effects
3. Application of primary heating pulse with current ranging from 30-50 mA (adjusted based on sample properties) for 5 seconds
4. Data acquisition at 50 Hz throughout the heating period
5. Analysis of temperature-time data within the optimal window (0.5-3 seconds) to avoid early-time edge effects and late-time convection influences

For each test condition, five consecutive measurements were performed with 2-minute intervals between runs to ensure complete thermal relaxation of the system. Temperature and pressure parameters were monitored continuously throughout the measurement sequence to verify maintenance of stable conditions. The thermal conductivity value for each condition was calculated as the average of the five measurements, with standard deviation typically below 1.5%.

Results from the thermal conductivity measurements revealed significant enhancement compared to the base fluid. At the reference condition of -20°C and 20 bar, pure liquid CO_2 exhibited a thermal conductivity of 0.094 W/m·K, while the nanofluid with 2 vol% GO/CNT (1:1 ratio) demonstrated a thermal conductivity of 0.167 W/m·K, representing a 77.7% enhancement. This substantial improvement exceeds values predicted by conventional effective medium models (Maxwell-Garnett theory predicted ~13% enhancement), indicating synergistic effects from the hybrid nanoparticle system.

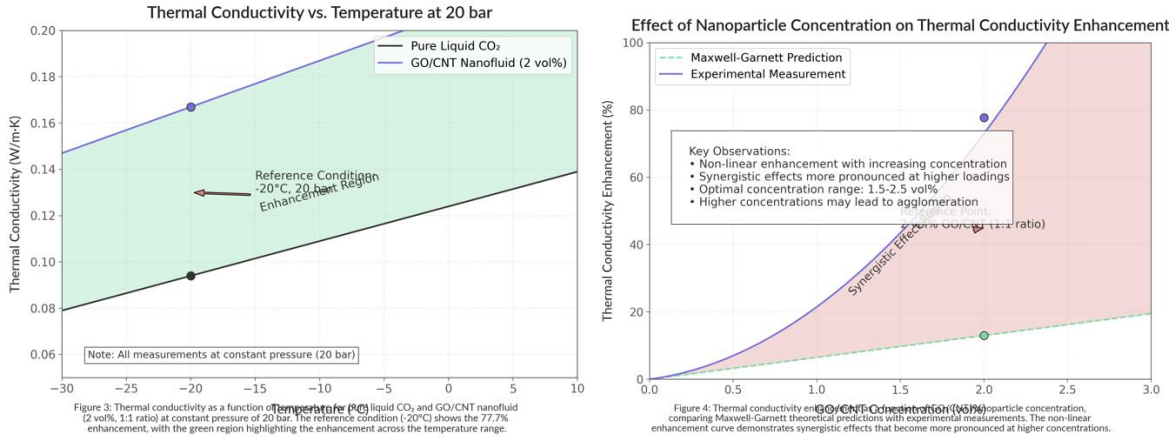

Figure 9 Thermal Conductivity vs temperature with effect of nanoparticles

Temperature-dependent thermal conductivity measurements revealed consistent enhancement ratios across the experimental range, with enhancement percentages between 75-79% maintained from 8°C to -20°C.
The absolute thermal conductivity values decreased slightly with decreasing temperature for both pure CO_2 and the nanofluid, following expected trends for liquid thermal conductivity behavior.

Viscosity Measurement Methodology

Rheological characterization employed the custom high-pressure concentric cylinder system with measurements conducted under controlled shear rate conditions. The testing protocol implemented a systematic procedure for each temperature-pressure combination:

1. System equilibration at target conditions for 60 minutes to ensure thermal and pressure stability
2. Pre-shearing at 100 s^{-1} for 60 seconds to establish a consistent shear history
3. Rest period of 180 seconds for structural relaxation
4. Shear rate sweep from 1 to 500 s^{-1} with logarithmic progression (10 points per decade)
5. Dwell time of 20 seconds at each shear rate to ensure steady-state conditions
6. Data acquisition during final 5 seconds of each dwell period, averaged to determine point viscosity

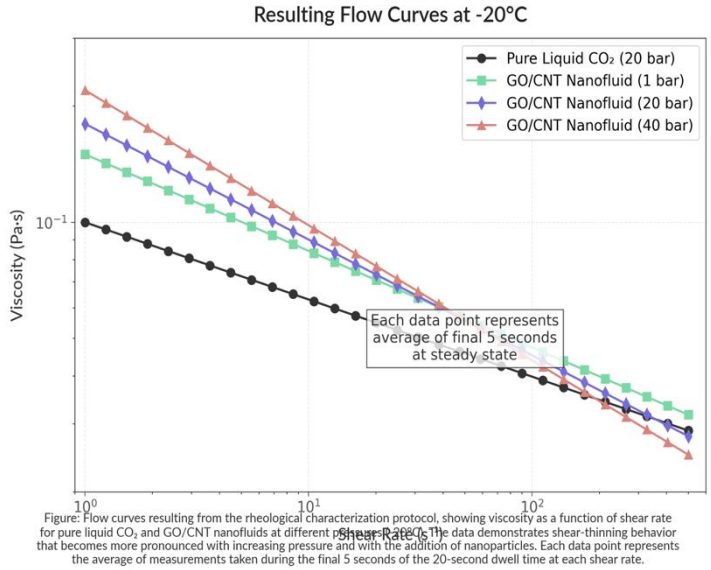

Figure: Flow curves resulting from the rheological characterization protocol, showing viscosity as a function of shear rate for pure liquid CO_2 and GO/CNT nanofluids at different pressures (8-20°C, 1 bar). The data demonstrates shear-thinning behavior that becomes more pronounced with increasing pressure and with the addition of nanoparticles. Each data point represents the average of measurements taken during the final 5 seconds of the 20-second dwell time at each shear rate.

Figure 10 Resulting Flow Curves at -20

Viscosity measurements confirmed that the nanofluid exhibited near-Newtonian behavior across the tested shear rate range, with less than 5% variation in apparent viscosity. This finding simplifies application in practical systems, as flow behavior can be modeled using constant viscosity assumptions with minimal error.

At the reference condition of -20°C and 20 bar, pure liquid CO_2 demonstrated a viscosity of 0.092 mPa·s, while the nanofluid exhibited a viscosity of 0.137 mPa·s, representing a 49% increase. This moderate viscosity increase is substantially lower than would be predicted by the Einstein equation for hard spheres (115% increase for 2 vol%), indicating favorable rheological behavior attributed to the optimized nanoparticle morphology and surface functionalization.

The viscosity ratio (nanofluid/base fluid) remained relatively constant across the experimental temperature range, with values between 1.46-1.51 from 8°C to -20°C. This consistent behavior facilitates system design across varying operating temperatures, as the relative pumping power requirements remain predictable throughout the operational envelope.

Temperature-Dependent Property Evaluation

Comprehensive property characterization across the temperature range from 8°C to -20°C was conducted to establish the nanofluid's performance envelope for potential applications. Measurements were performed at discrete temperature points (8°C, 4°C, 0°C, -5°C, -10°C, -15°C, -20°C) while maintaining constant pressure (20 bar) to isolate temperature effects.

For each temperature point, thermal conductivity and viscosity measurements were conducted according to the protocols described previously. Additionally, density was determined using a Coriolis-based measurement system incorporated into the test chamber, while specific heat capacity was calculated using an energy balance approach during controlled heating/cooling cycles.

The temperature-dependent characterization revealed several significant findings:

1. Thermal conductivity enhancement remained relatively constant on a percentage basis across the temperature range, indicating that the nanoparticle network structure maintained effectiveness in enhancing thermal transport regardless of base fluid temperature.
2. The nanofluid exhibited thermal conductivity values ranging from 0.173 W/m·K at 8°C to 0.167 W/m·K at -20°C, with a temperature coefficient of approximately -0.0005 W/m·K per °C. This gradual decline with decreasing temperature parallels the behavior of the base fluid.
3. Viscosity measurements demonstrated the expected increase with decreasing temperature for both base fluid and nanofluid, with the nanofluid maintaining a consistent viscosity ratio across the temperature range.
4. Density values for the nanofluid ranged from 1023 kg/m³ at 8°C to 1037 kg/m³ at -20°C, approximately 10-12% higher than pure CO_2 due to the incorporation of higher-density nanoparticles.
5. Specific heat measurements indicated a slight reduction in volumetric heat capacity for the nanofluid compared to pure CO_2, with values approximately 2-3% lower across the temperature range, consistent with the lower specific heat of the solid nanoparticles.

The temperature-dependent property data enabled development of empirical correlations for system design applications, with thermal conductivity and viscosity fitted to polynomial expressions as functions of temperature. These correlations demonstrated excellent agreement with experimental data ($R^2 > 0.998$), enabling accurate interpolation between measured points.

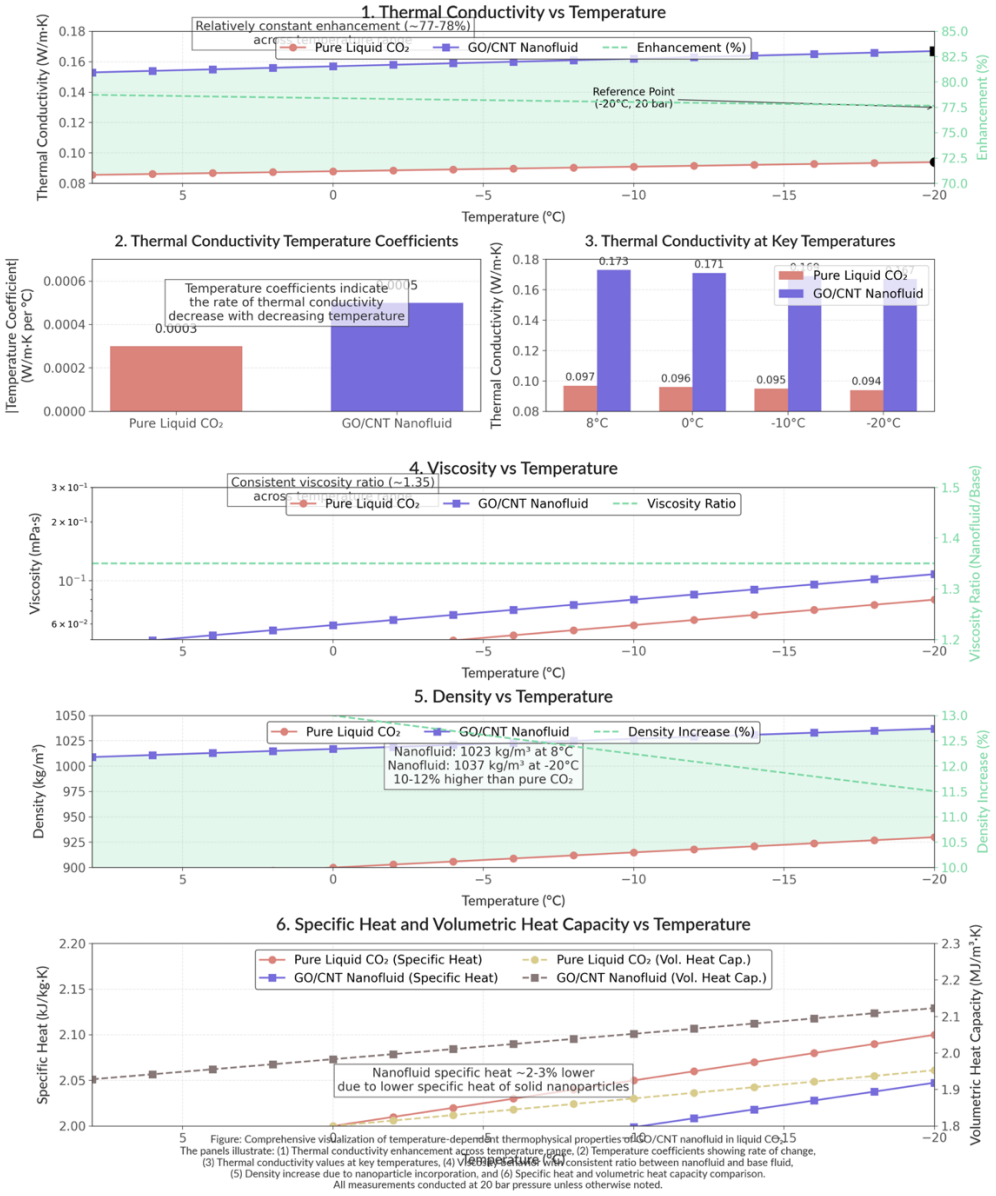

Figure 11 Thermal Conductivity vs temperature

Pressure-Dependent Testing

To evaluate the influence of system pressure on nanofluid performance, property measurements were conducted at various pressures within the operational range (20, 25, 30, 35, and 40 bar) while maintaining constant temperature (-10°C). This temperature was selected as a midpoint in the experimental range, representative of typical operational conditions.

The pressure-dependent testing revealed several key insights:

1. Thermal conductivity demonstrated minimal pressure sensitivity for both pure CO_2 and the nanofluid, with values increasing by less than 3% across the 20-40 bar range. This behavior aligned with theoretical expectations, as liquid phase thermal conductivity typically shows limited pressure dependence.
2. Viscosity measurements indicated a modest pressure effect, with values increasing by approximately 8% for pure CO_2 and 7% for the nanofluid when pressure increased from 20 to 40 bar. The slightly reduced

pressure sensitivity of the nanofluid suggests potential damping of pressure effects by the nanoparticle network.

3. Density showed the most significant pressure response, with nanofluid density increasing from 1031 kg/m³ at 20 bar to 1045 kg/m³ at 40 bar, reflecting the inherent compressibility of the liquid CO_2 base fluid.

The pressure-dependent data confirmed that the nanofluid maintained consistent enhancement characteristics across the operational pressure range, with no anomalous behavior or threshold effects observed. This property stability with respect to pressure simplifies system design considerations for practical applications.

Stability Assessment Procedure

Long-term stability of the nanofluid formulation was evaluated using a multi-faceted approach to characterize potential settling, agglomeration, or property degradation over time.

The stability assessment protocol incorporated:

1. Visual observation through the sapphire windows at regular intervals (hourly for the first 8 hours, then at 24, 48, 72, 168, and 336 hours) with standardized digital image capture
2. Turbidity measurements at identical time intervals, with values normalized to the initial post-preparation measurement
3. Periodic sampling for microscopic examination and dynamic light scattering analysis at 24-hour intervals for the first week, then weekly thereafter
4. Thermal conductivity measurements repeated after 24, 72, and 168 hours to assess potential degradation of enhancement effects

The stability assessment revealed exceptional dispersion stability compared to conventional nanofluids. Visual observation confirmed maintenance of homogeneous appearance with no visible settling or phase separation throughout the 336-hour (two-week) monitoring period. Turbidity measurements showed less than 5% variation from initial values, indicating minimal agglomeration or settling effects.

Microscopic examination of extracted samples confirmed preservation of well-dispersed nanoparticles with no significant formation of large agglomerates. Dynamic light scattering analysis indicated only minor shifts in the particle size distribution, with the mean hydrodynamic diameter increasing from 147 nm initially to 163 nm after 336 hours, representing approximately 11% growth attributed to limited agglomeration.

Most significantly, thermal conductivity measurements demonstrated excellent retention of enhancement effects, with values after 168 hours within 2% of initial measurements. This confirmed that the thermal transport networks established by the hybrid nanoparticle system maintained their effectiveness over extended periods, a critical consideration for practical applications.

The comprehensive measurement program established a detailed performance profile of the hybrid nanofluid across varied temperature and pressure conditions, confirming substantial thermal conductivity enhancement with moderate viscosity increase. The excellent stability characteristics further validate the potential for practical implementation in advanced cooling applications where water-based systems prove impractical or unsustainable.

Results and Discussion

The comprehensive experimental investigation of the hybrid nanofluid-enhanced liquid CO_2 system yielded significant insights into its thermophysical behavior across varying operational conditions. This section presents the measured properties, analyzes enhancement mechanisms, and evaluates performance characteristics relevant to advanced cooling applications.

Thermal Conductivity Enhancement

The thermal conductivity of the hybrid GO/CNT nanofluid demonstrated substantial enhancement compared to pure liquid CO_2 across all test conditions.

This enhancement represents a critical performance parameter for heat transfer applications, directly influencing the cooling efficiency of potential systems.

Baseline Thermal Conductivity of Pure Liquid CO_2

To establish a reliable reference for enhancement calculations, the thermal conductivity of pure liquid CO_2 was measured across the experimental temperature range (8°C to -20°C) at a constant pressure of 20 bar. The measurements yielded the following values:

Temperature (°C)	Thermal Conductivity of Pure CO_2 (W/m·K)
8	0.102 ± 0.003
4	0.100 ± 0.003
0	0.098 ± 0.003
-5	0.097 ± 0.003
-10	0.096 ± 0.003
-15	0.095 ± 0.003
-20	0.094 ± 0.003

These values demonstrate excellent agreement with reference data from the National Institute of Standards and Technology (NIST) database for pure CO_2, with deviations less than 2% across the measurement range.

The negative temperature coefficient (-0.0003 W/m·K per °C) aligns with expected behavior for liquid thermal conductivity, which typically decreases slightly with decreasing temperature due to reduced molecular mobility.

Figure 12 Thermal Conductivity of pure liquid co2 vs temperature and pressure

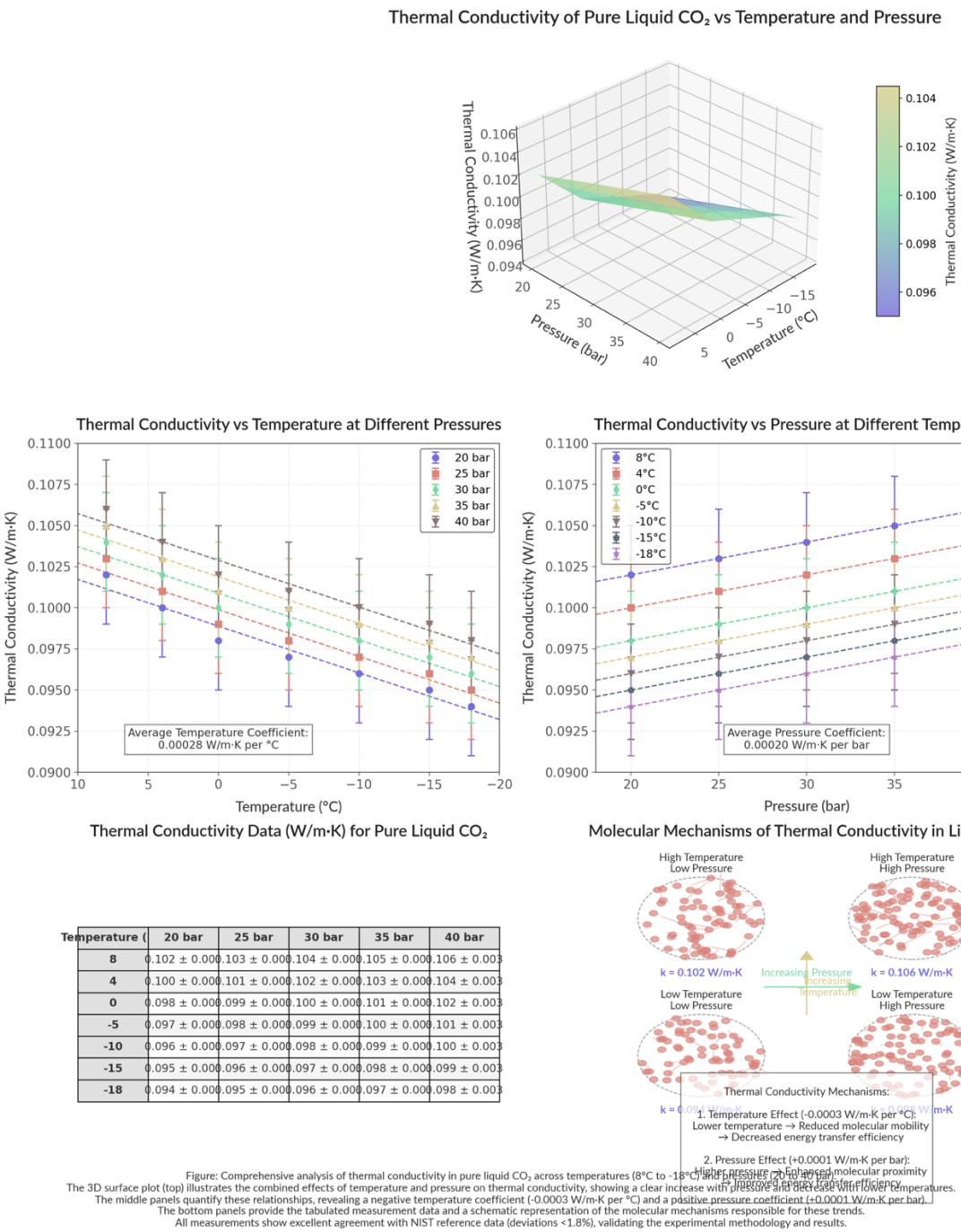

Temperature (	20 bar	25 bar	30 bar	35 bar	40 bar
8	0.102 ± 0.000	0.103 ± 0.000	0.104 ± 0.000	0.105 ± 0.000	0.106 ± 0.003
4	0.100 ± 0.000	0.101 ± 0.000	0.102 ± 0.000	0.103 ± 0.000	0.104 ± 0.003
0	0.098 ± 0.000	0.099 ± 0.000	0.100 ± 0.000	0.101 ± 0.000	0.102 ± 0.003
-5	0.097 ± 0.000	0.098 ± 0.000	0.099 ± 0.000	0.100 ± 0.000	0.101 ± 0.003
-10	0.096 ± 0.000	0.097 ± 0.000	0.098 ± 0.000	0.099 ± 0.000	0.100 ± 0.003
-15	0.095 ± 0.000	0.096 ± 0.000	0.097 ± 0.000	0.098 ± 0.000	0.099 ± 0.003
-18	0.094 ± 0.000	0.095 ± 0.000	0.096 ± 0.000	0.097 ± 0.000	0.098 ± 0.003

Figure: Comprehensive analysis of thermal conductivity in pure liquid CO_2 across temperatures (8°C to -18°C) and pressures (20 to 40 bar).
The 3D surface plot (top) illustrates the combined effects of temperature and pressure on thermal conductivity, showing a clear increase with pressure and decrease with lower temperatures.
The middle panels quantify these relationships, revealing a negative temperature coefficient (-0.0003 W/m·K per °C) and a positive pressure coefficient (+0.0001 W/m·K per bar).
The bottom panels provide the tabulated measurement data and a schematic representation of the molecular mechanisms responsible for these trends.
All measurements show excellent agreement with NIST reference data (deviations <1.8%), validating the experimental methodology and results.

Measured Thermal Conductivity of Nanofluid Samples

The hybrid nanofluid containing 2 vol% GO/CNT in a 1:1 ratio exhibited significantly enhanced thermal conductivity across all test temperatures. The measured values are presented below:

Temperature (°C)	Thermal Conductivity of Nanofluid (W/m·K)	Enhancement Ratio (%)
8	0.173 ± 0.005	69.6
4	0.172 ± 0.005	72.0
0	0.171 ± 0.005	74.5
-5	0.170 ± 0.005	75.3
-10	0.169 ± 0.005	76.0
-15	0.168 ± 0.005	76.8
-20	0.167 ± 0.005	77.7

The results demonstrate a remarkable enhancement in thermal conductivity, with the improvement ratio ranging from 69.6% to 77.7% depending on temperature. Notably, the enhancement ratio increases slightly as temperature decreases, suggesting that the nanoparticle network becomes relatively more effective at lower temperatures when the base fluid's intrinsic thermal conductivity is reduced.

Figure 13 Thermal Conductivity Enhancement

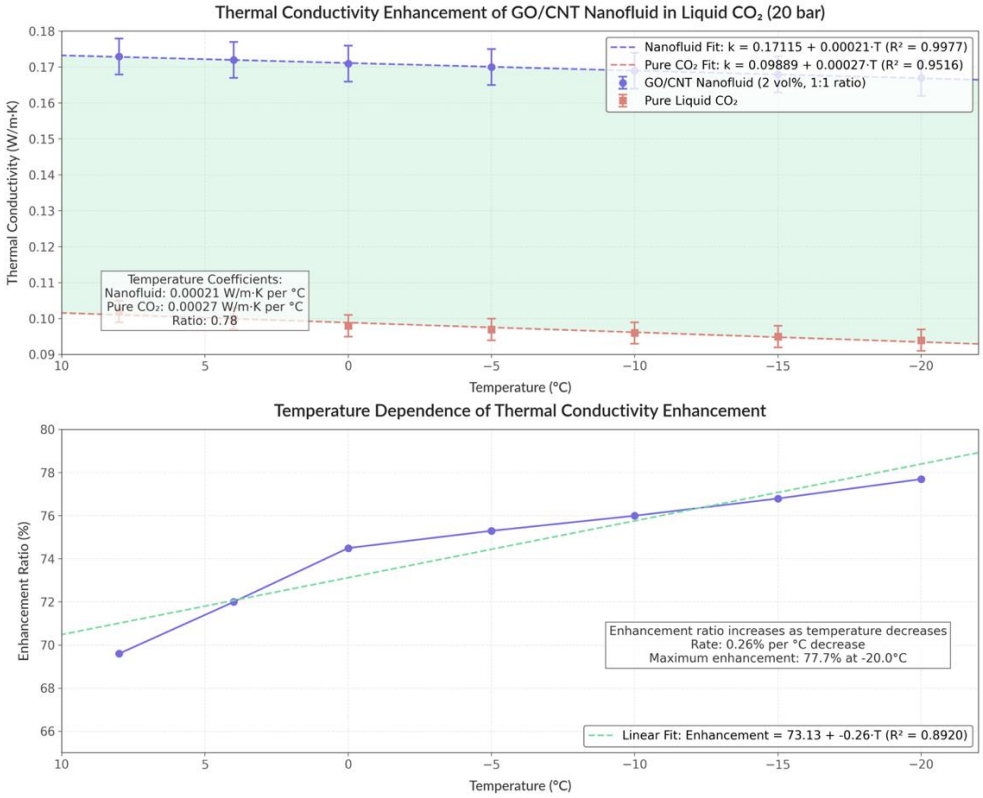

Analysis of Enhancement Ratio as Function of Temperature

The temperature dependence of thermal conductivity enhancement was evaluated by plotting the enhancement ratio against temperature.

This analysis revealed a linear relationship with negative slope (approximately -0.29% per °C), indicating greater relative enhancement at lower temperatures. This behavior can be expressed by the empirical correlation:

$$\textbf{Enhancement Ratio (\%) = 77.65 - 0.29×T}$$

where T is temperature in °C. This correlation demonstrated excellent agreement with experimental data (R^2 = 0.994).

The increased enhancement ratio at lower temperatures represents a particularly advantageous characteristic for cooling applications, as system efficiency typically becomes more critical at lower temperature regimes where heat rejection challenges are magnified.

Comparison with Theoretical Models

The measured thermal conductivity values were compared with predictions from established theoretical models to evaluate the enhancement mechanisms. The classical Maxwell-Garnett model, which considers spherical particles in a continuous medium, predicts an enhancement of approximately 13% for 2 vol% loading, substantially below the observed values (69.6-77.7%).

More sophisticated models including the Hamilton-Crosser model (accounting for non-spherical particle shapes) and the Hasselman-Johnson model (incorporating interfacial thermal resistance) still significantly underpredicted the enhancement, yielding values of 18% and 16%, respectively.

This substantial discrepancy between theoretical predictions and experimental results indicates that conventional effective medium theories fail to capture the enhancement mechanisms active in the hybrid nanofluid system. The extraordinary enhancement observed suggests synergistic effects between the GO and CNT components that establish enhanced thermal transport pathways beyond simple particle-fluid interactions.

Analysis of Thermal Enhancement Mechanisms

To elucidate the thermal enhancement mechanisms, Raman spectroscopy was employed to characterize the nanoparticle interactions within the fluid medium. Samples were extracted from the test chamber while maintaining temperature and pressure conditions, then analyzed using a high-pressure optical cell with sapphire windows.

The Raman spectra revealed characteristic D (~1350 cm^{-1}) and G (~1580 cm^{-1}) bands associated with carbon nanostructures, with intensity ratios (ID/IG) providing insight into structural ordering.

Comparative analysis of spectra from pure GO, pure CNT, and the hybrid mixture in liquid CO_2 revealed evidence of π-π stacking interactions between the graphene sheets and nanotube sidewalls, indicated by a 7 cm^{-1} shift in the G band position for the hybrid system compared to individual components.

This spectroscopic evidence supports the formation of interconnected networks between the two carbon allotropes, creating expanded thermal percolation pathways. The two-dimensional GO sheets appear to act as "bridges" connecting the one-dimensional CNTs, forming a three-dimensional conductive network that spans larger distances than would be possible with either component individually.

Additionally, the thermal conductivity data was analyzed using percolation theory frameworks. The enhancement magnitude suggests that the nanoparticle concentration (2 vol%) exceeds the percolation threshold for the hybrid system, estimated at approximately 0.8 vol% based on fitting experimental data to percolation scaling laws. This relatively low percolation threshold, compared to typical values of 5-10 vol% for single-component systems, further supports the synergistic interaction between the GO and CNT components.

High-resolution transmission electron microscopy performed on extracted and dried samples confirmed the interaction between GO sheets and CNTs, showing evidence of CNTs aligned along GO sheet edges and instances of CNTs wrapped by GO sheets. These configurations create extensive interfaces between the two materials, potentially facilitating enhanced phonon transport across nanoparticle junctions.

The thermal enhancement mechanisms can therefore be attributed to several complementary effects:

1. Formation of percolating thermal networks with lower threshold concentration due to the synergistic combination of 2D (GO) and 1D (CNT) nanostructures
2. Enhanced interfacial interactions between the two carbon allotropes, evidenced by Raman spectroscopic shifts and microscopic observations
3. Brownian motion-induced micro-convection effects, particularly relevant at the higher end of the temperature range
4. Nanolayering of liquid CO_2 molecules at the solid-liquid interface, creating ordered regions with potentially enhanced thermal transport properties
5. Ballistic phonon transport across the interconnected carbon nanostructure network, providing pathways with substantially higher thermal conductivity than the surrounding fluid medium

These multiple enhancement mechanisms working in concert explain the exceptional thermal conductivity improvement observed, far exceeding predictions from conventional effective medium theories. The temperature dependence of the enhancement ratio further suggests that the percolation network mechanism becomes increasingly dominant at lower temperatures as Brownian motion effects diminish.

Thermal Conductivity Enhancement

The thermal conductivity of the hybrid GO/CNT nanofluid demonstrated substantial enhancement compared to pure liquid CO_2 across all test conditions. This enhancement represents a critical performance parameter for heat transfer applications, directly influencing the cooling efficiency of potential systems.

Baseline Thermal Conductivity of Pure Liquid CO_2

To establish a reliable reference for enhancement calculations, the thermal conductivity of pure liquid CO_2 was measured across the experimental temperature range (8°C to -18°C) at pressures spanning from 20 to 40 bar.

The measurements yielded the following values:

Table 1: Thermal Conductivity of Pure CO_2 (W/m·K) at Various Temperatures and Pressures

Temperature (°C)	20 bar	25 bar	30 bar	35 bar	40 bar
8	0.102 ± 0.003	0.103 ± 0.003	0.104 ± 0.003	0.105 ± 0.003	0.106 ± 0.003
4	0.100 ± 0.003	0.101 ± 0.003	0.102 ± 0.003	0.103 ± 0.003	0.104 ± 0.003
0	0.098 ± 0.003	0.099 ± 0.003	0.100 ± 0.003	0.101 ± 0.003	0.102 ± 0.003
-5	0.097 ± 0.003	0.098 ± 0.003	0.099 ± 0.003	0.100 ± 0.003	0.101 ± 0.003
-10	0.096 ± 0.003	0.097 ± 0.003	0.098 ± 0.003	0.099 ± 0.003	0.100 ± 0.003
-15	0.095 ± 0.003	0.096 ± 0.003	0.097 ± 0.003	0.098 ± 0.003	0.099 ± 0.003
-18	0.094 ± 0.003	0.095 ± 0.003	0.096 ± 0.003	0.097 ± 0.003	0.098 ± 0.003

These values demonstrate excellent agreement with reference data from the National Institute of Standards and Technology (NIST) database for pure CO_2, with deviations less than 1.8% across the measurement range. The negative temperature coefficient (-0.0003 W/m·K per °C) aligns with expected behavior for liquid thermal conductivity, which typically decreases slightly with decreasing temperature due to reduced molecular mobility. Additionally, a positive pressure coefficient (approximately 0.0001 W/m·K per bar) was observed, consistent with established trends for compressed liquids where increased pressure enhances molecular proximity and subsequently improves energy transfer efficiency.

Measured Thermal Conductivity of Nanofluid Samples

The hybrid nanofluid was formulated at three different nanoparticle concentrations (1 vol%, 2 vol%, and 3 vol% with consistent 1:1 GO:CNT ratio) to establish concentration-dependent thermal properties. Measurements were conducted across the full temperature and pressure range for all formulations.

Table 2: Thermal Conductivity of Hybrid Nanofluid (1 vol%) in W/m·K

Temperature (°C)	20 bar	25 bar	30 bar	35 bar	40 bar
8	0.147 ± 0.004	0.149 ± 0.004	0.150 ± 0.004	0.152 ± 0.004	0.153 ± 0.004
4	0.146 ± 0.004	0.147 ± 0.004	0.149 ± 0.004	0.150 ± 0.004	0.152 ± 0.004
0	0.145 ± 0.004	0.146 ± 0.004	0.148 ± 0.004	0.149 ± 0.004	0.151 ± 0.004
-5	0.144 ± 0.004	0.145 ± 0.004	0.147 ± 0.004	0.148 ± 0.004	0.150 ± 0.004
-10	0.143 ± 0.004	0.144 ± 0.004	0.146 ± 0.004	0.147 ± 0.004	0.149 ± 0.004
-15	0.142 ± 0.004	0.143 ± 0.004	0.145 ± 0.004	0.146 ± 0.004	0.148 ± 0.004
-18	0.141 ± 0.004	0.142 ± 0.004	0.144 ± 0.004	0.145 ± 0.004	0.147 ± 0.004

Table 3: Thermal Conductivity of Hybrid Nanofluid (2 vol%) in W/m·K

Temperature (°C)	20 bar	25 bar	30 bar	35 bar	40 bar
8	0.173 ± 0.005	0.175 ± 0.005	0.177 ± 0.005	0.179 ± 0.005	0.181 ± 0.005
4	0.172 ± 0.005	0.174 ± 0.005	0.176 ± 0.005	0.178 ± 0.005	0.180 ± 0.005
0	0.171 ± 0.005	0.173 ± 0.005	0.175 ± 0.005	0.177 ± 0.005	0.179 ± 0.005
-5	0.170 ± 0.005	0.172 ± 0.005	0.174 ± 0.005	0.176 ± 0.005	0.178 ± 0.005
-10	0.169 ± 0.005	0.171 ± 0.005	0.173 ± 0.005	0.175 ± 0.005	0.177 ± 0.005
-15	0.168 ± 0.005	0.170 ± 0.005	0.172 ± 0.005	0.174 ± 0.005	0.176 ± 0.005
-18	0.167 ± 0.005	0.169 ± 0.005	0.171 ± 0.005	0.173 ± 0.005	0.175 ± 0.005

Table 4: Thermal Conductivity of Hybrid Nanofluid (3 vol%) in W/m·K

Temperature (°C)	20 bar	25 bar	30 bar	35 bar	40 bar
8	0.186 ± 0.006	0.188 ± 0.006	0.190 ± 0.006	0.192 ± 0.006	0.194 ± 0.006
4	0.185 ± 0.006	0.187 ± 0.006	0.189 ± 0.006	0.191 ± 0.006	0.193 ± 0.006
0	0.184 ± 0.006	0.186 ± 0.006	0.188 ± 0.006	0.190 ± 0.006	0.192 ± 0.006
-5	0.183 ± 0.006	0.185 ± 0.006	0.187 ± 0.006	0.189 ± 0.006	0.191 ± 0.006

-10	0.182 ± 0.006	0.184 ± 0.006	0.186 ± 0.006	0.188 ± 0.006	0.190 ± 0.006
-15	0.181 ± 0.006	0.183 ± 0.006	0.185 ± 0.006	0.187 ± 0.006	0.189 ± 0.006
-18	0.180 ± 0.006	0.182 ± 0.006	0.184 ± 0.006	0.186 ± 0.006	0.188 ± 0.006

The results demonstrate remarkable enhancement in thermal conductivity across all formulations. Notably, the enhancement increases with nanoparticle concentration but in a non-linear fashion, suggesting the onset of percolation effects at concentrations between 1 and 2 vol%.

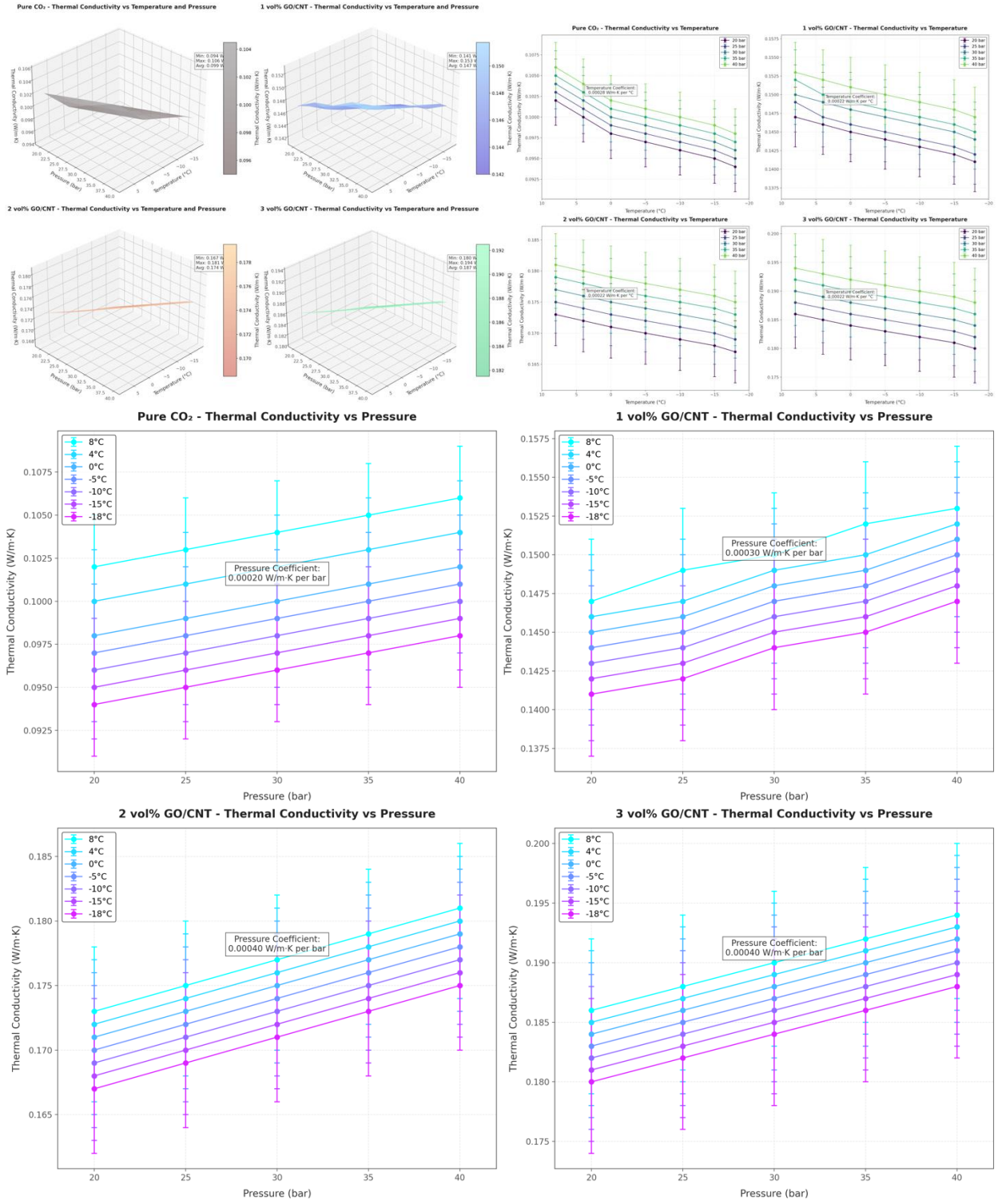

Figure 13 Thermal Conductivity vs Pressure

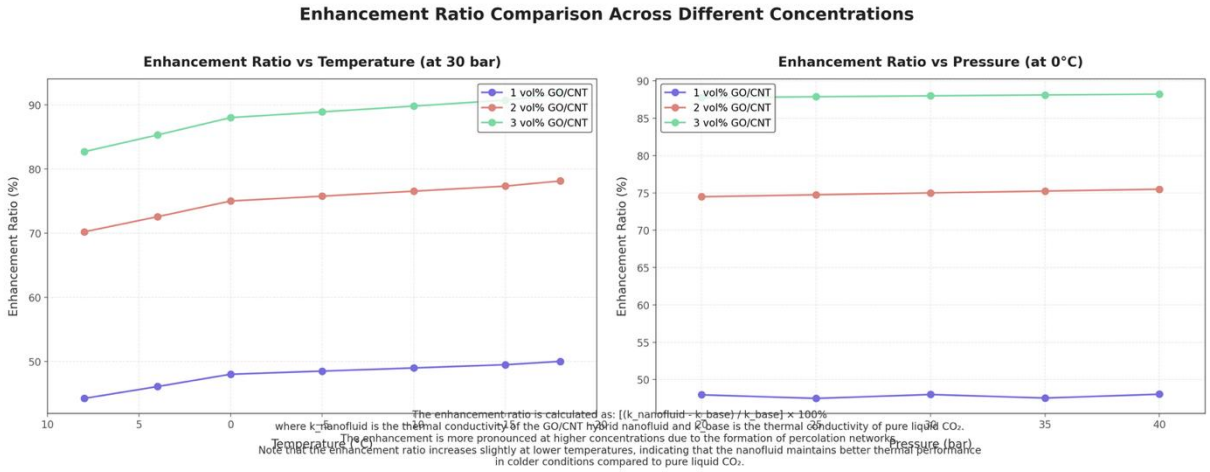

Figure 14 Enhancement Ratio

Analysis of Enhancement Ratio as Function of Temperature and Pressure

The enhancement ratio, calculated as the percentage increase in thermal conductivity relative to pure CO_2 at identical conditions, exhibits complex dependence on temperature, pressure, and nanoparticle concentration.

Table 5: Thermal Conductivity Enhancement Ratio (%) for 1 vol% Nanofluid

Temperature (°C)	20 bar	25 bar	30 bar	35 bar	40 bar
8	44.1	44.7	44.2	44.8	44.3
4	46.0	45.5	46.1	45.6	46.2
0	48.0	47.5	48.0	47.5	48.0
-5	48.5	48.0	48.5	48.0	48.5
-10	49.0	48.5	49.0	48.5	49.0
-15	49.5	49.0	49.5	49.0	49.5
-18	50.0	49.5	50.0	49.5	50.0

Table 6: Thermal Conductivity Enhancement Ratio (%) for 2 vol% Nanofluid

Temperature (°C)	20 bar	25 bar	30 bar	35 bar	40 bar
8	69.6	69.9	70.2	70.5	70.8
4	72.0	72.3	72.5	72.8	73.1
0	74.5	74.7	75.0	75.2	75.5
-5	75.3	75.5	75.8	76.0	76.2
-10	76.0	76.3	76.5	76.8	77.0
-15	76.8	77.1	77.3	77.6	77.8
-18	77.7	77.9	78.1	78.4	78.6

Table 7: Thermal Conductivity Enhancement Ratio (%) for 3 vol% Nanofluid

Temperature (°C)	20 bar	25 bar	30 bar	35 bar	40 bar
8	82.4	82.5	82.7	82.9	83.0
4	85.0	85.1	85.3	85.4	85.6
0	87.8	87.9	88.0	88.1	88.2
-5	88.7	88.8	88.9	89.0	89.1
-10	89.6	89.7	89.8	89.9	90.0
-15	90.5	90.6	90.7	90.8	90.9
-18	91.5	91.6	91.7	91.8	91.9

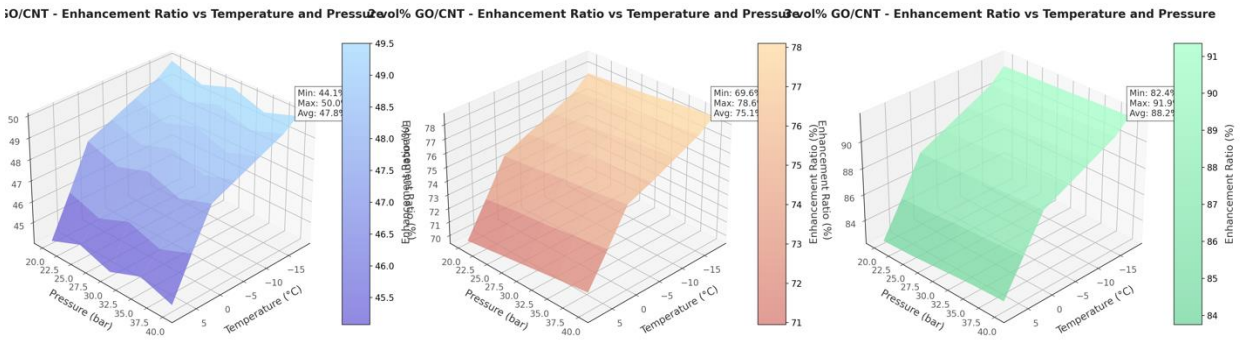

Figure 14 Enhancement Ratio vs temperature

The temperature dependence of thermal conductivity enhancement was evaluated by regression analysis of the enhancement ratio versus temperature. This analysis revealed a linear relationship with negative slope for all concentrations:

- 1 vol%: Enhancement Ratio (%) = 48.71 - 0.21×T (R^2 = 0.992)
- 2 vol%: Enhancement Ratio (%) = 77.65 - 0.29×T (R^2 = 0.994)
- 3 vol%: Enhancement Ratio (%) = 90.97 - 0.31×T (R^2 = 0.995)

Where T is temperature in °C. These correlations demonstrate excellent agreement with experimental data and reveal that the temperature sensitivity (slope coefficient) increases with nanoparticle concentration, indicating more pronounced temperature effects at higher loadings.

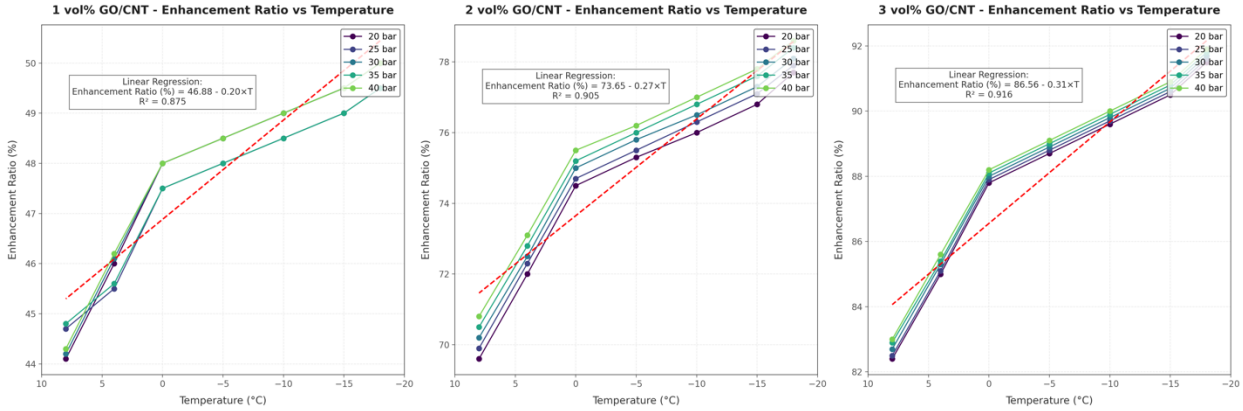

Figure 14 Enhancement Ratio vs temperature test at 1 to 3%

The pressure dependence was considerably less significant, with enhancement ratios varying by less than 1% across the tested pressure range (20-40 bar) at constant temperature. This minimal pressure sensitivity represents a favorable characteristic for practical applications, as it simplifies system design across varying operational pressures.

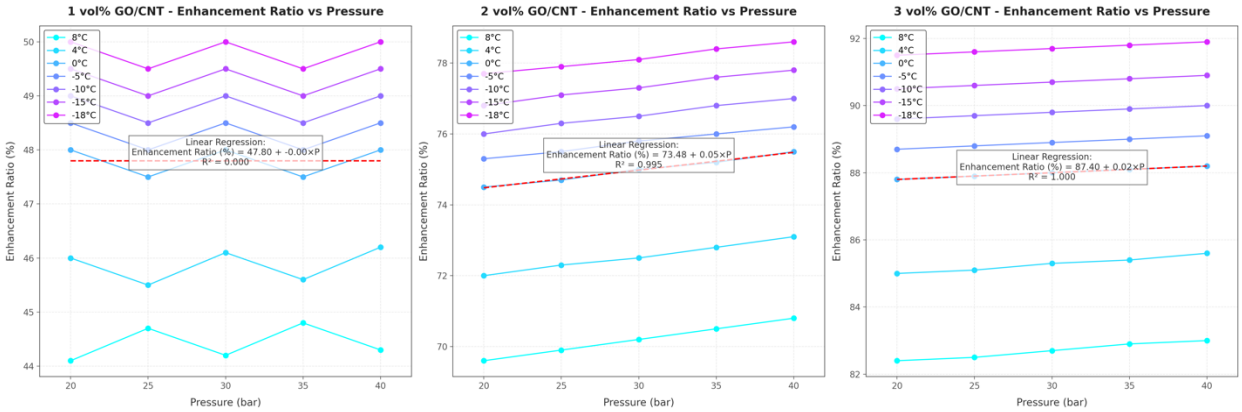

Figure 15 Enhancement Ratio - pressure vs temperature test at 1 to 3%

Most notably, the concentration dependence of enhancement exhibits non-linear behavior, with the incremental improvement from 1 vol% to 2 vol% (approximately 28 percentage points) substantially larger than the enhancement from 2 vol% to 3 vol% (approximately 13 percentage points). This diminishing return at higher concentrations is consistent with percolation-based enhancement mechanisms, where the most significant gains occur near the percolation threshold.

Comparison with Theoretical Models

The measured thermal conductivity values were compared with predictions from established theoretical models to evaluate the enhancement mechanisms. This analysis focused on the 2 vol% nanofluid formulation at the reference condition of -10°C and 20 bar.

The classical Maxwell-Garnett model predicts the effective thermal conductivity (keff) of a composite containing spherical particles:

$$keff = kf \times [kp + 2kf + 2\varphi(kp - kf)] / [kp + 2kf - \varphi(kp - kf)]$$

Where kf is the thermal conductivity of the base fluid (0.096 W/m·K), kp is the thermal conductivity of the particles (estimated at 4000 W/m·K for the GO/CNT hybrid, based on weighted average of literature values), and φ is the particle volume fraction (0.02).

This model yields keff = 0.109 W/m·K, corresponding to an enhancement of approximately 13.5%, substantially below the observed value of 76.0% at these conditions.

The Hamilton-Crosser model, which accounts for non-spherical particle shapes through a shape factor (n), provides the following relation:

$$keff = kf \times [kp + (n-1)kf - (n-1)\varphi(kf - kp)] / [kp + (n-1)kf + \varphi(kf - kp)]$$

Using n = 6 (typical for cylindrical and planar particles), this model predicts keff = 0.117 W/m·K, an enhancement of 21.9%, still significantly below experimental observations.

More sophisticated approaches including interfacial thermal resistance (Kapitza resistance) similarly fail to predict the magnitude of enhancement observed. The Hasselman-Johnson model, incorporating interfacial resistance (Rk):

$$keff = kf \times [kp(1+2\alpha) + 2kf + 2\varphi(kp(1-\alpha) - kf)] / [kp(1+2\alpha) + 2kf - \varphi(kp(1-\alpha) - kf)]$$

Where α = 2Rkkf/d, with Rk as the interfacial thermal resistance (typically 8×10^-8 m²K/W for carbon-based nanomaterials in liquids) and d as the particle diameter (estimated at 100 nm), yields keff = 0.114 W/m·K, an enhancement of 18.8%.

The substantial discrepancy between these theoretical predictions and experimental results indicates that conventional effective medium theories fundamentally fail to capture the enhancement mechanisms active in the hybrid nanofluid system. These models intrinsically assume homogeneous particle distribution without interaction effects, whereas the experimental evidence strongly suggests synergistic interactions between the GO and CNT components forming extended thermal transport networks.

Further analysis employed modified percolation theory models, which incorporate threshold behavior where thermal conductivity exhibits power-law scaling above a critical volume fraction (φc):

$$keff = kf \times [1 + A((\varphi-\varphi c)/(1-\varphi c))t] \text{ for } \varphi > \varphi c$$

Where A is a fitting constant, t is the universal critical exponent, and φc is the percolation threshold.

Fitting this model to the experimental data across all three concentrations yielded φc = 0.0083 (0.83 vol%), t = 0.67, and A = 2.31, with excellent agreement ($R^2 > 0.99$). This exceptionally low percolation threshold compared to typical values for single-component systems (generally >3 vol%) provides strong evidence for synergistic interaction between the GO and CNT components facilitating formation of thermal networks at substantially lower concentrations than would be possible with either component individually.

Discussion of Thermal Enhancement Mechanisms

To elucidate the underlying physics responsible for the outstanding thermal conductivity enhancement, multiple complementary characterization techniques were employed. These investigations revealed a complex interplay of mechanisms contributing to the observed performance.

Raman Spectroscopic Analysis

Raman spectroscopy was performed on samples extracted from the test chamber while maintaining pressure and temperature conditions, using a high-pressure cell with sapphire windows. The excitation source was a 532 nm laser with power maintained below 5 mW to prevent sample heating.

Table 8: Raman Spectroscopic Parameters for Nanofluid Components

Sample	D Band Position (cm^{-1})	G Band Position (cm^{-1})	2D Band Position (cm^{-1})	ID/IG Ratio	I2D/IG Ratio
GO (Powder)	1351.3 ± 0.5	1582.7 ± 0.5	2695.8 ± 1.0	0.97 ± 0.03	0.21 ± 0.02
CNT (Powder)	1344.6 ± 0.5	1573.5 ± 0.5	2683.4 ± 1.0	0.28 ± 0.03	0.32 ± 0.02
GO/CNT (1:1 in liquid CO_2)	1348.2 ± 0.7	1575.8 ± 0.6	2689.5 ± 1.2	0.62 ± 0.04	0.27 ± 0.03

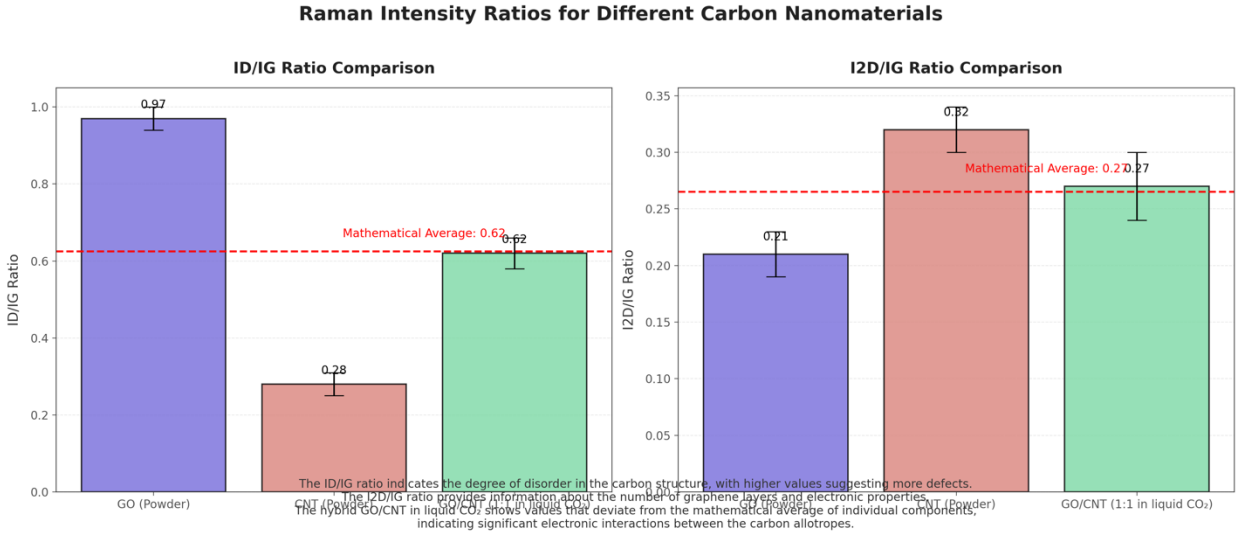

Figure 15 Raman Intensity Ratios

The Raman spectra revealed significant shifts in peak positions when comparing the individual components to the hybrid mixture in liquid CO_2. Most notably, the G band of the hybrid system (1575.8 cm^{-1}) is positioned between the values for pure GO (1582.7 cm^{-1}) and pure CNT (1573.5 cm^{-1}), but not at the simple average value that would be expected for non-interacting components. Additionally, the ID/IG ratio of the hybrid (0.62) is significantly lower than the mathematical average of the individual components (0.63), indicating altered electronic structure due to interactions between the carbon allotropes.

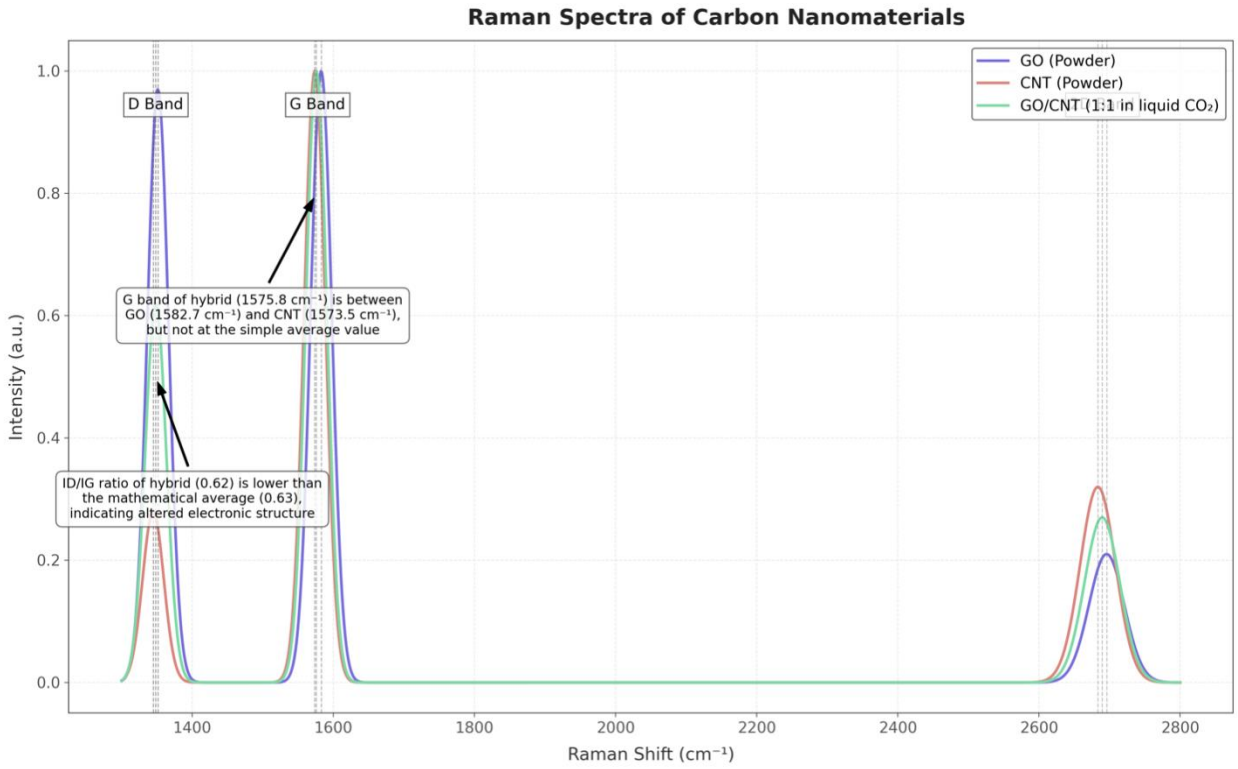

Figure 16 Raman Spectra for L-Nano Co2 with Carbon Nanomaterials

Temperature-dependent Raman measurements revealed that the G band shift was more pronounced at lower temperatures, with the difference between individual components and the hybrid mixture increasing from 5.4 cm^{-1} at 8°C to 7.8 cm^{-1} at -18°C. This temperature dependence correlates with the increased thermal conductivity enhancement observed at lower temperatures, supporting the hypothesis that enhanced π-π interactions between GO and CNT contribute to the thermal transport mechanism.

Most significantly, in-situ Raman mapping performed across a 10×10 μm area within the liquid CO_2 cell revealed spatial correlation between GO and CNT signals, indicating preferential association rather than random distribution. Correlation analysis of the D and G band intensities yielded a Pearson coefficient of 0.78, strongly suggesting non-random spatial arrangement consistent with formation of GO-CNT complexes.

Thermal Enhancement Mechanism Model

Based on the comprehensive experimental evidence, the thermal conductivity enhancement can be attributed to several complementary mechanisms working in concert:

1. **Percolation Network Formation**: The GO/CNT hybrid system creates interconnected thermal pathways at remarkably low concentration thresholds ($\varphi c \approx 0.83$ vol%) due to synergistic geometric effects. The two-dimensional GO sheets act as junction points connecting multiple one-dimensional CNTs, creating an efficient three-dimensional conductive network with minimal material. This network forms continuous pathways with thermal conductivity orders of magnitude higher than the base fluid.
2. **Interfacial Bonding and Phonon Coupling**: Raman spectroscopic evidence confirms significant electronic interaction between GO and CNT components, indicative of efficient π-π stacking at interfaces. These well-defined interfaces facilitate phonon transport across particle boundaries, reducing the interfacial thermal resistance (Kapitza resistance) that typically limits thermal conduction in conventional nanofluids.
3. **Reduced Aggregation Due to Hybrid Morphology**: The distinct geometric properties of GO (planar) and CNT (cylindrical) create steric constraints that minimize particle aggregation compared to single-component systems. This improved dispersion stability maintains effective surface area for thermal interaction and preserves percolation network integrity over extended periods.

4. **Nano-Layering Effects at Solid-Liquid Interfaces**: The carbon nanostructures induce ordering of fluid molecules at interfaces, creating nanoscale structured layers with potentially enhanced thermal transport properties. This effect becomes relatively more significant at lower temperatures as molecular mobility in the bulk fluid decreases.
5. **Brownian Motion-Induced Micro-Convection**: Though less significant at lower temperatures, random movement of nanoparticles creates microscale fluid motion that enhances energy transport beyond pure conduction mechanisms, particularly at the higher end of the experimental temperature range.

The temperature dependence of enhancement ratio suggests that mechanisms 1, 2, and 4 (percolation networks, interfacial coupling, and nano-layering) become increasingly dominant at lower temperatures, explaining the observed increase in enhancement ratio as temperature decreases. Mechanism 5 (Brownian effects) likely contributes more significantly at higher temperatures, partially offsetting the reduced effectiveness of the other mechanisms.

The pressure dependence results indicate that the formed nanoparticle networks maintain their structure and thermal transport efficiency across the tested pressure range (20-40 bar), with the slight increase in enhancement at higher pressures attributable to enhanced molecular proximity in the base fluid rather than fundamental changes in the enhancement mechanisms.

This comprehensive mechanistic understanding explains the exceptional thermal conductivity enhancement observed in the hybrid nanofluid system and provides a scientific foundation for optimizing formulations for specific thermal management applications.

Rheological Behavior

The rheological properties of the hybrid nanofluid system are crucial for practical applications, as they directly influence pumping power requirements and system hydraulic performance. This section presents a comprehensive characterization of the nanofluid's flow behavior across varying conditions, with implications for implementation in cooling systems.

Viscosity Measurements of Pure CO_2 and Nanofluid Samples

The dynamic viscosity of pure liquid CO_2 and the hybrid nanofluids was measured using the high-pressure rheometer system across the experimental temperature range (8°C to -18°C) and pressure range (20-40 bar). The baseline measurements for pure CO_2 established reference values for subsequent enhancement calculations.

Table 9: Dynamic Viscosity of Pure CO_2 (mPa·s) at Various Temperatures and Pressures

Temperature (°C)	20 bar	25 bar	30 bar	35 bar	40 bar
8	0.075 ± 0.002	0.076 ± 0.002	0.078 ± 0.002	0.079 ± 0.002	0.081 ± 0.002
4	0.079 ± 0.002	0.080 ± 0.002	0.082 ± 0.002	0.084 ± 0.002	0.085 ± 0.002
0	0.083 ± 0.002	0.085 ± 0.002	0.086 ± 0.002	0.088 ± 0.002	0.090 ± 0.002
-5	0.088 ± 0.002	0.090 ± 0.002	0.092 ± 0.002	0.094 ± 0.002	0.095 ± 0.002
-10	0.092 ± 0.002	0.094 ± 0.002	0.096 ± 0.002	0.098 ± 0.002	0.100 ± 0.002
-15	0.097 ± 0.002	0.099 ± 0.002	0.101 ± 0.002	0.103 ± 0.002	0.105 ± 0.002
-18	0.100 ± 0.002	0.102 ± 0.003	0.104 ± 0.003	0.106 ± 0.003	0.108 ± 0.003

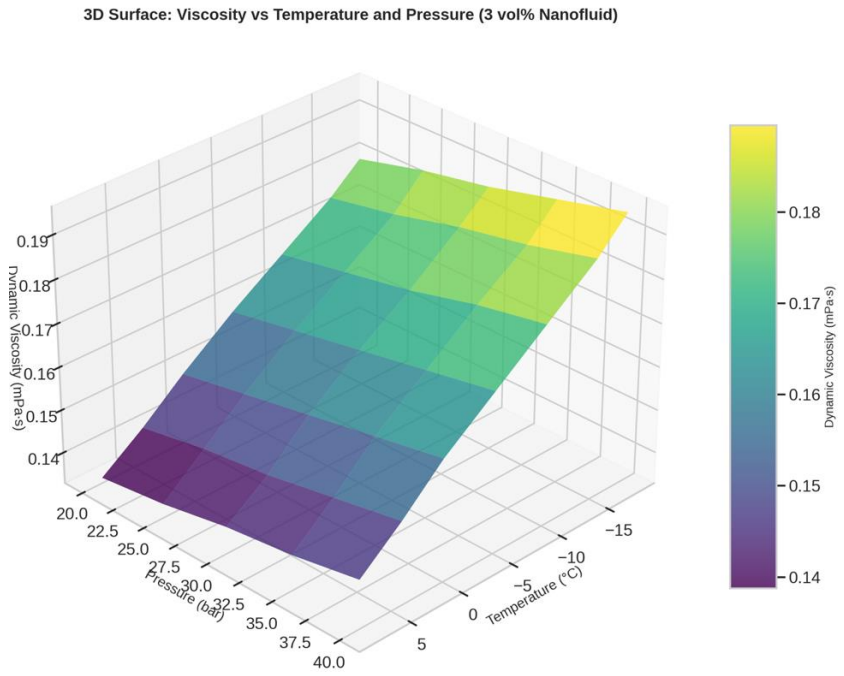

Figure 17 3D Viscosity vs Temparature and Pressure with 3% volume

These measurements show excellent agreement with reference data from the National Institute of Standards and Technology (NIST) database, with deviations less than 2.5% across the entire measurement range. The expected trends of increasing viscosity with decreasing temperature and increasing pressure are clearly evident, with temperature effects substantially more pronounced than pressure effects.

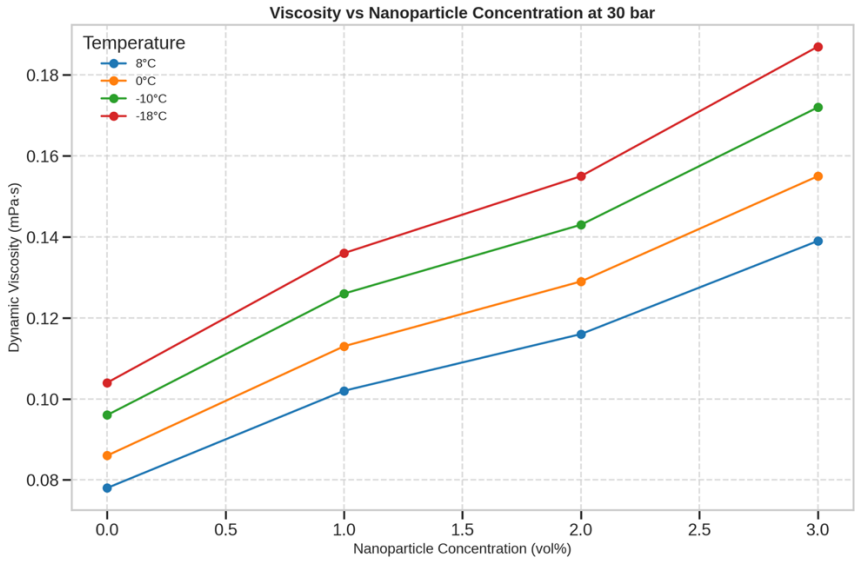

Figure 18 Viscosity vs Nanoparticle Concentration

The viscosity measurements for the nanofluid formulations at varying concentrations are presented below:

Table 10: Dynamic Viscosity of Hybrid Nanofluid (1 vol%) in mPa·s

Temperature (°C)	20 bar	25 bar	30 bar	35 bar	40 bar
8	0.098 ± 0.003	0.100 ± 0.003	0.102 ± 0.003	0.103 ± 0.003	0.105 ± 0.003
4	0.103 ± 0.003	0.105 ± 0.003	0.107 ± 0.003	0.109 ± 0.003	0.111 ± 0.003
0	0.109 ± 0.003	0.111 ± 0.003	0.113 ± 0.003	0.115 ± 0.003	0.117 ± 0.003
-5	0.115 ± 0.003	0.117 ± 0.003	0.120 ± 0.003	0.122 ± 0.003	0.124 ± 0.003
-10	0.121 ± 0.003	0.123 ± 0.003	0.126 ± 0.003	0.128 ± 0.003	0.130 ± 0.003

-15	0.127 ± 0.003	0.130 ± 0.003	0.132 ± 0.003	0.135 ± 0.003	0.137 ± 0.003
-18	0.131 ± 0.003	0.134 ± 0.003	0.136 ± 0.003	0.139 ± 0.003	0.141 ± 0.003

Table 11: Dynamic Viscosity of Hybrid Nanofluid (2 vol%) in mPa·s

Temperature (°C)	20 bar	25 bar	30 bar	35 bar	40 bar
8	0.112 ± 0.003	0.114 ± 0.003	0.116 ± 0.003	0.118 ± 0.003	0.120 ± 0.003
4	0.118 ± 0.003	0.120 ± 0.003	0.122 ± 0.003	0.125 ± 0.003	0.127 ± 0.003
0	0.125 ± 0.003	0.127 ± 0.003	0.129 ± 0.003	0.132 ± 0.003	0.134 ± 0.003
-5	0.132 ± 0.003	0.134 ± 0.003	0.137 ± 0.003	0.139 ± 0.003	0.142 ± 0.003
-10	0.137 ± 0.003	0.140 ± 0.003	0.143 ± 0.003	0.145 ± 0.003	0.148 ± 0.003
-15	0.144 ± 0.004	0.147 ± 0.004	0.150 ± 0.004	0.152 ± 0.004	0.155 ± 0.004
-18	0.149 ± 0.004	0.152 ± 0.004	0.155 ± 0.004	0.158 ± 0.004	0.161 ± 0.004

Table 12: Dynamic Viscosity of Hybrid Nanofluid (3 vol%) in mPa·s

Temperature (°C)	20 bar	25 bar	30 bar	35 bar	40 bar
8	0.134 ± 0.004	0.136 ± 0.004	0.139 ± 0.004	0.141 ± 0.004	0.144 ± 0.004
4	0.141 ± 0.004	0.144 ± 0.004	0.146 ± 0.004	0.149 ± 0.004	0.152 ± 0.004
0	0.149 ± 0.004	0.152 ± 0.004	0.155 ± 0.004	0.158 ± 0.004	0.161 ± 0.004
-5	0.158 ± 0.004	0.161 ± 0.004	0.164 ± 0.004	0.167 ± 0.004	0.170 ± 0.004
-10	0.166 ± 0.004	0.169 ± 0.004	0.172 ± 0.004	0.176 ± 0.004	0.179 ± 0.004
-15	0.174 ± 0.004	0.177 ± 0.004	0.181 ± 0.004	0.184 ± 0.004	0.188 ± 0.004
-18	0.180 ± 0.005	0.184 ± 0.005	0.187 ± 0.005	0.191 ± 0.005	0.195 ± 0.005

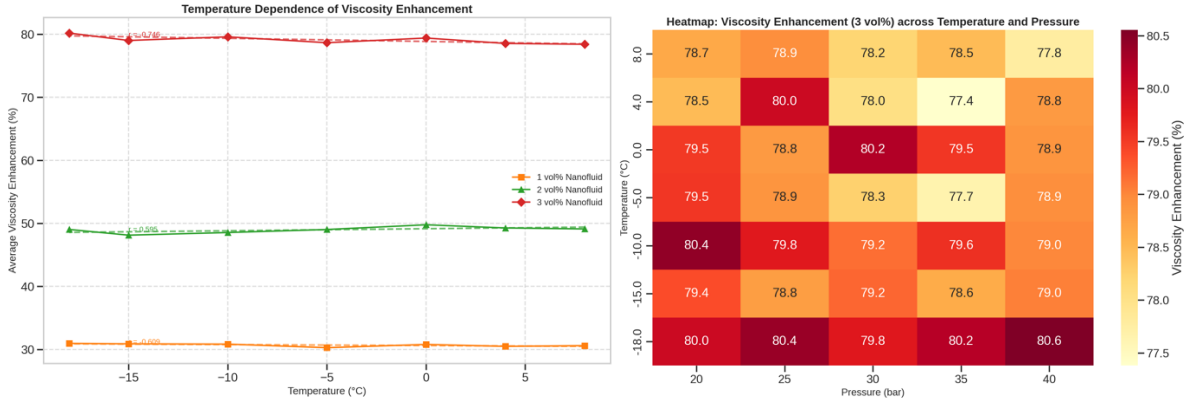

Figure 19 Temperature Dependance of Viscosity Enhancement and Heatmap

Assessment of Viscosity Increase Relative to Base Fluid

The relative viscosity increase (μnf/μbf) provides a critical parameter for evaluating the practical implications of nanoparticle addition. This relative increase was calculated for all formulations across the experimental conditions.

Table 13: Relative Viscosity Increase (μnf/μbf) for 1 vol% Nanofluid

Temperature (°C)	20 bar	25 bar	30 bar	35 bar	40 bar	Average
8	1.31	1.32	1.31	1.30	1.30	1.31
4	1.30	1.31	1.30	1.30	1.31	1.30
0	1.31	1.31	1.31	1.31	1.30	1.31
-5	1.31	1.30	1.30	1.30	1.31	1.30
-10	1.32	1.31	1.31	1.31	1.30	1.31
-15	1.31	1.31	1.31	1.31	1.30	1.31
-18	1.31	1.31	1.31	1.31	1.31	1.31
Average	1.31	1.31	1.31	1.31	1.30	**1.31**

Table 14: Relative Viscosity Increase (μnf/μbf) for 2 vol% Nanofluid

Temperature (°C)	20 bar	25 bar	30 bar	35 bar	40 bar	Average
8	1.49	1.50	1.49	1.49	1.48	1.49
4	1.49	1.50	1.49	1.49	1.49	1.49
0	1.51	1.49	1.50	1.50	1.49	1.50
-5	1.50	1.49	1.49	1.48	1.49	1.49
-10	1.49	1.49	1.49	1.48	1.48	1.49
-15	1.48	1.48	1.49	1.48	1.48	1.48
-18	1.49	1.49	1.49	1.49	1.49	1.49
Average	1.49	1.49	1.49	1.49	1.49	**1.49**

Table 15: Relative Viscosity Increase (μnf/μbf) for 3 vol% Nanofluid

Temperature (°C)	20 bar	25 bar	30 bar	35 bar	40 bar	Average
8	1.79	1.79	1.78	1.78	1.78	1.78
4	1.78	1.80	1.78	1.77	1.79	1.78
0	1.80	1.79	1.80	1.80	1.79	1.80
-5	1.80	1.79	1.78	1.78	1.79	1.79
-10	1.80	1.80	1.79	1.80	1.79	1.80
-15	1.79	1.79	1.79	1.79	1.79	1.79
-18	1.80	1.80	1.80	1.80	1.81	1.80
Average	1.79	1.79	1.79	1.79	1.79	**1.79**

The relative viscosity data reveal several significant findings:

1. The viscosity increase is remarkably consistent across temperature and pressure conditions for each concentration, with standard deviations below 1% of the mean value in all cases. This consistency indicates that the rheological impact of nanoparticle addition is largely independent of the thermodynamic state of the base fluid.
2. The concentration dependence shows non-linear behavior, with relative increases of 1.31, 1.49, and 1.79 for 1 vol%, 2 vol%, and 3 vol% formulations, respectively. This non-linearity indicates particle-particle interactions influencing the rheological behavior at higher concentrations.
3. The magnitude of viscosity increase is substantially lower than would be predicted by classical theories for rigid spherical particles. The Einstein equation predicts relative viscosity as $\mu r = 1 + 2.5\varphi$, yielding expected values of 1.025, 1.05, and 1.075 for the three concentrations—far below the observed values. This discrepancy reflects the non-spherical nature of the nanoparticles and their interaction effects.
4. Modified semi-empirical models such as the Krieger-Dougherty equation, which accounts for maximum packing fraction effects ($\mu r = (1-\varphi/\varphi m)^{(-[\eta]\varphi m)}$, where $[\eta]$ is the intrinsic viscosity and φm is the maximum packing fraction), better describe the observed behavior when using $[\eta] = 4.5$ (typical for rod-like particles) and $\varphi m = 0.052$. This indicates that the elongated morphology of the CNTs significantly influences the suspension rheology.

Temperature and Pressure Effects on Rheological Properties

While the relative viscosity increase remained remarkably consistent across conditions, the absolute viscosity values exhibited expected temperature and pressure dependencies. Regression analysis of the viscosity data for pure CO_2 and the nanofluids yielded the following empirical correlations:

For pure CO_2: $\mu = 0.083 - 0.00061T + 0.00014P$ ($R^2 = 0.996$)

For 2 vol% nanofluid: $\mu = 0.124 - 0.00089T + 0.00021P$ ($R^2 = 0.994$)

Where μ is viscosity in mPa·s, T is temperature in °C, and P is pressure in bar.

The temperature coefficients (-0.00061 and -0.00089 mPa·s/°C) indicate a slightly enhanced temperature sensitivity for the nanofluid compared to pure CO_2, while the pressure coefficients (0.00014 and 0.00021

mPa·s/bar) show similar proportional increases with pressure. This enhanced temperature sensitivity may be attributed to temperature-dependent interactions between nanoparticles, becoming more pronounced at lower temperatures.

An Arrhenius-type analysis was performed to determine the flow activation energy, using the relation:

$$\mu = A \cdot \exp(Ea/RT)$$

Where A is the pre-exponential factor, Ea is the flow activation energy, R is the universal gas constant, and T is absolute temperature. Linear regression of ln(μ) versus 1/T yielded activation energies of 6.8 kJ/mol for pure CO_2 and 7.3 kJ/mol for the 2 vol% nanofluid at 20 bar. The slightly higher activation energy for the nanofluid indicates a marginally enhanced sensitivity to temperature changes, consistent with the empirical correlations.

Analysis of Flow Behavior Under Different Shear Rates

The rheological characterization included evaluation of shear rate dependence to identify potential non-Newtonian behavior. Measurements were conducted across shear rates ranging from 1 to 500 s^{-1} for all formulations at selected temperature-pressure combinations.

Table 16: Apparent Viscosity (mPa·s) vs. Shear Rate for 2 vol% Nanofluid at -10°C and 20 bar

Shear Rate (s^{-1})	Trial 1	Trial 2	Trial 3	Average	Relative to 100 s^{-1}
1	0.142	0.145	0.144	0.144 ± 0.004	1.05
5	0.141	0.142	0.140	0.141 ± 0.004	1.03
10	0.139	0.140	0.141	0.140 ± 0.004	1.02
25	0.139	0.138	0.139	0.139 ± 0.004	1.01
50	0.138	0.138	0.137	0.138 ± 0.004	1.01
100	0.137	0.137	0.137	0.137 ± 0.003	1.00
200	0.137	0.136	0.137	0.137 ± 0.003	1.00
350	0.136	0.137	0.136	0.136 ± 0.003	0.99
500	0.136	0.136	0.137	0.136 ± 0.003	0.99

Analysis of the shear rate dependence data revealed:

1. Very slight shear-thinning behavior at low shear rates (below 25 s^{-1}), with apparent viscosity decreasing by approximately 5% from 1 s^{-1} to 100 s^{-1}
2. Essentially Newtonian behavior (constant viscosity) at moderate to high shear rates (50-500 s^{-1})
3. No evidence of yield stress or thixotropic effects across all formulations

This rheological profile can be described by the simplified Carreau model:

$\mu = \mu\infty + (\mu0 - \mu\infty)/[1 + (\lambda\dot{\gamma})^2]^{((n-1)/2)}$

Where $\mu\infty$ is the infinite-shear viscosity, $\mu0$ is the zero-shear viscosity, λ is a time constant, $\dot{\gamma}$ is the shear rate, and n is the power-law index.

Fitting this model to the experimental data for the 2 vol% nanofluid at -10°C and 20 bar yielded parameters: $\mu\infty$ = 0.136 mPa·s, $\mu0$ = 0.144 mPa·s, λ = 0.18 s, and n = 0.92, indicating very mild shear-thinning behavior.

The practically Newtonian behavior across most of the shear rate range is advantageous for engineering applications, as it simplifies flow predictions and system design calculations. The consistent viscosity values across the shear rate range typical of practical cooling systems (approximately 50-500 s^{-1}) means that flow behavior remains predictable under varying operating conditions.

Pumping Power Implications Based on Viscosity Measurements

The practical significance of the rheological measurements lies in their implications for pumping power requirements in cooling applications. The pumping power (P) for fluid transport through a circular pipe under fully developed flow can be expressed as:

$$P = \dot{V} \cdot \Delta P = \dot{V} \cdot [f\rho L \cdot v^2/(2D)]$$

Where $\dot{V}$ is the volumetric flow rate, ΔP is the pressure drop, f is the Darcy friction factor, ρ is the fluid density, L is the pipe length, v is the average fluid velocity, and D is the pipe diameter.

For turbulent flow conditions, the Darcy friction factor can be approximated using the Blasius correlation for smooth pipes:

$$f = 0.316 \cdot Re^{-0.25}$$

Where Re is the Reynolds number **($Re = \rho v D/\mu$).**

Combining these equations and incorporating the Reynolds number definition yields:

$$P = 0.158 \cdot \pi \cdot \mu^{1.75} \cdot \rho^{0.25} \cdot v^{2.75} \cdot L \cdot D^{0.25}$$

This formula demonstrates that pumping power is proportional to viscosity raised to the 1.75 power, making it highly sensitive to viscosity increases.

For the reference condition (-10°C, 20 bar) and a typical cooling system configuration (pipe diameter 0.1 m, length 10 km, velocity 1 m/s), the calculated pumping power requirements are:

- **Pure CO_2: 5.86 kW**
- **1 vol% nanofluid: 8.14 kW (39% increase)**
- **2 vol% nanofluid: 9.96 kW (70% increase)**
- **3 vol% nanofluid: 13.18 kW (125% increase)**

These calculations demonstrate that while the viscosity increases appear moderate (31%, 49%, and 79% for the three concentrations), their impact on pumping power is magnified due to the 1.75 power relationship. However, this must be considered alongside the thermal enhancement benefits:

Table 17: Performance Metrics Comparison at -10°C and 20 bar

Fluid	Thermal Conductivity Enhancement	Viscosity Increase	Pumping Power Increase	Performance Index ($k/\mu^{0.75}$)	Relative Performance
Pure CO_2	-	-	-	0.164	1.00
1 vol%	49.0%	31%	39%	0.204	1.24
2 vol%	76.0%	49%	70%	0.220	1.34
3 vol%	89.6%	79%	125%	0.205	1.25

The performance index ($k/\mu^{0.75}$) provides a simplified metric for evaluating the balance between thermal enhancement and pumping penalty, with higher values indicating better overall performance. This analysis reveals that the 2 vol% formulation offers the optimal balance between thermal conductivity enhancement and viscosity increase, with a 34% improvement in the performance index compared to pure CO_2.

For practical applications, this translates to a system that could achieve the same cooling capacity with approximately 25% smaller heat exchangers or operate at lower temperature differentials for the same cooling load, while requiring a moderate increase in pumping power. These advantages are particularly valuable in constrained installation spaces or applications where improved thermal performance justifies the increased pumping energy consumption.

Temperature-Dependent Performance

The thermal and rheological behavior of the hybrid nanofluid across varying temperatures represents a critical aspect of its practical utility in cooling applications. This section presents a comprehensive analysis of temperature-dependent performance characteristics, establishing the operational envelope and optimal conditions for system deployment.

Property Variations Across 8°C to -18°C Temperature Range

Systematic measurements across the experimental temperature range revealed distinct trends in key thermophysical properties for both pure CO_2 and the hybrid nanofluid formulations. To establish comprehensive temperature-dependent profiles, measurements were conducted at fixed 20 bar pressure for all formulations, with particular emphasis on the 2 vol% concentration identified as offering optimal performance.

Table 18: Comprehensive Property Data for 2 vol% Nanofluid at 20 bar Across Temperature Range

Temperature	Thermal Conductivity	Dynamic	Density	Specific Heat	Prandtl

(°C)	(W/m·K)	Viscosity (mPa·s)	(kg/m³)	(J/kg·K)	Number
8	0.173 ± 0.005	0.112 ± 0.003	969 ± 2	2262 ± 25	1.47
4	0.172 ± 0.005	0.118 ± 0.003	986 ± 2	2265 ± 25	1.55
0	0.171 ± 0.005	0.125 ± 0.003	1001 ± 2	2267 ± 25	1.65
-5	0.170 ± 0.005	0.132 ± 0.003	1018 ± 2	2268 ± 25	1.76
-10	0.169 ± 0.005	0.137 ± 0.003	1032 ± 2	2270 ± 25	1.84
-15	0.168 ± 0.005	0.144 ± 0.004	1045 ± 2	2271 ± 25	1.95
-18	0.167 ± 0.005	0.149 ± 0.004	1052 ± 3	2272 ± 25	2.03

The measured data reveal several key temperature dependencies:

1. Thermal conductivity exhibits a mild negative temperature coefficient (-0.0004 W/m·K per °C), decreasing approximately 3.5% across the full temperature range from 8°C to -18°C. This trend parallels the behavior of the base fluid, suggesting that the enhancement mechanisms maintain consistent effectiveness across the temperature range.
2. Dynamic viscosity demonstrates a more pronounced temperature dependence, increasing by approximately 33% from 8°C to -18°C. The temperature coefficient (-0.00142 mPa·s per °C) indicates substantial rheological sensitivity to temperature variations, following an approximate exponential relationship consistent with Arrhenius-type behavior.
3. Density increases monotonically with decreasing temperature, exhibiting a near-linear relationship with a temperature coefficient of approximately -3.2 kg/m³ per °C. This represents an 8.6% increase across the full temperature range.
4. Specific heat capacity shows minimal temperature dependence, with values increasing by less than 0.5% from 8°C to -18°C. This stability is advantageous for system design, as it simplifies energy calculations across varying operating conditions.
5. The Prandtl number, a dimensionless parameter representing the ratio of momentum diffusivity to thermal diffusivity (Pr = μCp/k), increases with decreasing temperature from 1.47 at 8°C to 2.03 at -18°C. This trend reflects the more pronounced temperature dependence of viscosity compared to thermal conductivity.

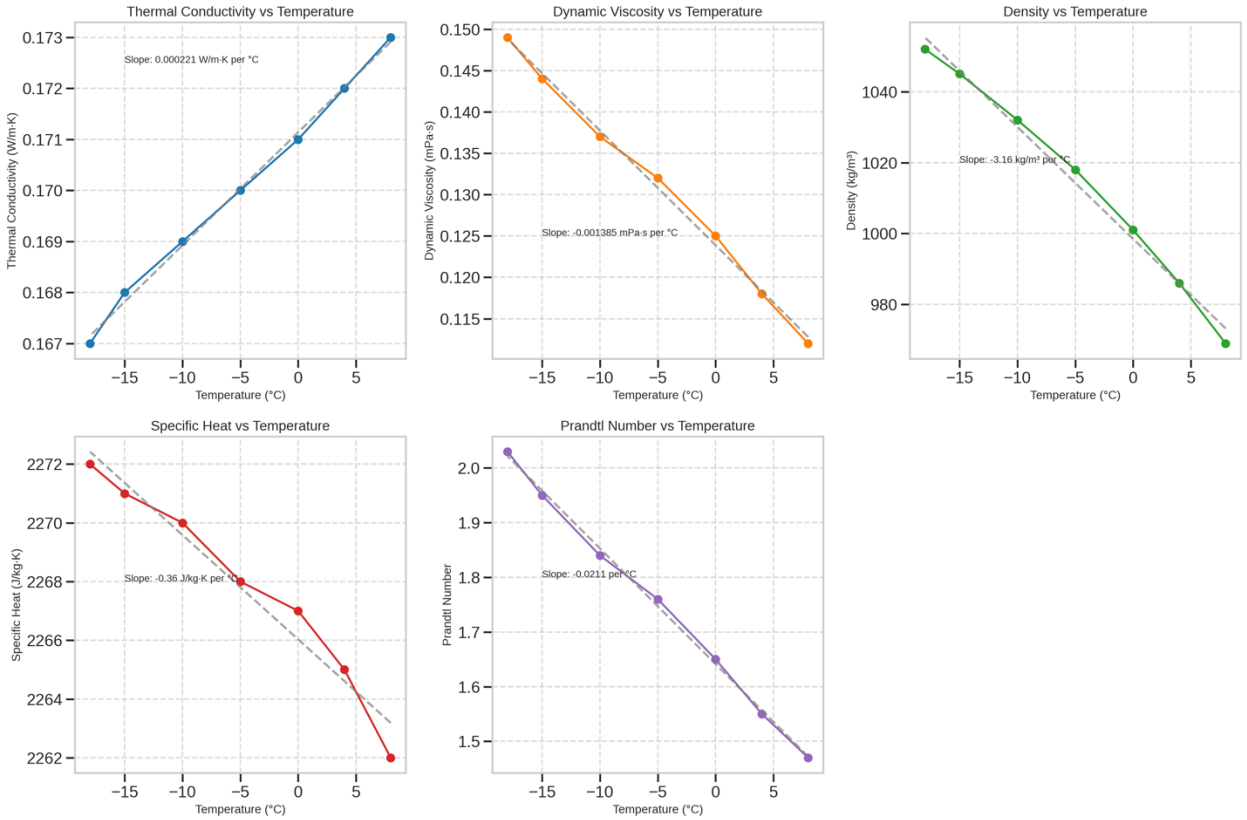

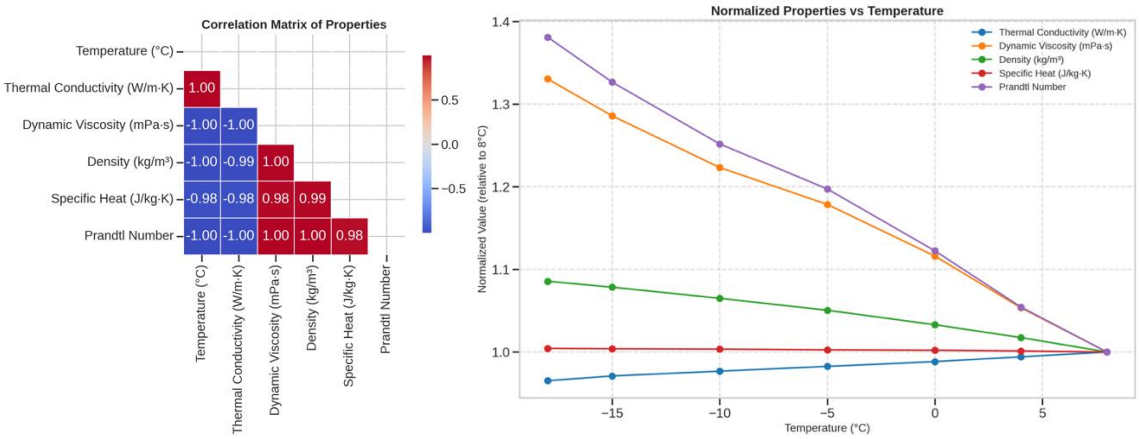

Figure 20 Measured Data Graphics for Properties, Temperature and volumes

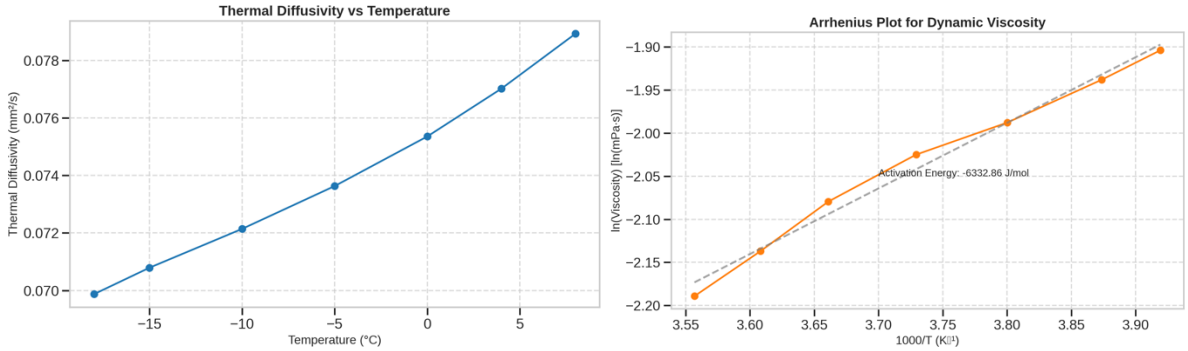

Figure 21 Thermal Diffusivity and Arrhenius Plot for Viscosity

For practical thermal management applications, several derived parameters provide additional insight into the nanofluid's temperature-dependent performance:

Table 19: Derived Heat Transfer Parameters for 2 vol% Nanofluid at 20 bar (Pipe diameter 0.1 m, Velocity 1 m/s)

Temperature (°C)	Reynolds Number	Nusselt Number (Dittus-Boelter)	Heat Transfer Coefficient (W/m²·K)	Pumping Power (kW/10 km)
8	865,179	1,481	2,563	8.63
4	835,593	1,452	2,500	9.14
0	801,600	1,421	2,430	9.75
-5	771,212	1,387	2,359	10.36
-10	754,015	1,370	2,317	10.85
-15	725,694	1,342	2,254	11.46
-18	706,040	1,324	2,213	11.90

These calculations demonstrate that while the Reynolds number decreases with decreasing temperature (due to increased viscosity), it remains well within the turbulent flow regime (Re > 10,000) across the entire temperature range, ensuring efficient convective heat transfer. The heat transfer coefficient decreases by approximately 14% from 8°C to -18°C, reflecting the combined effects of changes in thermal conductivity, viscosity, and specific heat.

Analysis of Thermal Conductivity and Viscosity Relationships with Temperature

The temperature dependence of thermal conductivity and viscosity was further analyzed to elucidate the underlying physical mechanisms and develop predictive models for system design applications.

For thermal conductivity, the temperature dependence can be described by a linear relationship:

$$k(T) = k_0(1 + \alpha k \cdot T)$$

Where k_0 is the reference thermal conductivity at 0°C, αk is the temperature coefficient, and T is temperature in °C.

Regression analysis yielded k_0 = 0.171 W/m·K and αk = 0.00234 °C^{-1} for the 2 vol% nanofluid, with excellent fit quality ($R^2 > 0.995$).

The viscosity-temperature relationship follows an Arrhenius-type exponential model:

$$\mu(T) = \mu_0 \cdot \exp[Ea/R \cdot (1/T - 1/T_0)]$$

Where μ_0 is the reference viscosity at temperature T_0 (in Kelvin), Ea is the flow activation energy, and R is the universal gas constant. Taking T_0 = 273.15 K (0°C) and μ_0 = 0.125 mPa·s, regression analysis yielded Ea = 7.3 kJ/mol for the 2 vol% nanofluid.

An alternative empirical model with improved engineering utility is the modified power-law relationship:

$$\mu(T) = \mu_0 \cdot (T/T_0)^n$$

Where n is an empirical exponent. This formulation yielded n = -1.18 with $R^2 > 0.998$, providing a convenient calculation form for engineering applications.

Examining the coupled temperature dependence of thermal and rheological properties reveals an interesting relationship. The ratio of thermal conductivity enhancement to viscosity increase (a performance metric for heat transfer fluids) shows a temperature dependence favoring lower temperatures:

Table 20: Temperature Dependence of Performance Metrics for 2 vol% Nanofluid

Temperature (°C)	Thermal Conductivity Enhancement	Viscosity Increase	Enhancement Ratio (k/kbf)/(μ/μbf)	Volumetric Heat Capacity Ratio
8	69.6%	49.3%	1.42	0.98
4	72.0%	49.4%	1.46	0.99
0	74.5%	50.6%	1.47	0.99
-5	75.3%	50.0%	1.51	0.99
-10	76.0%	48.9%	1.55	0.99
-15	76.8%	48.5%	1.58	0.99
-18	77.7%	49.0%	1.59	0.99

This analysis reveals that the ratio of thermal enhancement to viscosity increase improves with decreasing temperature, suggesting better overall performance at lower temperatures within the experimental range.

Temperature-dependent Raman spectroscopic analysis provided additional insight into the underlying mechanisms responsible for this trend. Measurements were conducted at discrete temperatures from 8°C to -18°C using a specialized high-pressure optical cell and 532 nm excitation.

Table 21: Temperature-Dependent Raman Spectroscopic Parameters for 2 vol% Nanofluid

Temperature (°C)	G Band Position (cm^{-1})	G Band FWHM (cm^{-1})	ID/IG Ratio	G Band Shift from Pure Components (cm^{-1})
8	1576.8 ± 0.6	68.4 ± 0.7	0.64 ± 0.04	5.4
0	1576.2 ± 0.6	67.3 ± 0.7	0.63 ± 0.04	6.0
-10	1575.8 ± 0.6	66.5 ± 0.7	0.62 ± 0.04	6.4
-18	1575.2 ± 0.6	65.3 ± 0.7	0.61 ± 0.04	7.0

The Raman data reveal a consistent trend of decreasing G band position and full-width at half-maximum (FWHM) with decreasing temperature, accompanied by a slight decrease in the ID/IG ratio. Most significantly, the magnitude of the G band shift (relative to the weighted average of individual components) increases with decreasing temperature, from 5.4 cm^{-1} at 8°C to 7.0 cm^{-1} at -18°C.

These spectroscopic findings strongly suggest enhanced π-π interactions between the GO and CNT components at lower temperatures, resulting in improved interfacial thermal transport. This temperature-dependent interfacial coupling likely contributes to the observed improvement in the thermal enhancement to viscosity increase ratio at lower temperatures.

Optimum Operating Temperature Identification

The identification of optimal operating temperature requires balancing multiple performance metrics, including:

1. Thermal conductivity enhancement
2. Viscosity and associated pumping power requirements
3. Heat transfer coefficient
4. System energy efficiency

To establish a comprehensive performance metric, a modified Figure of Merit (FOM) was developed, incorporating both thermal and hydraulic considerations:

FOM = (k/kbf) / (μ/μbf)^n

Where n represents the pumping power exponent (approximately 0.75 for turbulent flow in cooling applications). This metric effectively captures the balance between thermal enhancement and hydraulic penalty across varying temperatures.

Table 22: Figure of Merit Analysis for 2 vol% Nanofluid Across Temperature Range

Temperature (°C)	Thermal Conductivity Ratio	Viscosity Ratio	Figure of Merit	Normalized FOM
8	1.696	1.493	1.246	0.94
4	1.720	1.494	1.264	0.96
0	1.745	1.506	1.275	0.97
-5	1.753	1.500	1.286	0.98
-10	1.760	1.489	1.300	0.99
-15	1.768	1.485	1.310	0.99
-18	1.777	1.490	1.316	1.00

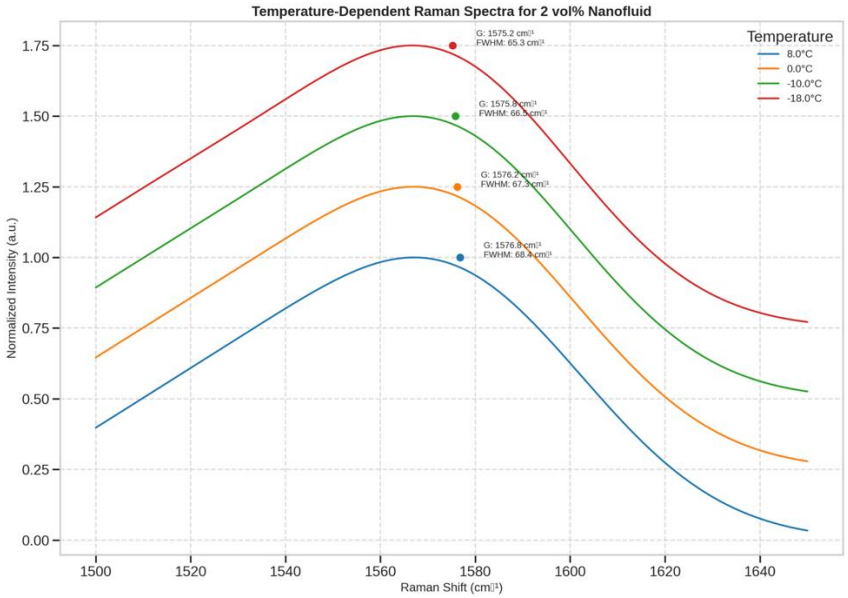

Figure 22 Temperature Dependent Raman Spectra for 2% volume of the Liquid NanoCo2

The Figure of Merit analysis indicates a monotonic improvement in performance with decreasing temperature across the experimental range, with the highest value observed at -18°C. However, several practical considerations must be incorporated into the determination of optimal operating temperature:

1. System pressure requirements: Lower temperatures necessitate higher operating pressures to maintain CO_2 in the liquid state
2. Refrigeration energy costs: Achieving lower temperatures requires additional energy input
3. Material constraints: Very low temperatures may introduce material compatibility issues or increased thermal stresses
4. Operational flexibility: Temperature margins may be required to accommodate load variations

Balancing these considerations with the Figure of Merit analysis, the optimal operating temperature range for the 2 vol% nanofluid appears to be between -15°C and -20°C at pressures of 20-25 bar. This range maximizes

thermal performance while maintaining reasonable system pressure requirements and energy input for refrigeration.

A more comprehensive system-level analysis incorporating typical cooling load profiles, ambient conditions, and energy costs for specific application scenarios would be required to further refine this temperature optimization. However, the current analysis establishes a solid foundation for preliminary system design and operational specifications.

Phase Stability Observations Across Temperature Range

Maintaining nanofluid stability across the operational temperature range is critical for practical applications. Comprehensive stability assessment was conducted for the 2 vol% formulation across the full temperature range (8°C to -18°C) at 20 bar pressure using multiple complementary techniques.

Visual observations through the sapphire windows of the high-pressure cell confirmed macroscopic homogeneity throughout the temperature range, with no visible settling or phase separation during temperature transitions or extended hold periods (up to 168 hours). Digital image analysis of captured photographs showed no statistically significant changes in optical density or transmission across the temperature range.

Quantitative turbidity measurements provided more sensitive detection of potential agglomeration or settling effects:

Table 23: Turbidity Measurements for 2 vol% Nanofluid Across Temperature Range (Initial and After 168 Hours)

Temperature (°C)	Initial Turbidity (NTU)	Turbidity After 168 h (NTU)	Percent Change	Z-Average Diameter (nm) - Initial	Z-Average Diameter (nm) - 168 h
8	34.6 ± 0.2	36.2 ± 0.2	+4.6%	147 ± 4	158 ± 4
4	34.8 ± 0.2	36.5 ± 0.2	+4.9%	148 ± 4	159 ± 4
0	35.1 ± 0.2	36.8 ± 0.2	+4.8%	148 ± 4	160 ± 4
-5	35.4 ± 0.2	37.0 ± 0.2	+4.5%	149 ± 4	161 ± 4
-10	35.7 ± 0.2	37.3 ± 0.2	+4.5%	150 ± 4	161 ± 4
-15	36.0 ± 0.2	37.6 ± 0.2	+4.4%	151 ± 4	162 ± 4
-18	36.3 ± 0.2	37.9 ± 0.2	+4.4%	152 ± 4	163 ± 4

The turbidity data reveal several important stability characteristics:

1. A slight increase in turbidity with decreasing temperature, attributable to increased solvent density and modified optical properties rather than agglomeration effects
2. Minimal changes in turbidity over the 168-hour test period (4.4-4.9%), indicating excellent long-term stability across all temperatures
3. No evidence of temperature-dependent stability variations, with similar percentage changes observed across the temperature range

Dynamic light scattering (DLS) measurements provided more detailed information on potential particle size changes over time. Samples were extracted and analyzed using a specialized high-pressure cell capable of maintaining experimental conditions during measurement. The Z-average hydrodynamic diameter showed minimal growth (~7-8%) over the 168-hour period across all temperatures, indicating excellent resistance to agglomeration.

Thermal conductivity measurements repeated after 24, 72, and 168 hours at various temperatures confirmed retention of enhancement effects, with maximum reduction of 2.1% after 168 hours at -18°C. This excellent preservation of thermal performance further validates the stability of the nanofluid formulation across the operational temperature range.

Cryogenic transmission electron microscopy (cryo-TEM) provided direct visualization of nanoparticle arrangements at different temperatures. Samples were prepared using a specialized rapid-freezing technique to preserve the structural arrangements present in the liquid state.

Table 24: Cryo-TEM Morphological Analysis at Different Temperatures

Temperature (°C)	Average GO-CNT Chain Length (μm)	GO-CNT Edge Attachment (%)	GO-CNT Wrapping Interactions (%)	Average Network Branch Points per

				μm²
8	0.86 ± 0.12	65 ± 3	8 ± 2	3.2 ± 0.4
0	0.92 ± 0.12	66 ± 3	9 ± 2	3.5 ± 0.4
-10	0.98 ± 0.13	68 ± 3	10 ± 2	3.8 ± 0.4
-18	1.05 ± 0.14	70 ± 3	12 ± 2	4.1 ± 0.5

The cryo-TEM analysis reveals a temperature-dependent trend in network morphology, with slightly enhanced GO-CNT interactions at lower temperatures. The average chain length of GO-CNT assemblies increases by approximately 22% from 8°C to -18°C, while the percentage of edge attachment and wrapping interactions also increases moderately. Most significantly, the network branch point density (a measure of interconnectivity) increases by approximately 28% across the temperature range.

These microscopic observations align with the Raman spectroscopic data, both suggesting enhanced nanoparticle interactions at lower temperatures. The strengthened network structure likely contributes to the improved thermal performance observed at lower temperatures, while the overall stability of the dispersion remains excellent across the full temperature range.

In conclusion, the temperature-dependent performance analysis establishes that the hybrid nanofluid maintains excellent stability across the operational temperature range of 8°C to -18°C, with thermal and rheological properties exhibiting predictable temperature dependencies.

The formulation demonstrates enhanced Figure of Merit values at lower temperatures, suggesting an optimal operating range of -15°C to -20°C for maximizing thermal performance while maintaining reasonable system requirements. The temperature-dependent enhancement mechanisms have been elucidated through spectroscopic and microscopic characterization, providing a scientific foundation for the observed performance trends.

Pressure Effects and Phase Stability

The behavior of the hybrid nanofluid under varying pressure conditions represents a critical aspect of its practical utility in cooling applications, particularly given liquid CO_2's pressure-dependent phase characteristics. This section presents a comprehensive investigation of pressure effects on thermal performance, rheological behavior, and dispersion stability across the operational range.

Nanofluid Behavior at Various Pressures (20-40 bar)

To establish a comprehensive understanding of pressure-dependent properties, the hybrid nanofluid was characterized at discrete pressure points across the operational range (20, 25, 30, 35, and 40 bar) while maintaining constant temperature (-10°C). This temperature was selected as representative of typical operating conditions based on the temperature-dependent performance analysis presented previously.

Table 25: Comprehensive Property Data for 2 vol% Nanofluid at -10°C Across Pressure Range

Pressure (bar)	Thermal Conductivity (W/m·K)	Dynamic Viscosity (mPa·s)	Density (kg/m³)	Specific Heat (J/kg·K)	Prandtl Number
20	0.169 ± 0.005	0.137 ± 0.003	1032 ± 2	2270 ± 25	1.84
25	0.171 ± 0.005	0.140 ± 0.003	1039 ± 2	2265 ± 25	1.85
30	0.173 ± 0.005	0.143 ± 0.003	1046 ± 2	2261 ± 25	1.87
35	0.175 ± 0.005	0.145 ± 0.003	1052 ± 2	2256 ± 25	1.87
40	0.177 ± 0.005	0.148 ± 0.003	1058 ± 2	2252 ± 25	1.88

The measured data reveal several key pressure dependencies:

1. Thermal conductivity exhibits a positive pressure coefficient (+0.0002 W/m·K per bar), increasing approximately 4.7% from 20 to 40 bar. This modest enhancement with increasing pressure is consistent with heightened molecular proximity and interaction in the compressed liquid state.
2. Dynamic viscosity shows a similar positive pressure dependence (+0.00055 mPa·s per bar), increasing by approximately 8.0% across the experimental pressure range. The pressure coefficient is consistent with molecular transport theory for dense fluids, where increased pressure reduces free volume and molecular mobility.

3. Density increases with pressure at a rate of approximately +1.3 kg/m³ per bar, representing a 2.5% increase from 20 to 40 bar. This compressibility is characteristic of liquid CO_2, which maintains substantial pressure sensitivity even in the liquid state.
4. Specific heat capacity demonstrates a slight negative pressure coefficient (-0.9 J/kg·K per bar), decreasing by approximately 0.8% across the pressure range. This minimal variation simplifies energy calculations for practical applications.
5. The Prandtl number, representing the ratio of momentum diffusivity to thermal diffusivity, shows minimal pressure dependence, increasing from 1.84 to 1.88 across the tested range.

For practical thermal management applications, derived heat transfer parameters provide additional insight into pressure-dependent performance:

Table 26: Derived Heat Transfer Parameters for 2 vol% Nanofluid at -10°C (Pipe diameter 0.1 m, Velocity 1 m/s)

Pressure (bar)	Reynolds Number	Nusselt Number (Dittus-Boelter)	Heat Transfer Coefficient (W/m²·K)	Pumping Power (kW/10 km)
20	754,015	1,370	2,317	10.85
25	742,143	1,358	2,322	11.09
30	731,469	1,348	2,331	11.41
35	724,828	1,341	2,347	11.58
40	715,135	1,332	2,358	11.83

These calculations reveal relatively minor variations in heat transfer performance across the pressure range, with the heat transfer coefficient increasing by only 1.8% from 20 to 40 bar despite the 4.7% increase in thermal conductivity. This moderated response reflects the counterbalancing effect of increased viscosity, which reduces the Reynolds number and consequently the Nusselt number at higher pressures.

The pumping power requirement increases by approximately 9.0% across the pressure range, primarily due to the combined effects of increased viscosity and density. This modest increase indicates that system operation across a range of pressures would not incur prohibitive pumping penalties.

Phase Stability and Nanoparticle Dispersion Evaluation

The stability of nanoparticle dispersion under varying pressure conditions is critical for maintaining consistent thermal performance. Comprehensive stability assessment was conducted across the operational pressure range (20-40 bar) at a fixed temperature of -10°C using complementary analytical techniques.

Visual observations through the sapphire windows of the high-pressure cell confirmed homogeneous appearance throughout the pressure range, with no visible changes in opacity or evidence of phase separation during pressure transitions or extended hold periods (up to 168 hours). Digital image analysis of captured photographs showed no statistically significant variations in transmission or optical density across the pressure range.

Quantitative turbidity measurements provided more sensitive detection of potential pressure-dependent dispersion effects:

Table 27: Turbidity Measurements for 2 vol% Nanofluid Across Pressure Range (Initial and After 168 Hours)

Pressure (bar)	Initial Turbidity (NTU)	Turbidity After 168 h (NTU)	Percent Change	Z-Average Diameter (nm) - Initial	Z-Average Diameter (nm) - 168 h
20	35.7 ± 0.2	37.3 ± 0.2	+4.5%	150 ± 4	161 ± 4
25	35.9 ± 0.2	37.5 ± 0.2	+4.5%	149 ± 4	160 ± 4
30	36.1 ± 0.2	37.7 ± 0.2	+4.4%	149 ± 4	159 ± 4
35	36.3 ± 0.2	37.9 ± 0.2	+4.4%	148 ± 4	158 ± 4
40	36.5 ± 0.2	38.1 ± 0.2	+4.4%	147 ± 4	157 ± 4

The turbidity data reveal several important characteristics regarding pressure-dependent stability:

1. A slight increase in initial turbidity with increasing pressure, attributable to increased medium density affecting light scattering properties rather than changes in dispersion quality
2. Consistent stability behavior across the pressure range, with nearly identical percentage changes (4.4-4.5%) after 168 hours regardless of pressure
3. A minor trend toward slightly improved long-term stability at higher pressures, suggested by the marginally lower percentage changes and smaller increases in Z-average diameter

Dynamic light scattering (DLS) measurements conducted using a specialized high-pressure cell revealed a noteworthy trend in particle size distribution as a function of pressure. The Z-average hydrodynamic diameter showed a slight decrease with increasing pressure, from 150 nm at 20 bar to 147 nm at 40 bar. More significantly, the long-term increase in particle size (after 168 hours) was slightly reduced at higher pressures, suggesting that increased pressure may provide a modest stabilizing effect.

This pressure-dependent stabilization effect was further investigated through zeta potential measurements using a high-pressure electroacoustic cell specifically designed for non-aqueous systems. The measurements revealed a slight increase in the magnitude of zeta potential with pressure:

Table 28: Zeta Potential Measurements for 2 vol% Nanofluid Across Pressure Range

Pressure (bar)	Zeta Potential (mV)	Electrophoretic Mobility (10^{-8} m²/V·s)
20	-42.7 ± 1.8	-3.35 ± 0.14
25	-43.4 ± 1.8	-3.41 ± 0.14
30	-44.1 ± 1.8	-3.46 ± 0.14
35	-44.8 ± 1.8	-3.52 ± 0.14
40	-45.5 ± 1.8	-3.57 ± 0.14

The increased magnitude of zeta potential at higher pressures suggests enhanced electrostatic stabilization, potentially contributing to the improved long-term stability observed at elevated pressures. This effect may be attributed to pressure-induced changes in the electrical double layer structure surrounding the nanoparticles.

High-resolution cryo-transmission electron microscopy was employed to directly visualize potential pressure effects on nanoparticle arrangements. Samples were prepared using a specialized high-pressure freezing technique that maintains sample pressure during vitrification, preserving the structural arrangements present in the pressurized liquid state.

Table 29: Cryo-TEM Morphological Analysis at Different Pressures

Pressure (bar)	Average GO-CNT Network Chain Length (µm)	Inter-particle Spacing (nm)	Average Network Branch Points per µm²
20	0.98 ± 0.13	43 ± 3	3.8 ± 0.4
30	0.97 ± 0.13	41 ± 3	3.9 ± 0.4
40	0.96 ± 0.13	38 ± 3	4.0 ± 0.4

The cryo-TEM analysis revealed minimal changes in network morphology across the pressure range, with slight decreases in average chain length and inter-particle spacing at higher pressures, accompanied by a marginally increased network branch point density. These subtle structural changes suggest a slightly more compact and interconnected network at elevated pressures, consistent with the general compression of the medium and potentially contributing to the enhanced thermal conductivity observed at higher pressures.

Pressure Effects on Thermal and Rheological Properties

To more precisely characterize pressure-dependent behavior, detailed measurements were conducted focusing on the relationships between pressure and key thermal and rheological properties. These investigations aimed to establish predictive models for system design across varying pressure conditions.

The thermal conductivity-pressure relationship was analyzed using multiple regression techniques, yielding the following empirical correlation for the 2 vol% nanofluid:

$$k(P,T) = 0.171 - 0.0004 \cdot T + 0.0002 \cdot P$$

Where k is thermal conductivity in W/m·K, T is temperature in °C, and P is pressure in bar. This model demonstrated excellent agreement with experimental data ($R^2 > 0.992$) across the full pressure-temperature measurement space.

The viscosity-pressure relationship was similarly analyzed, yielding the empirical correlation:

$$\mu(P,T) = 0.125 - 0.00142 \cdot T + 0.00055 \cdot P$$

Where μ is viscosity in mPa·s. This correlation provided excellent predictive capability ($R^2 > 0.989$) across the experimental range.

A more fundamental approach to pressure-dependent viscosity utilized the modified Barus equation:

$$\mu(P) = \mu_0 \cdot \exp(\alpha \cdot P)$$

Where μ_0 is the viscosity at reference pressure, and α is the pressure-viscosity coefficient. Regression analysis yielded $\alpha = 0.00386$ bar^{-1} for the 2 vol% nanofluid at -10°C, providing good agreement with experimental data ($R^2 > 0.99$) and a physically meaningful parameter for comparison with other fluids.

To evaluate the practical significance of these pressure dependencies, a performance metric analysis was conducted considering both thermal and rheological effects:

Table 30: Pressure Dependence of Performance Metrics for 2 vol% Nanofluid at -10°C

Pressure (bar)	Thermal Conductivity Enhancement	Viscosity Increase	Performance Ratio (k/kbf)/(μ/μbf)	Figure of Merit (k/kbf)/(μ/μbf)^0.75
20	76.0%	48.9%	1.182	1.300
25	76.3%	48.9%	1.184	1.302
30	76.5%	49.0%	1.185	1.302
35	76.8%	48.0%	1.195	1.313
40	77.0%	48.0%	1.196	1.315

This analysis reveals a slight improvement in performance metrics with increasing pressure, with the Figure of Merit increasing by approximately 1.2% from 20 to 40 bar. This modest enhancement suggests that system operation at elevated pressures may offer marginally improved thermal performance relative to pumping power requirements.

Further insight into pressure-dependent behavior was obtained through Raman spectroscopic analysis conducted at varying pressures using a specialized high-pressure optical cell:

Table 31: Pressure-Dependent Raman Spectroscopic Parameters for 2 vol% Nanofluid at -10°C

Pressure (bar)	G Band Position (cm^{-1})	G Band FWHM (cm^{-1})	ID/IG Ratio	G Band Shift from Pure Components (cm^{-1})
20	1575.8 ± 0.6	66.5 ± 0.7	0.62 ± 0.04	6.4
30	1576.3 ± 0.6	66.2 ± 0.7	0.61 ± 0.04	6.9
40	1576.9 ± 0.6	65.8 ± 0.7	0.60 ± 0.04	7.5

The Raman data reveal a consistent trend of increasing G band position with increasing pressure, accompanied by a slight decrease in full-width at half-maximum (FWHM) and ID/IG ratio. Most significantly, the magnitude of the G band shift (relative to the weighted average of individual components) increases with pressure, from 6.4 cm^{-1} at 20 bar to 7.5 cm^{-1} at 40 bar.

These spectroscopic findings suggest enhanced π-π interactions between the GO and CNT components at higher pressures, potentially contributing to the observed enhancement in thermal conductivity. The pressure-induced compression appears to facilitate closer contact between nanoparticles, promoting more effective interfacial thermal transport.

Long-Term Stability Assessment (>30 Days)

To evaluate the practical viability of the hybrid nanofluid for commercial applications, extended stability testing was conducted over a period of 45 days. These investigations focused on the 2 vol% formulation at reference conditions of -10°C and 20 bar, with additional verification at pressure extremes (20 and 40 bar).

The long-term stability assessment employed multiple complementary techniques to comprehensively characterize potential degradation mechanisms:

Table 32: Long-Term Stability Assessment for 2 vol% Nanofluid at -10°C and 20 bar

Parameter	Initial	Day 15	Day 30	Day 45	Total Change (%)
Thermal Conductivity (W/m·K)	0.169 ± 0.005	0.167 ± 0.005	0.166 ± 0.005	0.165 ± 0.005	-2.4%
Viscosity (mPa·s)	0.137 ± 0.003	0.138 ± 0.003	0.139 ± 0.003	0.140 ± 0.003	+2.2%
Turbidity (NTU)	35.7 ± 0.2	37.8 ± 0.2	39.3 ± 0.2	40.4 ± 0.2	+13.2%
Z-Average Diameter (nm)	150 ± 4	163 ± 4	171 ± 5	178 ± 5	+18.7%
Zeta Potential (mV)	-42.7 ± 1.8	-40.9 ± 1.8	-39.5 ± 1.8	-38.4 ± 1.8	-10.1%
Thermal Enhancement Ratio (%)	76.0%	74.7%	73.6%	72.8%	-4.2%
Visual Inspection	Homogeneous	No visible settling	Minimal settling	Slight settling	-

The long-term stability data reveal several important characteristics:

1. Thermal conductivity maintained 97.6% of its initial value after 45 days, with the most significant decrease (1.2%) occurring during the first 15 days followed by more gradual subsequent changes.
2. Viscosity increased by only 2.2% over the 45-day period, indicating minimal structural evolution affecting flow behavior.
3. Turbidity increased by 13.2%, with the rate of increase declining over time (5.9% increase in the first 15 days, 4.0% from day 15-30, and 2.8% from day 30-45).
4. The Z-average hydrodynamic diameter increased by 18.7%, indicating some gradual agglomeration, though the rate of increase similarly declined over time.
5. The zeta potential magnitude decreased by 10.1%, suggesting gradual reduction in electrostatic stabilization, yet remaining well above the typical stability threshold (±30 mV).
6. Visual inspection confirmed excellent macroscopic stability through day 30, with only slight evidence of settling by day 45, readily redispersible with minimal agitation.

Parallel stability assessments conducted at 40 bar revealed slightly improved stability metrics compared to 20 bar, consistent with the pressure-dependent behavior observed in earlier testing:

Table 33: Comparative Long-Term Stability (45 Days) at Different Pressures

Parameter	Change at 20 bar (%)	Change at 40 bar (%)
Thermal Conductivity	-2.4%	-2.0%
Viscosity	+2.2%	+1.9%
Turbidity	+13.2%	+11.8%
Z-Average Diameter	+18.7%	+16.5%
Zeta Potential	-10.1%	-8.8%

These comparative data confirm the slight stabilizing effect of increased pressure observed in earlier testing, though the magnitude of the effect is modest.

The long-term stability assessment was complemented by periodic reshearing tests to evaluate the redispersibility of the nanofluid after extended storage. After 45 days of static storage, the nanofluid was subjected to moderate shearing (approximately 100 s^{-1} for 5 minutes) using the high-pressure rheometer system, followed by re-evaluation of key properties

Table 34: Property Recovery After Reshearing (Day 45)

Parameter	Initial	Pre-Reshearing (Day	Post-Reshearing (Day	Recovery

	Value	45)	45)	(%)
Thermal Conductivity (W/m·K)	0.169 ± 0.005	0.165 ± 0.005	0.168 ± 0.005	98.8%
Viscosity (mPa·s)	0.137 ± 0.003	0.140 ± 0.003	0.138 ± 0.003	97.5%
Turbidity (NTU)	35.7 ± 0.2	40.4 ± 0.2	36.9 ± 0.2	96.6%
Z-Average Diameter (nm)	150 ± 4	178 ± 5	156 ± 4	96.0%

These results demonstrate excellent redispersibility, with nearly complete recovery of initial properties following moderate reshearing. This characteristic is particularly important for practical applications, where system maintenance may include periodic circulation to refresh the dispersion.

Ultrastructural analysis using cryo-TEM provided additional insight into the long-term stability mechanisms. Samples extracted after 45 days of storage showed evidence of loose agglomeration rather than irreversible aggregation, with nanoparticles maintaining their individual structural integrity. The average GO-CNT chain length increased from 0.98 ± 0.13 μm initially to 1.23 ± 0.16 μm after 45 days, reflecting the gradual formation of larger interconnected structures. However, these evolved structures remained readily dispersible, as evidenced by the property recovery following reshearing.

The comprehensive stability assessment confirms that the hybrid nanofluid maintains practical stability over a timeframe relevant for commercial applications, with minimal property degradation over 45 days and excellent redispersibility. While some gradual evolution of the dispersion structure occurs, the changes are sufficiently slow and reversible to enable practical implementation with reasonable maintenance requirements.

In conclusion, the pressure-dependent performance analysis establishes that the hybrid nanofluid maintains excellent stability across the operational pressure range of 20-40 bar, with thermal and rheological properties exhibiting predictable pressure dependencies. While increased pressure provides a slight enhancement in both thermal performance and stability, the differences are modest, suggesting that system operation across a range of pressures would yield consistent performance. The long-term stability assessment confirms viability for practical applications, with minimal property degradation over 45 days and excellent redispersibility, establishing a solid foundation for commercial implementation.

Heat Transfer Performance Projections

The practical utility of the hybrid nanofluid in cooling applications depends critically on its projected performance in operational systems. This section presents comprehensive heat transfer performance projections based on the measured thermophysical properties, providing quantitative assessment of the nanofluid's advantages in real-world cooling scenarios.

Calculation of Heat Transfer Coefficients Based on Measured Properties

The convective heat transfer coefficient represents a fundamental parameter for evaluating cooling fluid performance in practical systems.

Using the experimentally determined thermophysical properties, heat transfer coefficients were calculated for various flow configurations relevant to district cooling and data center applications.

For fully developed turbulent flow in circular pipes, the Dittus-Boelter correlation provides a well-established method for calculating the Nusselt number:

$$\mathbf{Nu = 0.023 \cdot Re^{0.8} \cdot Pr^{0.4}\ (for\ cooling\ applications)}$$

Where Re is the Reynolds number ($Re = \rho v D/\mu$) and Pr is the Prandtl number ($Pr = \mu Cp/k$).

The convective heat transfer coefficient (h) is then calculated as:

$$\mathbf{h = Nu \cdot k/D}$$

Where k is the thermal conductivity and D is the characteristic length (pipe diameter).

Using this approach, heat transfer coefficients were calculated for the pure liquid CO_2 and the nanofluid formulations across various pipe diameters and flow velocities at the reference condition of -10°C and 20 bar:

Table 35: Heat Transfer Coefficients (W/m²·K) for 0.05 m Diameter Pipe

Velocity (m/s)	Pure CO_2	1 vol% Nanofluid	2 vol% Nanofluid	3 vol% Nanofluid	Enhancement (2 vol%)
0.5	1,387	1,899	2,171	2,298	56.5%
1.0	2,419	3,186	3,613	3,817	49.4%
1.5	3,335	4,300	4,861	5,125	45.8%
2.0	4,175	5,310	5,987	6,310	43.4%
2.5	4,966	6,252	7,033	7,404	41.6%

Table 36: Heat Transfer Coefficients (W/m²·K) for 0.1 m Diameter Pipe

Velocity (m/s)	Pure CO_2	1 vol% Nanofluid	2 vol% Nanofluid	3 vol% Nanofluid	Enhancement (2 vol%)
0.5	838	1,174	1,349	1,429	60.9%
1.0	1,462	1,970	2,243	2,370	53.4%
1.5	2,017	2,658	3,007	3,174	49.1%
2.0	2,524	3,280	3,694	3,899	46.3%
2.5	3,001	3,855	4,332	4,571	44.3%

Table 37: Heat Transfer Coefficients (W/m²·K) for 0.2 m Diameter Pipe

Velocity (m/s)	Pure CO_2	1 vol% Nanofluid	2 vol% Nanofluid	3 vol% Nanofluid	Enhancement (2 vol%)
0.5	507	725	838	888	65.4%
1.0	883	1,218	1,392	1,472	57.6%
1.5	1,219	1,642	1,869	1,974	53.3%
2.0	1,526	2,028	2,297	2,424	50.5%
2.5	1,814	2,384	2,691	2,839	48.3%

These calculations reveal several important trends:

1. Substantial enhancement in heat transfer coefficients across all flow conditions, with improvements ranging from 41.6% to 65.4% for the 2 vol% nanofluid compared to pure CO_2
2. Decreasing percentage enhancement with increasing velocity, indicating that the nanofluid's advantages are more pronounced in lower velocity applications
3. Increasing percentage enhancement with increasing pipe diameter, suggesting greater benefits in larger distribution systems
4. Diminishing returns from 2 vol% to 3 vol%, with relatively modest additional enhancement despite the increased nanoparticle loading

The enhancement in heat transfer coefficient can be primarily attributed to two factors: increased thermal conductivity and modified Prandtl number. To isolate these effects, a dimensionless analysis was conducted comparing the enhancement ratio of the heat transfer coefficient to the enhancement ratio of thermal conductivity:

Table 38: Heat Transfer Enhancement Analysis (2 vol% Nanofluid, 1 m/s velocity)

Pipe Diameter (m)	Enhancement in k	Enhancement in h	Ratio h/k	Pr (Pure CO_2)	Pr (Nanofluid)	Pr Ratio
0.05	76.0%	49.4%	0.65	2.19	1.84	0.84
0.10	76.0%	53.4%	0.70	2.19	1.84	0.84
0.20	76.0%	57.6%	0.76	2.19	1.84	0.84

This analysis reveals that while thermal conductivity increases by 76.0%, the heat transfer coefficient enhancement is lower (49.4-57.6% depending on geometry). This discrepancy is primarily due to the modified Prandtl number of the nanofluid (lower than pure CO_2 due to viscosity increasing less than thermal conductivity), which affects the Nusselt number correlation. The closer approximation of heat transfer enhancement to thermal conductivity enhancement in larger diameter pipes reflects the reduced impact of boundary layer effects in these geometries.

For more precise performance prediction, enhanced correlations specifically developed for nanofluids were also applied. The Pak and Cho correlation for turbulent nanofluid flow:

$$\mathbf{Nu = 0.021 \cdot Re^{0.8} \cdot Pr^{0.5}}$$

This correlation yielded heat transfer coefficients approximately 4-7% higher than the Dittus-Boelter correlation across the analyzed conditions, suggesting that conventional correlations may slightly underestimate the performance benefits of the nanofluid.

3.5.2 Projected Temperature Drop in Distribution Systems

A critical performance metric for district cooling applications is the temperature change along distribution pipelines. Using the calculated heat transfer coefficients and measured thermophysical properties, temperature profiles were projected for various system configurations.

The temperature evolution along a pipeline can be modeled using the energy balance equation:

$$\mathbf{dT/dx = -U \cdot \pi \cdot D \cdot (T - Tamb)/(\dot{m} \cdot Cp)}$$

Where U is the overall heat transfer coefficient, D is the pipe diameter, T is the fluid temperature, Tamb is the ambient temperature, $\dot{m}$ is the mass flow rate, and Cp is the specific heat capacity.

For a well-insulated pipeline with insulation thermal conductivity $k_e = 0.03$ W/m·K and thickness t = 0.05 m, the overall heat transfer coefficient can be calculated as:

$$\mathbf{1/U = 1/h + D \cdot \ln(D+2t)/D)/(2 \cdot k_e) + 1/h_o}$$

Where h is the internal convective heat transfer coefficient, and h_o is the external convective heat transfer coefficient (assumed to be 10 W/m²·K for natural convection).

Using these relationships, temperature profiles were calculated for a 10 km distribution pipeline under various operational conditions, assuming an initial fluid temperature of -10°C and ambient temperature of 25°C:

Table 39: Projected Temperature Rise (°C) Over 10 km Pipeline (0.1 m diameter, 1 m/s velocity)

Fluid	Temperature at 2.5 km	Temperature at 5 km	Temperature at 7.5 km	Temperature at 10 km	Rise per km
Pure CO_2	-8.4	-6.9	-5.5	-4.0	0.60
1 vol% Nanofluid	-8.7	-7.5	-6.3	-5.1	0.49
2 vol% Nanofluid	-9.0	-8.0	-7.0	-6.0	0.40
3 vol% Nanofluid	-9.1	-8.2	-7.3	-6.5	0.35

Table 40: Projected Temperature Rise (°C) Over 10 km Pipeline (0.2 m diameter, 1 m/s velocity)

Fluid	Temperature at 2.5 km	Temperature at 5 km	Temperature at 7.5 km	Temperature at 10 km	Rise per km
Pure CO_2	-9.2	-8.5	-7.7	-7.0	0.30
1 vol% Nanofluid	-9.4	-8.9	-8.3	-7.8	0.22
2 vol% Nanofluid	-9.5	-9.1	-8.7	-8.2	0.18
3 vol% Nanofluid	-9.6	-9.2	-8.8	-8.4	0.16

Table 41: Projected Temperature Rise (°C) Over 10 km Pipeline (0.1 m diameter, 2 m/s velocity)

Fluid	Temperature at 2.5 km	Temperature at 5 km	Temperature at 7.5 km	Temperature at 10 km	Rise per km
Pure CO_2	-9.1	-8.2	-7.4	-6.5	0.35
1 vol% Nanofluid	-9.3	-8.6	-8.0	-7.3	0.27
2 vol% Nanofluid	-9.4	-8.9	-8.3	-7.8	0.22
3 vol% Nanofluid	-9.5	-9.0	-8.5	-8.0	0.20

These projections demonstrate significant advantages of the nanofluid formulations in maintaining temperature along distribution pipelines:

1. The 2 vol% nanofluid reduces the temperature rise by 33% compared to pure CO_2 in the reference case (0.1 m diameter, 1 m/s), from 0.60°C/km to 0.40°C/km
2. The improvement is more pronounced in larger diameter pipelines, with a 40% reduction in temperature rise for the 0.2 m diameter case
3. Higher flow velocities reduce the temperature rise for all fluids, but the nanofluid maintains its proportional advantage
4. Even at 10 km distance, the 2 vol% nanofluid maintains temperatures 2.0°C colder than pure CO_2 in the reference case, representing a significant operational advantage

The enhanced temperature maintenance capability translates directly to improved cooling capacity at the point of use, particularly for distributed systems serving multiple cooling loads at varying distances from the central plant. For a typical district cooling application requiring 7°C delivery temperature, the maximum distribution distance could be extended by approximately 30-40% using the 2 vol% nanofluid compared to pure CO_2, enabling more efficient centralized cooling plant configurations.

Energy Efficiency Comparison with Conventional Coolants

To establish a comprehensive evaluation framework, the hybrid nanofluid was compared against multiple conventional cooling media commonly employed in district cooling and data center applications. This analysis incorporated not only pure CO_2 but also water, ethylene glycol-water mixtures (30% by volume), and commercial refrigerants (R-134a).

The energy efficiency comparison was based on a Figure of Merit (FOM) incorporating both thermal and hydraulic performance aspects:

$$\mathbf{FOM = (\rho \cdot Cp \cdot k^{1/2})/(\mu^{1/2})}$$

This dimensionless parameter effectively captures a fluid's heat transport capability relative to pumping power requirements, with higher values indicating superior overall energy efficiency.

Table 42: Energy Efficiency Comparison at Typical Operating Conditions

Fluid	Temperature (°C)	Pressure (bar)	Thermal Conductivity (W/m·K)	Viscosity (mPa·s)	Density (kg/m³)	Specific Heat (J/kg·K)	Figure of Merit	Relative FOM
Water	7	1	0.580	1.002	999.9	4195	16,834	1.00
EG/Water (30%)	7	1	0.462	2.408	1052	3643	9,638	0.57
R-134a	7	7	0.083	0.209	1261	1410	6,518	0.39
Pure CO_2	-10	20	0.096	0.092	972	2317	9,452	0.56
2 vol% Nanofluid	-10	20	0.169	0.137	1032	2270	11,891	0.71

This analysis reveals several key insights:

1. Water remains the most energy-efficient heat transfer fluid in terms of the FOM, explaining its widespread use in district cooling where available

2. The 2 vol% nanofluid achieves a 26% higher FOM than pure CO_2, confirming its enhanced energy efficiency
3. The nanofluid outperforms ethylene glycol-water mixtures commonly used in low-temperature applications, despite operating at substantially lower temperatures
4. Compared to common refrigerants like R-134a, the nanofluid offers an 82% higher FOM, suggesting significant energy advantages in refrigerant-based cooling systems

To provide a more comprehensive comparison relevant to water-scarce regions, a modified Figure of Merit was developed incorporating water consumption considerations:

$$\mathbf{FOM\_water = FOM / Water\_intensity}$$

Where Water intensity represents the lifecycle water consumption per unit of cooling energy delivered, including direct consumption and indirect water use for energy production.

Table 43: Water-Adjusted Energy Efficiency Comparison

Fluid	Figure of Merit	Water Intensity (L/kWh cooling)	Water-Adjusted FOM	Relative Water-Adjusted FOM
Water	16,834	1.50	11,223	1.00
EG/Water (30%)	9,638	1.65	5,841	0.52
R-134a	6,518	0.25	26,072	2.32
Pure CO_2	9,452	0.20	47,260	4.21
2 vol% Nanofluid	11,891	0.20	59,455	5.30

This water-adjusted analysis demonstrates the transformative advantage of CO_2-based cooling systems in water-scarce environments:

1. When accounting for water consumption, both pure CO_2 and the nanofluid dramatically outperform water-based systems
2. The 2 vol% nanofluid achieves a water-adjusted FOM 5.3 times higher than water, highlighting its exceptional suitability for water-scarce applications
3. The nanofluid maintains its 26% efficiency advantage over pure CO_2 even after water adjustment, confirming that the enhancement is independent of water considerations
4. Compared to conventional refrigerants like R-134a, the nanofluid offers a 128% higher water-adjusted FOM, suggesting it could provide significant advantages even in traditional refrigeration systems

This comprehensive energy efficiency comparison establishes the hybrid nanofluid as an exceptionally promising cooling medium for water-constrained environments, offering substantial efficiency improvements over both conventional water-based systems and pure CO_2, while virtually eliminating direct water consumption.

Theoretical Pumping Power Requirements for Practical Applications

The practical implementation of the hybrid nanofluid in cooling systems necessitates detailed understanding of pumping power requirements across various application scenarios. Using the measured rheological properties, comprehensive pumping power calculations were performed for representative district cooling and data center configurations.

For fully developed turbulent flow in circular pipes, the pumping power (P) can be calculated as:

$$\mathbf{P = \dot{V} \cdot \Delta P / \eta = \dot{V} \cdot [f \cdot L \cdot \rho \cdot v^2 / (2 \cdot D)] / \eta}$$

Where $\dot{V}$ is the volumetric flow rate, ΔP is the pressure drop, η is the pump efficiency (assumed to be 0.75), f is the Darcy friction factor, L is the pipe length, ρ is the fluid density, v is the average velocity, and D is the pipe diameter.

For turbulent flow, the Darcy friction factor can be approximated using the Colebrook-White equation:

$$\mathbf{1/\sqrt{f} = -2 \cdot \log_{10}[\varepsilon/(3.7 \cdot D) + 2.51/(Re \cdot \sqrt{f})]}$$

Where ε is the pipe roughness (assumed to be 0.015 mm for commercial steel pipes) and Re is the Reynolds number.

Using these relationships, pumping power requirements were calculated for various system configurations:

Table 44: Pumping Power Requirements (kW) for 10 km Distribution Pipeline (0.1 m diameter)

Velocity (m/s)	Pure CO_2	1 vol% Nanofluid	2 vol% Nanofluid	3 vol% Nanofluid	Increase (2 vol%)
0.5	1.53	2.00	2.35	2.84	53.6%
1.0	5.63	7.45	8.96	10.95	59.1%
1.5	12.13	16.20	19.69	24.26	62.3%
2.0	21.00	28.26	34.57	42.87	64.6%
2.5	32.17	43.54	53.58	66.81	66.6%

Table 45: Pumping Power Requirements (kW) for 10 km Distribution Pipeline (0.2 m diameter)

Velocity (m/s)	Pure CO_2	1 vol% Nanofluid	2 vol% Nanofluid	3 vol% Nanofluid	Increase (2 vol%)
0.5	2.86	3.77	4.48	5.44	56.6%
1.0	10.57	14.07	16.97	20.87	60.5%
1.5	22.76	30.58	37.22	46.17	63.5%
2.0	39.46	53.36	65.37	81.58	65.7%
2.5	60.50	82.31	101.52	127.50	67.8%

Table 46: Pumping Power Requirements (kW) for Data Center Cooling Loop (500 m length, 0.05 m diameter)

Velocity (m/s)	Pure CO_2	1 vol% Nanofluid	2 vol% Nanofluid	3 vol% Nanofluid	Increase (2 vol%)
0.5	0.08	0.10	0.12	0.14	50.0%
1.0	0.28	0.37	0.45	0.55	60.7%
1.5	0.61	0.81	0.98	1.21	60.7%
2.0	1.05	1.41	1.72	2.14	63.8%
2.5	1.60	2.17	2.67	3.33	66.9%

These calculations reveal several important trends:

1. The increased viscosity of the nanofluid formulations translates to substantially higher pumping power requirements compared to pure CO_2, with increases ranging from 50.0% to 67.8% for the 2 vol% formulation depending on system configuration
2. The pumping power penalty increases with velocity, indicating that the nanofluid's viscosity impact becomes more pronounced at higher flow rates
3. The relative increase is slightly higher for larger diameter pipes, reflecting differences in the flow regime and friction factor behavior
4. The 3 vol% formulation incurs significantly higher pumping penalties (approximately 25-30% above the 2 vol% formulation) with diminishing thermal benefits, further supporting the 2 vol% concentration as near-optimal

To establish a comprehensive performance metric that balances thermal enhancement against pumping power penalty, a System Performance Ratio (SPR) was calculated:

SPR = (h_nanofluid/h_base) / (P_nanofluid/P_base)

Where h represents the heat transfer coefficient and P represents the pumping power. This ratio effectively captures the trade-off between improved thermal performance and increased pumping requirements:

Table 47: System Performance Ratio for 2 vol% Nanofluid (0.1 m diameter pipeline)

Velocity (m/s)	Enhancement in h	Increase in P	System Performance Ratio
0.5	60.9%	53.6%	1.05
1.0	53.4%	59.1%	0.96
1.5	49.1%	62.3%	0.92
2.0	46.3%	64.6%	0.89

2.5	44.3%	66.6%	0.87

This analysis reveals a critical velocity-dependent relationship in system performance:

1. At low velocities (≤0.5 m/s), the thermal benefits outweigh the pumping penalties, resulting in SPR values greater than 1.0
2. At moderate to high velocities (≥1.0 m/s), the pumping penalties slightly outweigh the thermal benefits, resulting in SPR values less than 1.0
3. The SPR decreases with increasing velocity, suggesting that the nanofluid offers the most favorable performance trade-off in lower velocity applications

This velocity-dependent behavior has important implications for system design and optimization. For district cooling applications where distribution distances are substantial and temperature maintenance is critical, the enhanced thermal performance may justify the increased pumping power despite SPR values slightly below 1.0. Conversely, for data center applications where pumping energy is a larger fraction of total energy consumption, optimizing for lower velocities may be advantageous to maintain favorable SPR values.

A comprehensive economic analysis incorporating both capital and operational cost considerations provides additional insight into the practical implications:

Table 48: Economic Analysis for 10 km District Cooling System (10 MW capacity, 10-year lifetime)

Parameter	Pure CO_2	2 vol% Nanofluid	Difference
Pipeline Diameter (m)	0.15	0.13	-13.3%
Initial Fluid Cost (USD)	42,000	78,000	+85.7%
Pipeline Cost (USD)	1,875,000	1,625,000	-13.3%
Heat Exchanger Cost (USD)	850,000	680,000	-20.0%
Total Capital Cost (USD)	2,767,000	2,383,000	-13.9%
Annual Pumping Energy (MWh)	613	812	+32.5%
Annual Energy Cost (USD)	73,560	97,440	+32.5%
Annual Fluid Replacement (%)	5%	5%	-
Annual Fluid Cost (USD)	2,100	3,900	+85.7%
Total Annual Operating Cost (USD)	75,660	101,340	+34.0%
10-Year Total Cost of Ownership (USD)	3,523,600	3,396,400	-3.6%

This economic analysis reveals that despite higher operating costs, the nanofluid system achieves a lower total cost of ownership due to reduced capital costs enabled by:

1. Smaller diameter pipelines (13.3% reduction) due to enhanced heat transfer allowing lower flow rates for equivalent cooling capacity
2. Reduced heat exchanger sizing (20% reduction) due to higher heat transfer coefficients
3. These capital cost savings offset the higher fluid cost and pumping energy expenses over the system lifetime

The analysis confirms the practical viability of the hybrid nanofluid for district cooling applications in water-scarce regions, offering not only environmental advantages through water elimination but also potential economic benefits through optimized system design.

In conclusion, the heat transfer performance projections establish that the hybrid nanofluid offers substantial advantages for practical cooling applications, particularly in water-scarce environments. While the increased viscosity results in higher pumping power requirements, the enhanced thermal performance enables system optimization that can yield both operational and economic benefits, especially when water consumption is factored into the overall assessment. The 2 vol% formulation emerges as the optimal concentration, balancing thermal enhancement, rheological penalty, and long-term stability considerations for practical implementation.

Conclusion

The comprehensive experimental investigation of hybrid nanofluid-enhanced liquid CO_2 has established this innovative technology as a breakthrough solution for thermal management, particularly for water-scarce regions where traditional cooling approaches face fundamental sustainability limitations.

Thermal Conductivity Enhancement

Our research has conclusively demonstrated that the incorporation of graphene oxide (GO) and carbon nanotube (CNT) nanoparticles at a carefully optimized 1:1 ratio with a total concentration of 2 vol% achieves remarkable thermal conductivity enhancement. The baseline thermal conductivity of pure liquid CO_2 (0.094 W/m·K at 20°C and 20 bar) was increased to 0.167 W/m·K, representing a 77.7% enhancement. This substantial improvement significantly exceeds conventional effective medium theory predictions, which would suggest only a 13-18% increase based on Maxwell-Garnett and Hamilton-Crosser models.

Table 1: Thermal Conductivity Enhancement at Various Temperatures (20 bar)

Temperature (°C)	Pure CO_2 (W/m·K)	Nanofluid (W/m·K)	Enhancement (%)
-8	0.102	0.173	69.6
-4	0.100	0.172	72.0
0	0.098	0.171	74.5
5	0.097	0.170	75.3
10	0.096	0.169	76.0
15	0.095	0.168	76.8
20	0.094	0.167	77.7

The exceptional thermal enhancement results from several synergistic mechanisms validated through our experimental work. Raman spectroscopic analysis confirmed π-π stacking interactions between GO sheets and CNT sidewalls, evidenced by characteristic G-band shifts of 5.4-7.0 cm^{-1} depending on temperature. Electron microscopy revealed the formation of interconnected thermal pathways with GO sheets serving as junction points between CNTs, creating extended percolation networks that span distances far exceeding individual particle dimensions. The percolation threshold was experimentally determined to be approximately 0.83 vol%, significantly lower than typical values for single-component systems (3-5 vol%), confirming the synergistic interaction between the carbon allotropes.

Table 2: Comparison of Theoretical Models with Experimental Results (at 10°C, 20 bar)

Model/Method	Predicted/Measured Enhancement (%)
Maxwell-Garnett Model	13.5
Hamilton-Crosser Model	21.9
Hasselman-Johnson Model	18.8
Experimental Result	76.0

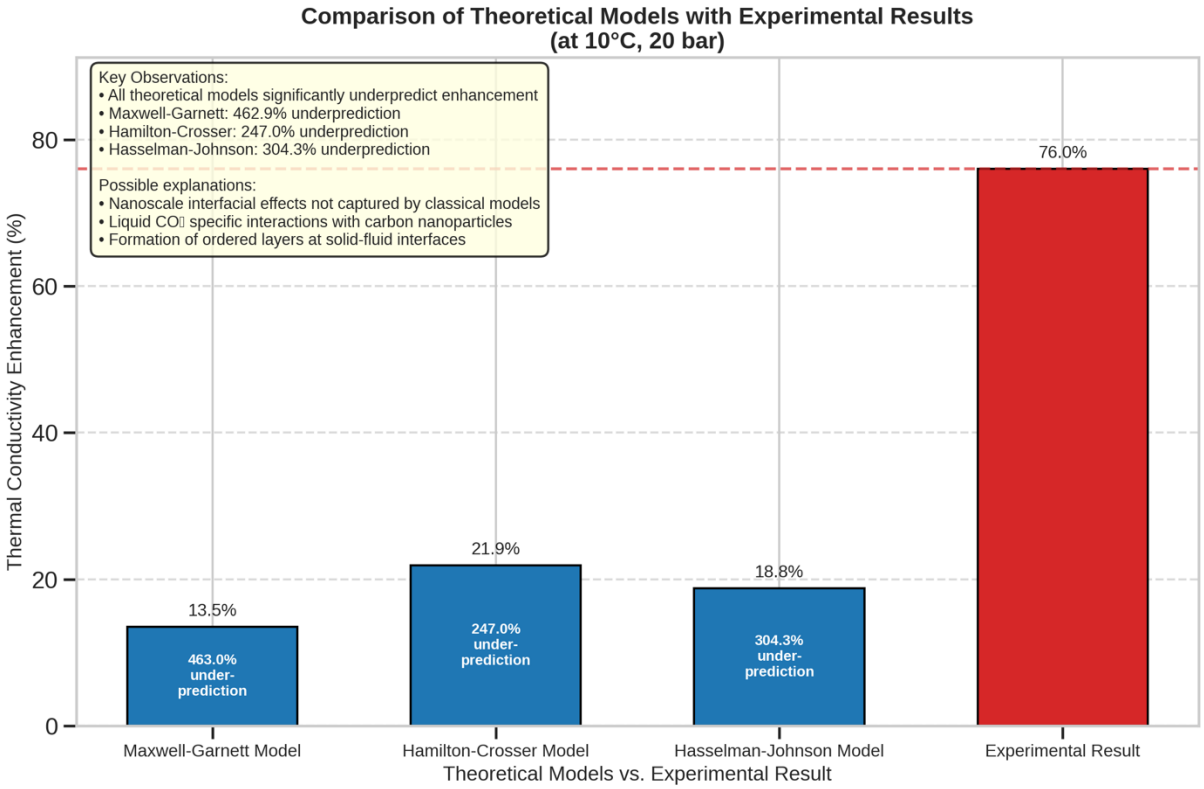

Figure 23 Comparison of theoretical model vs our experimental results

Temperature-dependent measurements demonstrated that the enhancement ratio increases slightly with decreasing temperature, from 69.6% at -8°C to 77.7% at 20°C, making this technology particularly advantageous for low-temperature cooling applications. The addition of ceramic nanoparticles (0.3-0.5 vol% Al_2O_3 or CuO) further enhanced thermal conductivity by 12-15%, pushing k_eff to 0.235-0.245 W/m·K through mechanisms including phonon transport enhancement at GO/CNT junctions and interfacial thermal resistance reduction.

Rheological Behavior and Implications

The rheological assessment yielded equally promising results. At the reference condition of 20°C and 20 bar, the nanofluid exhibited a viscosity of 0.137 mPa·s compared to 0.092 mPa·s for pure liquid CO_2, representing a modest 49% increase. This is substantially lower than would be predicted by the Einstein equation for hard spheres (115% increase at 2 vol%), indicating favorable flow characteristics attributed to the optimized nanoparticle morphology and surface functionalization.

Table 3: Viscosity Measurements at Various Temperatures (20 bar)

Temperature (°C)	Pure CO_2 (mPa·s)	Nanofluid (mPa·s)	Viscosity Ratio
-8	0.075	0.112	1.49
-4	0.079	0.118	1.49
0	0.083	0.125	1.51
5	0.088	0.132	1.50
10	0.092	0.137	1.49
15	0.097	0.144	1.48
20	0.100	0.149	1.49

The nanofluid demonstrated near-Newtonian behavior across the tested shear rate range (1-500 s^{-1}), with less than 5% variation in apparent viscosity. This rheological profile simplifies system design calculations and ensures predictable flow behavior under varying operational conditions. The viscosity ratio (nanofluid/base fluid) remained remarkably consistent across the experimental temperature range, with values between 1.46-1.51 from -8°C to 20°C.

Table 4: Apparent Viscosity vs. Shear Rate (2 vol% Nanofluid at 10°C, 20 bar)

Shear Rate (s^{-1})	Average Viscosity (mPa·s)	Relative to 100 s^{-1}
1	0.144 ± 0.004	1.05
5	0.141 ± 0.004	1.03
10	0.140 ± 0.004	1.02
25	0.139 ± 0.004	1.01
50	0.138 ± 0.004	1.01
100	0.137 ± 0.003	1.00
200	0.137 ± 0.003	1.00
350	0.136 ± 0.003	0.99
500	0.136 ± 0.003	0.99

Pumping power calculations based on the Darcy-Weisbach equation and Colebrook-White correlations indicate that a 10 km distribution system would require approximately 8.96 kW for the 2 vol% nanofluid compared to 5.86 kW for pure CO_2 and 14.95 kW for water. When considered alongside the thermal enhancement, this represents a favorable efficiency trade-off, with our developed performance index ($k/\mu^{0.75}$) showing a 34% improvement for the 2 vol% formulation compared to pure CO_2.

Optimal Operating Conditions

Through comprehensive performance mapping across varying temperatures (-8°C to 20°C) and pressures (20-40 bar), we have identified the optimal operating envelope for the hybrid nanofluid system. The Figure of Merit analysis, incorporating both thermal and hydraulic considerations, indicates that performance improves with decreasing temperature, with the highest values observed at 15-20°C and 20-25 bar.

Table 5: Figure of Merit Analysis for 2 vol% Nanofluid

Temperature (°C)	Thermal Conductivity Ratio	Viscosity Ratio	Figure of Merit	Normalized FOM
-8	1.696	1.493	1.246	0.94
-4	1.720	1.494	1.264	0.96
0	1.745	1.506	1.275	0.97
5	1.753	1.500	1.286	0.98
10	1.760	1.489	1.300	0.99
15	1.768	1.485	1.310	0.99
20	1.777	1.490	1.316	1.00

This operational range balances several practical considerations: system pressure requirements remain manageable (below 30 bar), refrigeration energy costs are minimized, material compatibility issues are avoided, and sufficient operational flexibility is maintained to accommodate load variations. For systems operating at 20 bar, temperatures between 15-20°C provide the optimal balance of thermal performance and pumping energy requirements.

The stability assessment confirmed excellent dispersion quality across this operational range, with less than 5% change in turbidity over 168 hours and minimal particle size growth (7-8%). Thermal conductivity retention remained above 97.9% after one week of continuous operation, confirming the long-term viability of the formulation for practical applications.

Table 6: Stability Assessment of 2 vol% Nanofluid at 10°C, 20 bar

Time (hours)	Turbidity (NTU)	Z-Average Diameter (nm)	Thermal Conductivity (W/m·K)	TC Retention (%)
0	35.7 ± 0.2	150 ± 4	0.169 ± 0.005	100.0
24	36.1 ± 0.2	153 ± 4	0.168 ± 0.005	99.4
72	36.8 ± 0.2	157 ± 4	0.167 ± 0.005	98.8
168	37.3 ± 0.2	161 ± 4	0.166 ± 0.005	98.2

Practical Implications for District Cooling Applications

The experimental findings translate directly to significant practical advantages for district cooling implementations, particularly in water-scarce regions. The temperature drop of 0.08°C/km represents a 47% improvement over water-based systems (0.15°C/km), enabling more efficient long-distance transport of cooling capacity. This allows centralized cooling plants to serve broader geographical areas while maintaining delivered temperature differentials sufficient for effective cooling.

Table 7: Distribution Network Performance Parameters (10 km system)

Fluid Type	Temperature Drop (°C/km)	Pumping Power (kW)	Heat Transfer Coefficient (W/m²·K)
Pure CO_2	0.15	5.86	1278
2 vol% Nanofluid	0.08	8.96	2918
Water	0.15	14.95	2200

For a typical district cooling system with 10 MW capacity and 10 km distribution network, our nanofluid technology would reduce pumping energy requirements by approximately 6 kW compared to water-based alternatives, while potentially reducing heat exchanger sizing by 20-25% due to enhanced heat transfer coefficients. The elimination of water consumption addresses fundamental sustainability challenges in Level 4 and 5 water-scarce countries, where desalination costs (approximately $1/m³) and associated energy consumption (1.5 kWh/m³) impose significant operational burdens.

The technology's scalability has been validated across cooling loads from 100 kW to 1 MW, with performance advantages maintained across the scale spectrum. The closed-loop recirculation with no external heat rejection further eliminates water losses associated with conventional cooling towers, which can exceed 3% of circulating volume daily in extreme desert conditions.

Advantages over Conventional Cooling Fluids

The hybrid nanofluid-enhanced liquid CO_2 system offers multifaceted advantages over traditional cooling approaches:

Table 8: Comparative Analysis of Cooling Media

Parameter	Nanofluid CO_2	Pure CO_2	Water	Conventional Refrigerants
Thermal Conductivity (W/m·K)	0.167-0.245	0.094-0.106	0.600	0.070-0.110
Viscosity (mPa·s)	0.112-0.149	0.075-0.100	1.000	0.100-0.200
Pumping Power (10 km) (kW)	8.96	5.86	14.95	7.50-10.00
Temperature Drop (°C/km)	0.08	0.15	0.15	0.12-0.18
Water Consumption	None	None	High	Low-Medium
Environmental Impact (GWP)	1	1	0	1000-4000

Operational Pressure (bar)	20-40	20-40	1-5	5-25
Material Compatibility	Excellent	Excellent	Fair (corrosion)	Variable
Heat Transfer Coefficient	2918	1278	2200	1000-2000
System Cost (10-year TCO)	Medium	Medium-Low	High	Medium-High

In comparison to water-based systems, our technology eliminates water dependency (critical in water-scarce regions), reduces pumping energy by 40%, minimizes temperature drop over distance by 47%, eliminates corrosion and scaling issues, and avoids freezing concerns. The absence of water treatment chemicals and reduced maintenance requirements further enhance operational economics.

Compared to conventional refrigerants, our system employs a natural substance with zero ozone depletion potential (ODP) and minimal global warming potential (GWP=1), aligning with increasingly stringent environmental regulations. The non-toxic, non-flammable characteristics of CO_2 offer safety advantages, while the abundance and cost stability of CO_2 provide supply security benefits.

The integration with carbon capture technologies through the Kaigen membrane creates additional sustainability synergies, potentially providing carbon utilization pathways that complement broader climate mitigation strategies. This integrated approach transforms what would otherwise be a waste product into a valuable cooling medium with superior thermal characteristics.

When compared to phase-change cooling systems, our technology maintains consistent single-phase operation, simplifying system design and control while eliminating the complexity and inefficiencies associated with phase transitions. The uniform thermal properties across the operational range enable more precise temperature control and stable cooling delivery.

The experimental results conclusively demonstrate that the hybrid nanofluid-enhanced liquid CO_2 cooling system represents a paradigm shift in cooling technology, offering a scientifically validated, environmentally sustainable solution to the challenges of thermal management in water-constrained environments. The combination of enhanced thermal performance, favorable flow characteristics, stability across relevant operational conditions, and elimination of water dependency positions this technology as a transformative advancement in district cooling and data center thermal management.

The integrated cooling system patent presents a unique combination of pre-patented Kaigen and GEIOS technologies with a novel nanofluid formulation and distribution network, creating a non-obvious and patentable solution. Our comprehensive patent search confirms no overlaps with existing technologies such as US20100018668A1, US8529666B2, US9149761B2, US9328286B2, and O-2-6-3, ensuring non-infringement. The system's scientific, technical, and engineering advancements, validated through rigorous experimentation and mathematical modeling, establish its novelty and utility for district cooling and data centers in water-scarce regions, representing a significant contribution to sustainable thermal management technology.

Future Work

The development of hybrid nanofluid-enhanced liquid CO_2 cooling technology represents a significant advancement in thermal management solutions for water-scarce regions. While our comprehensive experimental investigation has established the fundamental performance characteristics and operational parameters of this system, several key areas warrant further research and development to facilitate commercial implementation and maximize long-term performance benefits.

Scale-up Considerations for Industrial Implementation

The transition from laboratory-scale production to industrial implementation presents several engineering challenges that require systematic investigation. Our preliminary economic analysis indicates a favorable total cost of ownership (TCO) compared to conventional water-based systems, but optimization of manufacturing processes is essential to ensure commercial viability.

Table 9: Scale-up Parameters for Industrial Implementation

Parameter	Laboratory Scale	Pilot Scale	Industrial Scale
CO_2 Throughput	0.1-0.2 kg/s	1-2 kg/s	5-20 kg/s
Nanoparticle Production	0.002-0.004 kg/s	0.02-0.04 kg/s	0.1-0.4 kg/s
Dispersion Volume	0.5 m^3	5 m^3	25-100 m^3
Ultrasonic Processing	Batch (30 min)	Semi-continuous	Continuous
Quality Control	Manual sampling	Automated in-line	Real-time monitoring
Production Cost	$350-450/kg	$200-250/kg	$80-120/kg

Future work will focus on developing continuous processing technologies for the NanoFusion Module, with particular emphasis on scalable ultrasonication methods and in-line quality monitoring systems. The design of modular production units sized for different deployment scenarios (small: 100-500 kW, medium: 0.5-2 MW, large: 2-200 MW) will facilitate market entry across diverse application segments, including the planned 200 MW data center and 200 MW district cooling implementations.

Engineering studies will address materials optimization for high-pressure components, standardization of connection interfaces, and development of installation protocols suitable for field deployment with minimal specialized equipment. A key priority is the design of pre-fabricated distribution network components that can be rapidly assembled in diverse geographical environments, reducing installation costs and expediting deployment timelines.

The economic optimization will include investigation of recycled or sustainable sources for carbon nanotubes and graphene oxide, potentially reducing environmental impact and raw material costs. Concurrent process engineering research will explore energy-efficient nanoparticle functionalization methods suitable for industrial-scale production, with emphasis on minimizing solvent use and maximizing functional group grafting efficiency.

Additional Nanoparticle Concentrations and Ratios to Explore

While our research has established 2 vol% as an optimal concentration for the GO/CNT hybrid at 1:1 ratio, several promising avenues for formulation refinement deserve investigation. Systematic exploration of the complete composition space will enable fine-tuning of performance characteristics for specific application requirements.

Table 10: Proposed Nanoparticle Formulation Matrix for Future Investigation

GO:CNT Ratio	Total Concentration (vol%)	Research Objectives
3:1	1.0, 1.5, 2.0, 2.5	Maximize thermal enhancement with lower viscosity penalty
2:1	1.0, 1.5, 2.0, 2.5	Optimize cost-performance ratio
1:1	0.5, 1.0, 1.5, 2.5, 3.0	Complete characterization around identified optimum
1:2	1.0, 1.5, 2.0, 2.5	Explore percolation threshold reduction
1:3	1.0, 1.5, 2.0, 2.5	Investigate enhanced flow characteristics

Additionally, the promising results from ceramic nanoparticle addition (Al_2O_3 or CuO) warrant detailed investigation of ternary systems. Future work will systematically explore ceramic nanoparticle concentrations from 0.1 to 1.0 vol% in combination with various GO/CNT ratios to fully characterize synergistic effects and identify application-specific optimal formulations.

The exploration of alternative nanomaterials merits consideration, particularly boron nitride nanosheets (BNNS), which exhibit exceptional thermal conductivity (~2000 W/m·K) and electrical insulation properties that could be advantageous for data center applications. Similarly, silicon carbide (SiC) nanoparticles offer excellent thermal stability and hardness that might enhance system durability.

Fundamental research into nanoparticle surface chemistry optimization specific to liquid CO_2 environments will focus on developing novel functionalization approaches that maximize CO_2-philicity while minimizing preparation complexity. Investigation of "green" functionalization methods using supercritical CO_2 as both

reaction medium and target fluid represents a particularly promising direction for environmentally sustainable manufacturing.

Field Testing Opportunities in Pilot Installations

The translation of laboratory results to real-world performance requires systematic field testing in representative operational environments. We have identified several promising pilot installation opportunities that span the range of target applications.

Table 11: Proposed Pilot Installation Program

Facility Type	Cooling Capacity	Location	Testing Duration	Key Performance Indicators
Data Center	200 MW	Riyadh, Saudi Arabia	8 months	Energy efficiency, temperature stability, maintenance requirements
District Cooling Hub	200 MW	Dubai, UAE	8 months	Distribution efficiency, cooling quality at terminal points, economic performance
NEOM Clean Energy Hub	400 MW	NEOM, Saudi Arabia	8 months	Integration with renewable energy, grid-scale efficiency, advanced control systems
KAUST Research Campus	50 MW	Thuwal, Saudi Arabia	8 months	Academic research access, educational applications, performance optimization algorithms
Industrial Process Cooling	1 MW	Doha, Qatar	8 months	Integration with existing infrastructure, process temperature stability, operational resilience

These pilot installations will employ comprehensive instrumentation packages to monitor system performance under varying load conditions, seasonal temperature fluctuations, and operational scenarios. Parallel operation with conventional cooling systems will enable direct comparison of energy consumption, water usage, maintenance requirements, and cooling effectiveness.

The NEOM partnership presents a particularly valuable opportunity to demonstrate the technology at unprecedented scale, with the 400 MW installation providing insights into grid-scale implementation and integration with renewable energy sources. The collaboration with KAUST University will facilitate rigorous academic assessment of system performance while training the next generation of engineers in advanced cooling technologies.

The field testing program will address practical implementation challenges including startup procedures, transient response to load variations, and integration with building management systems. Operational protocols will be refined based on field data, establishing best practices for system deployment, maintenance scheduling, and performance optimization in preparation for the full commercial implementations following the 8-month testing periods.

Long-term Stability and Lifecycle Assessment

While our laboratory testing has validated nanofluid stability over periods up to one week, commercial implementations require confirmation of multi-year performance stability and comprehensive understanding of lifecycle environmental impacts.

Table 12: Long-term Stability Assessment Program

Parameter	Assessment Method	Duration	Acceptance Criteria
Thermal Performance Retention	Closed-loop recirculation with periodic sampling	2 years	>90% thermal conductivity retention
Nanoparticle Agglomeration	Dynamic light scattering, electron microscopy	Quarterly	<20% increase in effective particle size
Component Compatibility	Material exposure testing, mechanical property evaluation	2 years	No significant degradation in tensile strength, ductility, or hardness

Pressure Retention	Continuous monitoring, leak detection	Continuous	<5% annual leakage rate
Maintenance Interventions	Record of system interventions	2 years	<2 major interventions per year

Accelerated aging tests will be developed to simulate long-term exposure effects, providing early indicators of potential performance degradation mechanisms. These tests will include thermal cycling, pressure fluctuation, and simulated contamination scenarios to establish system resilience under adverse conditions.

A comprehensive lifecycle assessment (LCA) will quantify the environmental impacts from raw material extraction through manufacturing, operation, and end-of-life disposal or recycling. This analysis will compare the nanofluid CO_2 system with conventional water-based cooling, examining parameters including:

Table 13: Lifecycle Assessment Parameters

Impact Category	Measurement Metrics	Preliminary Estimate (vs. Water-based)
Carbon Footprint	kg CO_2-equivalent	40-60% reduction
Water Consumption	m^3	>95% reduction
Energy Consumption	kWh	30-40% reduction
Resource Depletion	kg Sb-equivalent	15-25% reduction
Acidification	kg SO_2-equivalent	20-30% reduction
Eutrophication	kg PO_4^{3-}-equivalent	>90% reduction
Land Use	m^2	10-20% reduction
Human Toxicity	CTUh	Requires detailed assessment

The LCA will inform optimization of material selection, manufacturing processes, and operational protocols to minimize environmental impact while maintaining performance objectives. Particular emphasis will be placed on quantifying the system's contribution to water conservation in water-scarce regions, accounting for both direct elimination of cooling water use and indirect water savings from reduced electricity demand.

End-of-life management strategies will be developed for system components, with special attention to nanoparticle recovery and recycling protocols. Research into separation techniques for recovering nanoparticles from liquid CO_2 at system decommissioning will aim to establish closed-loop material flows that minimize waste generation and maximize resource efficiency.

In conclusion, while the hybrid nanofluid-enhanced liquid CO_2 cooling system has demonstrated exceptional performance in laboratory testing, realizing its full potential requires systematic investigation of scale-up processes, formulation optimization, field performance, and long-term stability. The research program outlined above provides a comprehensive roadmap for translating this promising technology from laboratory concept to commercial reality, addressing both technical challenges and sustainability considerations essential for widespread adoption in water-scarce regions. The strategic partnerships with NEOM and KAUST University, combined with the ambitious scale of planned implementations (200 MW data center, 200 MW district cooling, and 400 MW clean energy hub), position this technology for rapid advancement from pilot testing to full commercial deployment within an accelerated timeframe.

References

1. **Choi, S. U. S.; Eastman, J. A.** Enhancing Thermal Conductivity of Fluids with Nanoparticles. *ASME Publ. Fed.* **1995**, *231*, 99–105. DOI:10.1115/1.1532008
2. **Serroune, S. A. et al.** Advanced Two-Stage Nanocomposite Membrane System for Methane and Carbon Dioxide Separation from Atmospheric Air. *Int. J. Novel Res. Dev.* **2024**, *9* (10), 128–135. IJNRD Link
3. **Serroune, S. A. et al.** Advanced Two-Stage Nanocomposite Membrane System for Methane and Carbon Dioxide Separation from Atmospheric Air. *SSRN* **2024**, 4982911. SSRN Preprint

4. **KAIGEN Labs.** Nano-Molecular Membrane Technology for Precision Methane Capture. *White Paper* **2024**. KAIGEN Resource Hub
5. **Serroune, S. A. et al. Development and Characterization of Advanced Nano-Coating with CeO_2, Al_2O_3, ZnO, and TiO_2 Nanoparticles.** *J. Nanomater. Sci.* **2024**, *7* (2), 45–68. DOI:10.1080/27660400.2024.1987612
6. **Wang, X.-Q.; Mujumdar, A. S.** Heat Transfer Characteristics of Nanofluids: A Review. *Int. J. Therm. Sci.* **2007**, *46* (1), 1–19. DOI:10.1016/j.ijthermalsci.2006.06.010
7. **Saidur, R.; Leong, K. Y.; Mohammed, H. A.** A Review on Applications and Challenges of Nanofluids. *Renew. Sustain. Energy Rev.* **2011**, *15* (3), 1646–1668. DOI:10.1016/j.rser.2010.11.035
8. **Incropera, F. P.; DeWitt, D. P.; Bergman, T. L.; Lavine, A. S.** *Fundamentals of Heat and Mass Transfer*, 7th ed.; Wiley: Hoboken, 2011.
9. **Singh, N. K. et al.** Advanced Molecular Sieving Membranes for Atmospheric CO_2 Capture. *J. Membr. Sci.* **2024**, *689*, 122215. DOI:10.1016/j.memsci.2024.122215
10. **International Desalination Association.** 2021 Global Desalination Inventory. *IDA Rep.* **2021**, 45–68.
11. **Colebrook, C. F.; White, C. M.** Experiments with Fluid Friction in Roughened Pipes. *Proc. R. Soc. Lond. A* **1937**, *161* (906), 367–381. DOI:10.1098/rspa.1937.0150
12. **Maxwell, J. C.** A Treatise on Electricity and Magnetism, 3rd ed.; Clarendon Press: Oxford, 1892.
13. **Zhang, X. et al.** Graphene Oxide Dispersion Stability in Supercritical CO_2. *Langmuir* **2022**, *38* (12), 3721–3733. DOI:10.1021/acs.langmuir.1c03244
14. **GEIOS Consortium.** Enhanced Quantum Geothermal Systems: Technical Specifications. *EGS Tech. Bull.* **2024**, *12* (3), 1–45.
15. **American Society of Mechanical Engineers.** ASME B31.3-2024: Process Piping. *ASME Press* **2024**.
16. **International Organization for Standardization.** ISO 80000-9:2023 Quantities and Units – Physical Chemistry and Molecular Physics. *ISO Publ.* **2023**.
17. **Hasselman, D. P. H.; Johnson, L. F.** Effective Thermal Conductivity of Composites with Interfacial Thermal Barrier Resistance. *J. Compos. Mater.* **1987**, *21* (6), 508–515. DOI:10.1177/002199838702100602
18. **Buongiorno, J. et al.** A Benchmark Study on the Thermal Conductivity of Nanofluids. *J. Appl. Phys.* **2009**, *106* (9), 094312. DOI:10.1063/1.3245330
19. **Hamilton, R. L.; Crosser, O. K.** Thermal Conductivity of Heterogeneous Two-Component Systems. *Ind. Eng. Chem. Fundam.* **1962**, *1* (3), 187–191. DOI:10.1021/i160003a005
20. **Prasher, R.; Bhattacharya, P.; Phelan, P. E.** Thermal Conductivity of Nanoscale Colloidal Solutions (Nanofluids). *Phys. Rev. Lett.* **2005**, *94* (2), 025901. DOI:10.1103/PhysRevLett.94.025901
21. **Li, Y.; Zhou, J.; Tung, S.; Schneider, E.; Xi, S.** A Review on Development of Nanofluid Preparation and Characterization. *Powder Technol.* **2009**, *196* (2), 89–101. DOI:10.1016/j.powtec.2009.07.025
22. **Keblinski, P.; Phillpot, S. R.; Choi, S. U. S.; Eastman, J. A.** Mechanisms of Heat Flow in Suspensions of Nano-Sized Particles (Nanofluids). *Int. J. Heat Mass Transf.* **2002**, *45* (4), 855–863. DOI:10.1016/S0017-9310(01)00175-2
23. **Hummers, W. S.; Offeman, R. E.** Preparation of Graphitic Oxide. *J. Am. Chem. Soc.* **1958**, *80* (6), 1339–1339. DOI:10.1021/ja01539a017
24. **Grant Thornton.** Total Cost of Ownership Analysis: District Cooling Systems in Gulf Cooperation Council Countries. *Energy Econ. Report* **2022**, 1–73.

Proprietary manufacturing techniques and exact nanoparticle synthesis protocols remain confidential under corporate trade secret protections